Experimental Investigation and Nonlocal Modeling of Compaction of Hot Asphalt Mixtures

A DISSERTATION
SUBMITTED TO THE FACULTY OF THE GRADUATE SCHOOL
OF THE UNIVERSITY OF MINNESOTA
BY

Tianhao Yan

IN PARTIAL FULFILLMENT OF THE REQUIREMENTS
FOR THE DEGREE OF
DOCTOR OF PHILOSOPHY

Advisors:
Mihai Marasteanu,
Jia-Liang Le

August, 2021

Acknowledgements

I would like to acknowledge all who provided me with academic or moral support over the years of my PhD study. First and foremost, I would like to extend my deepest gratitude to my advisors Prof. Mihai Marasteanu and Prof. Jia-Liang Le for their enormous contributions to this thesis. I am grateful to Prof. Marasteanu for enlightening me the essentials in pavement engineering, and involving me in his research projects on different topics of pavement engineering. I am indebted to Prof. Le for his guidance on the modeling part of this thesis. It is Prof. Le's courses on fracture mechanics, stability analysis, and reliability analysis that shaped my understanding on mechanical modeling. Beyond the wealth of knowledge of my advisors, I really appreciate their efforts in teaching me the philosophy of performing research, which I am sure would have a profound influence on my future career.

I want to express my gratitude to Prof. Henryk Stolarski, the chair of my committee. He is a remarkable teacher. His course, nonlinear finite element method, has deeply influenced the way how I think about material mechanics. His rigorous teaching style was extremely helpful to me for forming a deep and clear understanding of the subject. Moreover, He is always willing to help whenever his students have any questions. I really appreciate the time he spent meeting with me.

I am also grateful to my committee member Prof. Susan Mantell for her time and helpful feedback, which are extremely valuable for the completion of this thesis.

Special thanks go to Mugurel Turos, the manager of pavement research lab, for his substantial efforts in the experimental part of this thesis. In fact, many ideas of experiments belong to him, for example, the tribological test using rough surfaces. I really enjoyed the time I spent with him doing experiments and discussing research problems. Beyond that, Mugurel and his wife Mirela Miresan have also provided great help to my personal life, including served as the witnesses of my wedding during the pandemic period. I cannot

thank them enough for their support throughout these years.

Many other faculty have greatly impacted my PhD life. I want to thank Prof. Joe Labuz for hiring me as his TA for the civil engineering material course, which has been an invaluable experience for me. From him, I have learned a lot, especially his enthusiasm for teaching and his care for students. I want also to thank Prof. Colleen Meyers, the teacher of the TA training, for the help she provided to me on teaching. I must thank Prof. Richard James for allowing me to sit in his class of continuum mechanics. The understanding I achieved from this class has been extremely helpful for my PhD research. I must also thank Prof. Ellad Tadmor for allowing me to sit in his class on multiscale modeling, which strengthened a lot my understanding of material mechanics. Of course, I cannot forget those professors who have influenced me years ago in Southeast University during my undergraduate and master period. It is them who stimulated my interests in asphalt material and mechanics. They are Prof. Xiaoming Huang, Prof. Tao Ma, Prof. Li Guo, Prof. Lingyi Lv, and Prof. Shunzhi Qian.

I would like to acknowledge our collaborators at Minnesota Department of Transportation (MnDOT), especially Chelsea Bennett and John Garrity, for their help on collecting the data and materials that used in this research. Also, I would like to acknowledge Prof. Francesco Canestrari and Dr. Lorenzo Paolo Ingrassia of Università Politecnica delle Marche in Italy for their input in the tribological test part of this thesis.

I want to express my thanks to the other group members in Prof Marasteanu's and Prof. Le's group. Among them, Dr. Zhifeng Xu has helped me with the simulation of Gaussian random field. Dr. Teng Man has helped me with understanding some concepts in granular physics. Ravi Kumar has helped me with performing the tribological tests. I am also indebted to other group members: Dr. Meng Xu, Chen Hu, Jhenyffer Oliveira, Thomas Calhoon, Kristen Cash, and Anna Gorgogianni, for having helped me in all kinds of ways. To all of them, I am grateful for their support and friendship.

I gratefully acknowledge the sources that have funded me and my research during my PhD study, including the MnDOT research grant 1003325WO#106, and the Sommerfeld Fellowship of the Department of Civil, Environmental, and Geo- Engineering at UMN.

On the non-academic side, I am deeply grateful to my mother Hongyun Gao, my father Haifeng Yan for always being there supporting me and encouraging me. I am also deeply grateful to my wife Xiaoyi Fang for her love, support, and accompany throughout these years. Last but not least, I would also like to thank Yufeng Zhang, Yuesheng Gao, Jingkai

Jiang, Yilin Liu, Jing Gao, Qiming Zhu, Tao Tao, Lun Gao, Hanqing Zhao, Taihui Li, Rongsheng Chen, Shi'an Wang, Weijian Jiao, Thao Truong, Xiaoran Wang, Mohammad Ebrahim Shemshadian, Xiangfei Zhang, Chi Zhang, Bo Zhu, for their friendship. Thanks to them, my experience in UMN has been very colorful.

Abstract

Compaction is the most critical step in the construction process of asphalt pavements, which has a significant consequence on the durability of asphalt pavements. Although the importance of compaction has been well recognized, due to its complexity, the mechanisms of compaction have not been fully understood, and inadequate compaction is still a common problem in current practice. Therefore, the objective of this thesis is to explore physical mechanisms of compaction and to model the compaction process based on the mechanisms.

Before exploring mechanisms of compaction, we first analyze the field density data from recently constructed projects to achieve a thorough understanding of the current situation of field compaction. From it, probability distribution of field density and factors affecting field compaction are investigated. The results show that field density distribution is typically left-skewed and leptokurtic. The design parameter, N_{design}, and the material property, fine aggregate angularity, are identified to have significant effects on field density.

Then, the mechanism of how asphalt binder affects compaction of mixtures is investigated. A tribological test is developed to measure the lubricating effect (friction coefficient) of thin asphalt binder film (~ 10 μm) between rough solid surfaces, which simulates the interaction between binder and aggregates during compaction process. Tribological tests are conducted on graphite nanoplatelets (GNP) modified binders. The results show that GNP addition decreases the friction coefficient of binder between rough surfaces, which explains why GNP addition increases the compactability of mixtures. Compared to viscosity, the tribological property (friction coefficient) of asphalt binder is more related to compactability of mixtures, which implies that compared to viscosity the lubricating effect of asphalt binder may represents a more comprehensive mechanism which explains the effect of binder on compaction of asphalt mixtures mixtures.

Mechanisms of compaction in the length scale of asphalt mixture (~ 10 cm) are then studied to explain the macroscopic phenomena observed in gyratory compaction. Two mesoscopic mechanisms are proposed: jamming of aggregates and aggregate-binder interaction. By aggregates jamming, compaction process of asphalt mixture can be interpreted as the evolving jammed states of aggregates under the excitation of shear or vibration. This interpretation explains why shear and vibration enhance densification, and why shear resistance

increases with density, showing the coupling effects between shear and densification process of asphalt mixture. The mechanism of aggregate-binder interaction explains the decrease in shear resistance in the latter part of gyratory compaction.

Based on the mechanism of aggregate jamming (aggregate rearrangement), a one dimensional (1D) nonlocal model is developed for simulating the gyratory compaction process of asphalt mixtures. The model is formulated by combining the local mass balance law and a densification model of a cluster of aggregates. The nonlocal model involves a material characteristic length scale, which gives rise to strong effects of specimen height on the overall compaction curve as well as on the density profile. The proposed model is calibrated and validated by a set of gyratory compaction tests of different specimen heights. Through a set of parametric studies, it is shown that the nonlocal length scale plays a critical role in determining the spatial distribution of the local density and consequently the overall compaction curve. The model parameters can be related to the set up of the gyratory compaction and the material properties, such as the tribological property of binder, angularity of aggregates, and aggregate gradation, and therefore can provide guidance for the design of more compactable mixtures.

Lastly, effect of randomness on compaction process is studies based on the developed 1D nonlocal model for gyratory compaction. Two sources of randomness are investigated: the randomness in the initial density profile and the randomness in compaction effort. Monte Carlo simulations were performed to compute the probability distribution of average density of gyratory compacted specimens. The result explains the left-skewed and leptokurtic features of field density distribution.

Contents

List of Tables

List of Figures

Chapter 1

Introduction

1.1 Background

Compaction represents the most critical step in the construction process of asphalt pavements, by which asphalt mixture is turned from the initial loose state to a desired dense state in the field. The level of compaction is represented by the field density, which is typically expressed by the percent of theoretical maximum density (%G_{mm}) or the air-void ratio (100%−%G_{mm}). Numerous studies have emphasized the importance of compaction on the performance of asphalt pavements [4, 5, 6]. A direct consequence of insufficient compaction would be the low field density (or high air-void ratio) which will further cause many durability-related distresses, such as cracking, moisture damage and raveling [7, 8], and therefore will significantly reduce the service life of asphalt pavements.

Despite the importance of compaction, low compaction level (exemplified by low field density or high air-void ratio) is still a common problem in current practice, as reported in many previous studies [9, 10, 11]. The average field density reported in these studies is about 92∼93% G_{mm} (or 7∼8% air voids), which is much lower than the design density level, 96% G_{mm} (or 4% air voids), according to Superpave design method (AASHTO R35 [12]). It is believed that the current issue of low field density is closely related to the Superpave mixture design method, which mainly focused on designing rutting-resistant mixtures but did not give enough consideration to the compactability or workability of mixtures. Mixtures designed by Superpave are typically sufficiently resistant to rutting while are not compactable enough. As a result, after the implementation of Superpave design method in the late 1990s, rutting

occurrence is essentially reduced, while durability-related issues related to low field densities are becoming increasingly prevalent [13]. Therefore, there is a strong need to improve field density by designing more compactable mixtures.

As for the design of more compactable asphalt mixtures, the main obstacle is the lack of fundamental understanding of the compaction process of asphalt mixtures. In practice, the evaluation and design of compaction of asphalt mixtures rely heavily on empirical methods and trial-and-error. Examples are as follows. The most widely used index for characterizing the compactability of asphalt mixtures is the slope of the compaction curve in the semi-log scale (density vs. log(time)), which is proposed about half a century ago [14]. However, there is no theoretical explanation for the linear relationship between density and the logarithm of time; it is unclear to what extent this approximate is appropriate. There are other indices characterizing the compactability of asphalt mixtures based on the compaction curves, including locking point [15] and energy indices [16, 17, 18]. Similarly, these indices are essentially empirical which do not have clear physical meanings. In terms of mixture design, some empirical methods have been proposed to adjust the compactability of mixtures, for example, by means of the maximum density line [19] and Bailey method parameters [20, 21]. These methods aim to identify the aggregate gradation that produces the minimum air voids. However, the results are typically based on the experimental data of certain aggregate types, and it is unclear to what extent the results are applicable to other aggregate types.

More recently, with the advance in computational tools, major research efforts have been directed towards numerical modeling of the compaction process of asphalt mixtures. Material models under the framework of finite-strain elasto-viscoplasticity have been developed to capture the behavior of asphalt mixture during compaction and have been implemented by finite element method to simulate the compaction process of asphalt mixtures [22, 23, 24, 25]. However, these models are phenomenological in macroscopic level, which cannot capture the effect of mesoscale features on compaction, such as how the property of components (e.g., the angularity of aggregate and viscosity of asphalt binder) and their proportions affect the compaction. Because of that, these models are not that useful for mixture design which is basically a process of selecting and proportioning mesoscale components for achieving certain macroscopic properties.

Compaction of asphalt mixtures has also been studied by discrete element method [26, 27, 28, 29, 30]. The main advantage of the discrete approach is that it can capture some

mesoscale features explicitly, e.g., the shape and size distribution of aggregates. However, its main drawback is the excessive computational cost, which renders it prohibitive for being used for practice.

Despite these research efforts, due to the complexity of compaction of asphalt mixture, there are many macroscopic phenomena that we still do not understand, for example:

- Why adding graphite nanoplatelets (GNP) to asphalt mixtures increases its compactability, even though GNP addition increases the viscosity of asphalt binder? [31, 32]
- Why gyratory compaction is affected by height of the specimen? [33, 34]
- Why gyratory compacted specimen exhibits a nonuniform density profile, with higher density in the middle while lower density at the two ends of the specimen? [33, 34]
- Why in gyratory compaction shear resistance of the mixture first increases and then decreases? [35, 16, 17, 36]
- Why field density distribution is always left-skewed and leptokurtic? [37]

These macroscopic scale phenomena of compaction process must be a result of the behaviors of materials in the mesoscopic scale, i.e., the motion of aggregates and binder. However, the connections between the two scales are still obscure. In this thesis, we attempt to explain these macroscopic phenomena by physical mechanisms in the mesoscopic level.

1.2 Objectives and Organization

The goal of this thesis is to enhance the understanding of compaction process of asphalt mixtures through: (i) data analysis; (ii) experimental studies; and (iii) analytical modeling. Towards this, we have the following objectives:

- Perform data analysis to achieve a thorough understanding of the current situation of field compaction, including the statistical distribution of field density and the key factors affecting it.
- Perform an experimental study to investigate the effect of the tribological property of asphalt binder on compaction of asphalt mixtures.

- Perform an experimental study to explore the mesoscopic mechanisms that govern the compaction process of asphalt mixtures.

- Develop a material model for the densification process of asphalt mixtures based on the proposed mesoscopic mechanisms, and simulate the gyratory compaction process by using this model.

- Based on the developed model for gyratory compaction, investigate the effects of randomness (including the randomness of initial density and compaction effort) on the gyratory compaction process, with the aim of understanding the statistical distribution of field density data.

The thesis is organized as follows:

In Chapter 2, field density and material properties data obtained from recently constructed projects are analyzed and a thorough understanding of the current situation of field compaction is achieved. Material and design factors that affect field compaction are also identified.

In Chapter 3, the effect of tribological property of asphalt binder on compaction is investigated by performing tribology tests on graphite nanoplatelets (GNPs) modified asphalt binders. The results show that, compared to viscosity, tribological property of asphalt binder is more related to the compaction behavior of asphalt mixtures.

In Chapter 4, two mesoscopic physical mechanisms are proposed to explain the macroscopic behaviors of compaction of asphalt mixtures. One mechanism is related to the jamming of aggregates (aggregate rearrangement), which governs the densification process of the mixture. The other mechanism is related to the binder-aggregate interaction, which is responsible for the change of shear resistance of mixtures during compaction. Experimental studies are also performed to validate these mechanisms.

In Chapter 5, a one-dimensional (1D) nonlocal model for gyratory compaction is developed, based on the mesoscopic mechanism of aggregate rearrangement. The model is formulated by combining the local mass balance law and a densification model of a cluster of aggregates. The proposed model is able to simulate the compaction curve, density profile, and the size effect observed in the gyratory compaction process.

In Chapter 6, the 1D nonlocal model for gyratory compaction developed in Chapter 5 is employed to study the effect of randomness on compaction of asphalt mixtures. Two

sources of randomness are investigated: the randomness in the initial density profile and the randomness in compaction effort. Monte Carlo simulations were performed to compute the probability distribution of average density of gyratory compacted specimens. The results explain the features of field density distribution as observed in Chapter 2.

Chapter 7 summarizes the main conclusions of this study.

Chapter 2

Field Density Investigation of Asphalt Pavements in Minnesota[1]

In this Chapter, the current situation of field density in Minnesota is investigated, with the aim of identifying key factors affecting field density and possible measures to further improve field density. Data (including field densities and material properties) from 15 recent asphalt pavement projects were collected by Minnesota Department of Transportation (MnDOT) and are used in this investigation. First, we perform a statistical analysis to study the probability distribution of field densities. Then, we conduct a two-way analysis of variance (ANOVA) to check if the nominal maximum aggregate size (NMAS) and traffic levels have any significant effect on field densities. We follow with a correlation analysis to identify significant correlations between mixtures' compactability and material properties. The results show that the field density data approximately obey normal distribution, with an average field density of 93.4% of theoretical maximum specific gravity (G_{mm}). We observe significant differences between mixtures with different traffic levels, and find that mixture compactability is significantly correlated to fine aggregate angularity and fine aggregate gradation.

[1]This chapter is adopted from the following manuscript:
T. Yan, M. Marasteanu, C. Bennett, and J. Garrity. Field density investigation of asphalt mixtures in Minnesota. *Transp. Res. Rec.*, Advance online publication, 2021

2.1 Introduction

After the implementation of Superpave mix design in the late 1990s, durability related distresses, such as cracking, became the most prevalent distresses[13]. Durability issues, to a great extent, can be attributed to inadequate field density. The minimum requirement of as-constructed field density in most states is about 92∼93% of theoretical maximum specific gravity (G_{mm}), or 7∼8% of air voids[8]. Many previous studies have shown that as-constructed field densities are lower than desired[11, 38, 10], which causes premature durability related distresses, e.g. cracking, water damage, raveling, etc.[6, 7]. The importance of the as-constructed field density is emphasized by Linden et al.[6] who found that "a 1 percent increase in air voids (over the base air-void level of 7%) tends to produce about a 10 percent loss in pavement life." The relatively low as-constructed field density can be in part related to the implementation of Superpave mix design that emphasized preventing rutting, the most prevalent distress before Superpave, that resulted in designing harder to compact asphalt mixtures[13].

To improve durability and extend pavement life, many agencies have proposed modifications to the traditional Superpave mix design to improve compactability. Wisconsin Department of transportation (WisDOT) implemented a method called "regressing air voids", in which the mixture is designed at 3∼3.5% air voids by increasing the binder content by 0.3∼0.4%, compared to the traditional 4% air voids Superpave mixtures[39]. The additional binder increases the compactability of mixtures and allows achieving higher field densities.

Another method, developed as a result of joint research by Purdue University, Heritage Research Group, and Indiana Department of Transportation (INDOT), is the "Superpave 5", in which the asphalt mixtures are designed at 5% air voids and also compacted to 5% air voids in the field. This idea is achieved by significantly reducing N_{design} to 30 or 50, depending on traffic levels. In this method, N_{design} is related to compaction effort rather than traffic volume, which guarantees the consistency between laboratory and field compaction. Superpave 5 mixtures are designed by adjusting aggregate gradation while keeping the effective binder content unchanged, compared to traditional Superpave[40, 19].

Inspired by these research efforts, Minnesota Department of Transportation (MnDOT) and University of Minnesota have started working on developing a high-density mix design method, similar to Indiana Superpave 5 method, based on the use of locally available materials. Phase one of this study focused on understanding the compaction process of asphalt

mixture, and developing mechanical model and numerical tools to simulate the compaction process[41]. This paper presents research performed as part of phase two of this study, in which the current situation of field density in Minnesota is investigated, with the goal of answering the following questions:

- What is the current level of field density in Minnesota? How much improvement is needed to achieve the desired field density of 95% G_{mm} required by Superpave 5?
- Are field compaction values consistent with laboratory compaction values?
- What options are available in the current mix design, to increase compactability and field density?

In this research, the information obtained from 15 MnDOT projects, which includes field density data, mix design report, and material properties, are used. Statistical analyses are performed to investigate the probability distribution of field densities, and to determine the effects of nominal maximum aggregate size (NMAS) and traffic levels, respectively, on field density values. A correlation analysis is then conducted to identify the significant correlations between the compactability and material properties. The identified correlations can be used to design more compactable mixtures.

2.2 Project Information

Data obtained from fifteen MnDOT projects constructed in 2018 and 2019 were used in the investigation. All mixtures were designed using the current Superpave volumetric mixture design method[12] to 4% of design air voids at a designed number of gyration (N_{design}). The N_{design} value varies from state to state[42]. In Minnesota, the N_{design} for traffic level 3 (1-3 million ESAL), 4 (3-10 million ESAL), and 5 (10-30 million ESAL) are 60, 90, and 100, respectively[43]. All mixtures were used in the wearing course and contained reclaimed asphalt pavement (RAP), ranging from 17% to 30% by weight.

Table 2.1 details the mix design information of the seven mixtures with NMAS = 9.5mm; two of them are level 3, and the other five are level 4. Table 2.2 details the mix design information of the eight mixtures with NMAS = 12.5mm; three are level 3, three are level 4, and the other two are level 5. For simplification, the mixtures with nominal maximum aggregate size (NMAS) of 9.5mm were labeled A, and the 12.5mm mixtures were labeled B. The mixture IDs identify the NMAS and traffic level.

Table 2.1: Information of MnDOT mixtures with NMAS = 9.5mm

Traffic level		Level 3 (1-3 million ESAL)		Level 4 (3-10 million ESAL)				
Mixture ID		A3-1	A3-2	A4-1	A4-2	A4-3	A4-4	A4-5
% Passing of different sieve sizes (mm)	12.5	100	100	100	100	100	100	100
	9.5	92	86	87	96	96	88	88
	4.75	67	67	65	65	65	65	65
	2.36	51	57	50	45	45	53	53
	1.18	36	45	38	32	32	42	42
	0.6	24	30	28	20	20	28	28
	0.3	11	13	15	11	11	14	14
	0.15	6	6	6	5	5	6	6
	0.075	4.5	3.4	3.8	3.4	3.4	3.2	3.2
%AC		5.6	4.9	4.8	5.3	5.3	5.6	5.6
PG		58H-34	58S-28	58V-34	58V-34	58V-34	58H-34	58H-34
RAP Content		20%	30%	20%	19%	17%	22%	15%

Table 2.2: Information of MnDOT mixtures with NMAS = 12.5 mm

Traffic level		Level 3 (1-3 million ESAL)			Level 4 (3-10 million ESAL)			Level 5 (10-30 million ESAL)	
Mixture ID		B3-1	B3-2	B3-3	B4-1	B4-2	B4-3	B5-1	B5-2
% Passing of different sieve sizes (mm)	19	100	100	100	100	100	100	100	100
	12.5	95	90	90	94	92	92	91	90
	9.5	89	76	78	81	80	83	82	81
	4.75	70	57	62	63	60	67	66	65
	2.36	50	45	49	46	40	51	51	50
	1.18	38	35	38	32	27	37	36	34
	0.6	26	26	28	22	19	26	24	22
	0.3	13	13	14	12	11	14	13	12
	0.15	6	6	5	7	6	6	6	5
	0.075	3.6	4.2	2.8	3.5	3.5	3.4	3.3	2.8
%AC		5.5	5.6	5.2	5.3	5.3	5.5	5.1	5.3
PG		58H-34	58S-28	58V-34	58V-34	58V-34	58H-34	58H-34	58H-34
RAP Content		17%	26%	27%	20%	17%	18%	25%	20%

2.3 Material Properties

Field density is mainly affected by mixtures' compactability, which is governed mesoscopically by the properties of the main components of asphalt mixtures. In this study, the following material properties were considered:

- Asphalt content (AC)
- RAP content
- Aggregate gradation
- Aggregate angularity

AC and RAP content are listed in Table 2.1 and Table 2.2. In this section, aggregate gradation and aggregate angularity are further analyzed.

The effect of binder type (modified binder), was not considered in this research, because the 15 projects studied have similar high PG limits, as listed in Table 2.1 and Table 2.2, and did not provide sufficient information for a valid analysis. In addition, the compaction temperatures were determined based on the equiviscous principle[44], which should result in similar binder viscosities at the compaction temperatures.

2.3.1 Aggregate Gradation

Aggregate gradations are listed in Table 2.1 and Table 2.2, and the gradation curves for NMAS=9.5mm and NMAS=12.5mm mixtures are plotted in Fig. 2.1 and 2.2, respectively.

The Bailey method parameters are employed to further quantify the gradations of the investigated mixtures. Bailey method is an empirical method that correlates the aggregate gradation to aggregate packing, which is widely used in mix design for adjusting volumetrics. In Bailey method, aggregates are separated into different portions by three critical sieve sizes: the Primary Control Sieve (PCS), the Secondary Control sieve (SCS), and the Tertiary Control Sieve (TCS). The control sieve sizes are determined using the following relationships: PCS = 0.22*NMAS, SCS = 0.22*PCS, and TCS = 0.22*SCS.

Aggregate gradation is characterized using the following parameters: Primary Control Sieve Index (PCSI), Coarse Aggregate Ratio (CA Ratio), Fine Aggregate Coarse Ratio

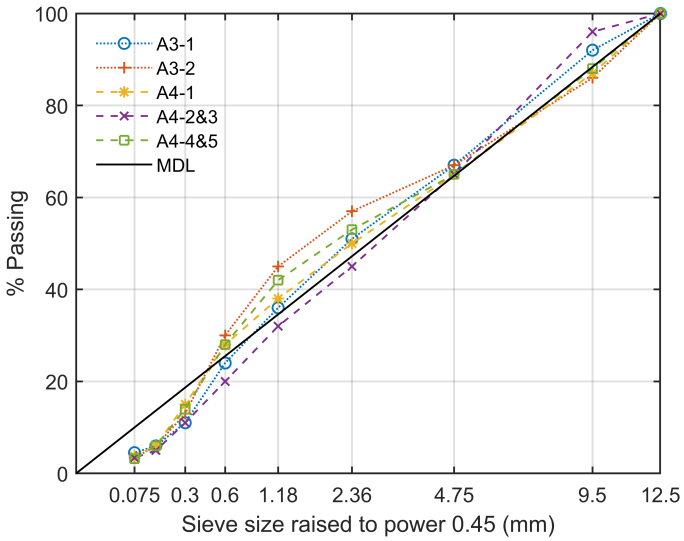

Figure 2.1: Gradation curves of mixtures with NMAS = 9.5 mm.

(FA_c Ratio), and Fine Aggregate Fine Ratio (FA_f Ratio). They are defined by the following formulae[20]:

$$\begin{cases} \text{PCSI} = \%\text{Passing PCS} \\ \text{CA} = \frac{\%\text{Half Sieve}-\%\text{PCS}}{100\%-\%\text{Half Sieve}} \\ \text{FA}_\text{c} = \frac{\%\text{SCS}}{\%\text{PCS}} \\ \text{FA}_\text{f} = \frac{\%\text{TCS}}{\%\text{SCS}} \end{cases} \tag{2.1}$$

where the Half Sieve is the sieve size equal to 0.5*NMAS.

PCSI characterizes the overall fineness of all aggregates, CA characterizes the fineness of the coarse aggregates (aggregates larger than PCS), FA_c characterizes the fineness of the coarse portion of fine aggregates (aggregates larger than SCS but smaller than PCS), and FA_f characterizes the fineness of the fine portion of fine aggregates (aggregates smaller than SCS).

In addition to Bailey method parameters, we also calculate another parameter called the distance to maximum density line (d_{MDL}), that is defined as the accumulated difference of the

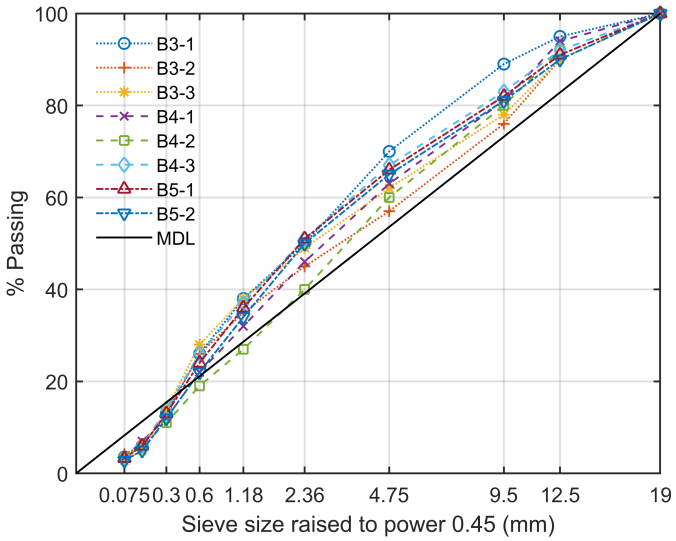

Figure 2.2: Gradation curves of mixtures with NMAS = 12.5 mm.

passing rate between the gradation curve and the maximum density line ($100 \times (\frac{D_i}{D_{max}})^{0.45}$):

$$\mathrm{d_{MDL}} = \sum_{i=1}^{\text{number of sieves}} \left| \%\text{Pass of sieve i} - 100 \times (\frac{D_i}{D_{max}})^{0.45} \right| \tag{2.2}$$

This is based on previous research that showed that mixture compactability is related to how close the gradation curve is to the maximum density line[40, 19].

The values of Bailey method parameters and $\mathrm{d_{MDL}}$ are listed in Table 2.3.

2.3.2 Aggregate Angularity

In the current MnDOT specification[43], aggregate angularity is quantified by three parameters, the Fine Aggregate Angularity (FAA) (AASHTO T304 Method A)[45], Coarse Aggregate Angularity of one face (CAA1) and Coarse Aggregate Angularity of two faces (CAA2) (ASTM D5821)[46].

The physical meaning of FAA value is the volume fraction of fine aggregate in special packing state obtained using AASHTO T304 Method A. CAA1 and CAA2 values represent the mass percentage of particles having at least the required number of fractured faces, respectively.

Table 2.3: Bailey method parameters for MnDOT mixtures

Mixture ID	PCSI (%)	CA	FA_c	FA_f	d_{MDL}
A3-1	51	0.48	0.47	0.19	33.46
A3-2	57	0.3	0.53	0.11	49.32
A4-1	50	0.43	0.56	0.14	27.92
A4-2	45	0.57	0.44	0.17	41.16
A4-3	45	0.57	0.44	0.17	41.16
A4-4	53	0.34	0.53	0.11	35.52
A4-5	53	0.34	0.53	0.11	35.52
B3-1	50	1.08	0.52	0.14	81.97
B3-2	45	0.49	0.58	0.16	42.37
B3-3	49	0.55	0.57	0.1	59.77
B4-1	46	0.72	0.48	0.16	52.07
B4-2	40	0.78	0.48	0.18	41.59
B4-3	51	0.75	0.51	0.13	69.17
B5-1	51	0.69	0.47	0.14	64.27
B5-2	50	0.67	0.44	0.13	58.77

Aggregate angularity increases with traffic level. The required minimum FAA for traffic level 3, 4 and 5 are 42%, 44% and 45%, respectively. The corresponding values for CAA1 are 55%, 85% and 95% respectively. There is no minimum requirement of CAA2 for traffic level 3, while for traffic level 4 and 5, the required minimum CAA2 values are as 80% and 90%, respectively[43].

The values of the angularity parameters, obtained from the quality control and quality assurance (QC&QA) data, are listed in Table 2.4.

2.4 Statistical Analysis of Field Density

A total of 1354 density values from field cores were collected from the QC&QA phase of the 15 projects. The density of a field core was determined by the test method, AASHTO T166[47], if it does not contain open or interconnecting voids. Otherwise, it was determined by the test method, ASTM D1188[48]. The probability distribution of the field densities is first analyzed. Then, an analysis of variance (ANOVA) is conducted to identify if traffic levels and NMAS have any significant effect on field densities. In Minnesota, 92% G_{mm} is the minimum requirement of the as-constructed field density for the 4% air voids Superpave mixtures. A compaction lot with field density less than 92% G_{mm} will be penalized while

Table 2.4: Aggregate angularity for MnDOT mixtures

Mixture ID	FAA (%)	CAA1 (%)	CAA2 (%)
A3-1	42.6	91.4	NA
A3-2	NA	NA	NA
A4-1	44	91.04	87.86
A4-2	44.63	91.88	91.13
A4-3	44.5	92	91.4
A4-4	43.8	96.1	95.8
A4-5	44.04	97.91	97.91
B3-1	42.67	84.33	NA
B3-2	42	99	99
B3-3	42	96.5	NA
B4-1	44.1	98.4	97.5
B4-2	44.9	98.9	97.8
B4-3	NA	NA	NA
B5-1	45.69	98.53	98.53
B5-2	45	97.88	97.88

Table 2.5: Basic statistics of field density data

Statistics	Mean (%)	Median (%)	Std. (%)	Skewness	Kurtosis
Value	93.4	93.5	1.45	-0.44	3.68

bonus will be given if the field density is greater than 93% G_{mm}.

2.4.1 Probability Distribution

The probability distribution of all field core density data is plotted in Fig. 2.3. The basic statistics are listed in Table 2.5.

As shown in Fig. 2.3, field densities approximately follow normal distribution, with a mean of 93.4% G_{mm} and a standard deviation of 1.45% G_{mm}. As listed in Table 2.5, the skewness, -0.44, indicates that the distribution is a bit left-skewed (skewness < 0), which means that the distribution is denser in the right side (higher density side) or has a longer tail in the left side (low density side). The kurtosis, 3.68, indicates that the distribution is a bit leptokurtic (kurtosis > 3), which means that the peak of the distribution is a bit taller than the normal distribution. The left-skewed and leptokurtic properties can be seen from the overall shape of the histogram under scrutiny[2].

[2]The origin of the left-skewed and leptokurtic features are discussed in Chapter 6

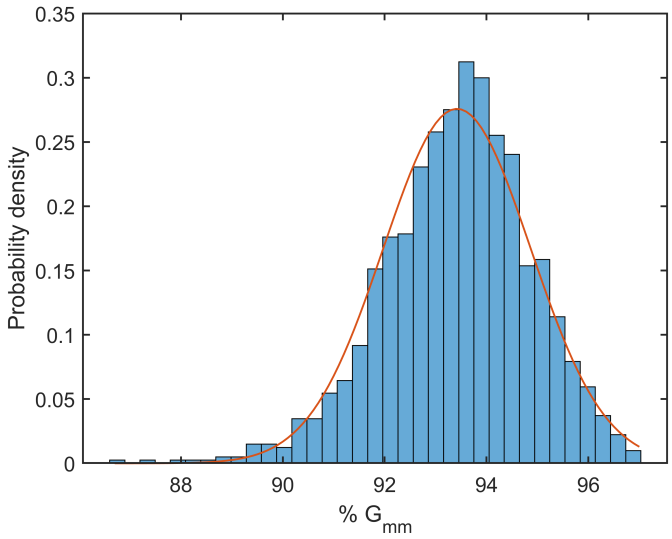

Figure 2.3: Probability distribution of field density data. (The red curve is a normal distribution regression of the data).

To further check the normality of the distribution of the overall data, a q-q (quantile-quantile) plot is drawn in Fig. 2.4. Again, it reveals the left-skewed property of the overall data, while in the middle range, from 91% to 96% G_{mm}, the distribution matches the normal distribution very well.

The cumulative distribution of the overall density data is plotted in Fig. 2.5. It shows that 16% of the field cores are less dense than the minimum MnDOT requirement, 92% G_{mm} [43]. The vast majority (87%) of field cores are less dense than 95% G_{mm}, which is considered as the desired field density level [40, 19] for a Superpave 5 mixture. Therefore, to achieve this desired field density level, most of the current mixtures need to be redesigned to improve their field compaction.

The field density distribution of each project is also analyzed. It is found that all projects approximately follow normal distribution. The boxplots of field densities of each mixture are shown in Fig. 2.6. Their means and standard deviations are summarized in Table 2.6, which will be used later in the correlation analysis in Section 2.5.

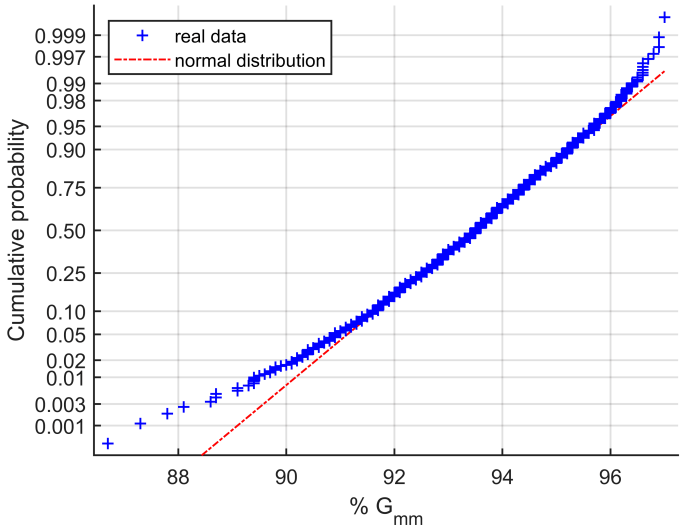

Figure 2.4: Normal distribution q-q plot for field density data.

2.4.2 Analysis of Variance (ANOVA)

The 15 projects can be grouped by their NMAS and traffic level, as is denoted by their mixture IDs shown in Table 2.1 and Table 2.2. A two-way ANOVA is conducted in this section to investigate if these two factors have any significant effect on the variation of field densities.

Table 2.6: Mean and standard deviation (std,) of field density data for each mixture

Mixture ID	Mean (%)	Std. (%)	Mixture ID	Mean (%)	Std. (%)
A3-1	94.07	1.5	B3-1	93.77	1.24
A3-2	93.56	1.24	B3-2	94.53	1.11
A4-1	92.87	1.38	B3-3	94.55	0.86
A4-2	93.71	1.14	B4-1	92.85	0.96
A4-3	93.15	0.96	B4-2	93.01	1.04
A4-4	94.56	1.43	B4-3	92.41	1.65
A4-5	93.36	1.22	B5-1	92.69	1.61
			B5-2	93.72	1.38

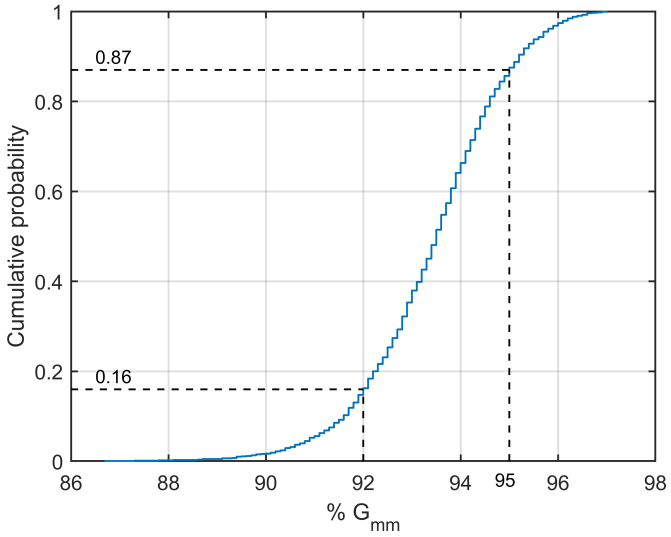

Figure 2.5: Cumulative distribution of field density.

The two-way ANOVA is conducted by testing the following three pairs of hypotheses:

$$\begin{cases} H_{01} : \text{The mean densities of mixtures separeted by NMAS are equal} \\ H_{11} : \text{The mean densities of mixtures separeted by NMAS are not equal} \end{cases} \tag{2.3}$$

$$\begin{cases} H_{02} : \text{The mean densities of mixtures separeted by traffic level are equal} \\ H_{12} : \text{The mean densities of mixtures separeted by traffic level are not equal} \end{cases} \tag{2.4}$$

$$\begin{cases} H_{03} : \text{There is no interaction effect between NMAS and traffic level} \\ H_{13} : \text{There is interaction effect between NMAS and traffic level} \end{cases} \tag{2.5}$$

Results of the two-way ANOVA are shown in Table 2.7. It can be seen that the main effect of NMAS on field density is not significant since its p-value 0.6385 is greater than the significance level 0.05, while the main effect of traffic level and the interaction effect between NMAS and traffic level are significant even at a significance level of 0.001.

The two-way ANOVA indicates whether there is a significant difference caused by NMAS, traffic level and their interaction. To further explore where exactly the significant difference

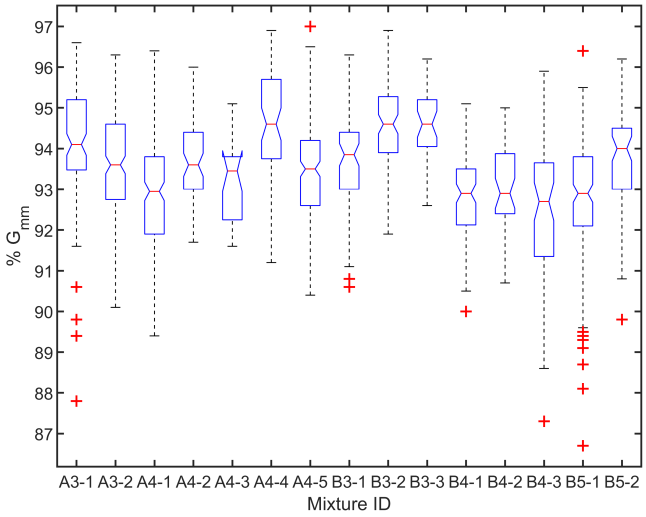

Figure 2.6: Boxplot of field density data of each mixture.

Table 2.7: Two-way ANOVA calculation table

Source of Variation	SS	df	MS	F ratio	p-value
NMAS	0.44	1	0.439	0.22	0.6385
Traffic Level	288.31	2	144.153	72.57	<0.001
NMAS*Traffic Level	79.59	2	39.796	20.04	<0.001
Error	3090.73	1556	1.986		
Total	3405.84	1561			

Note: "NMAS*Traffic Level" represents the interaction between NMAS and traffic level. SS stands for sum of squares. df stands for degrees of freedom. MS stands for mean square.

comes from, a Tukey method multiple pairwise comparison is conducted[49]. The results of the multiple comparison are shown in Fig. 2.7, 2.8 and 2.9 for the main effect of NMAS, main effect of traffic level, and the interaction effect between NMAS and traffic level, respectively. In these figures, circles and stars represent the mean density values of groups, and the error bars represent the 95% confidence interval of the means. Groups shown significant difference in Tukey method multiple comparison are plotted in different colors.

As shown in Fig. 2.7, the main effect of NMAS is not significant, with the means for 9.5mm and 12.5mm NMAS equal to approximately 93.35% G_{mm}. There is, however, a slight downwards trend in field density as NMAS increases.

The main effect of traffic level on field density is shown in Fig. 2.8. Clearly, there is

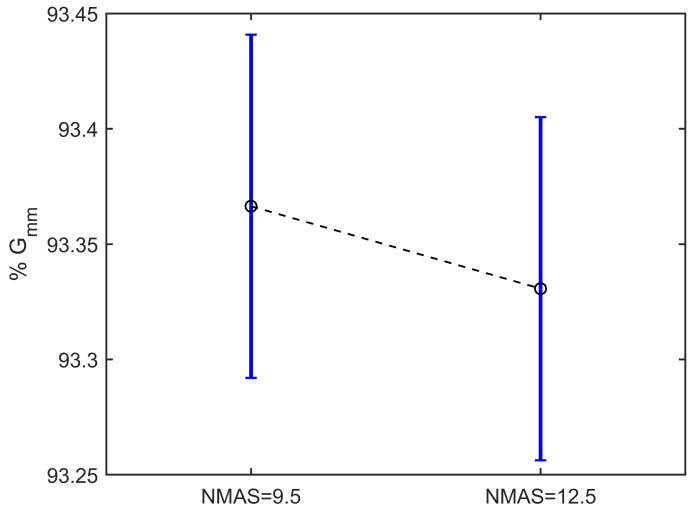

Figure 2.7: Comparison between mixtures grouped by different NMASs.

a downwards trend in field density with the increase in traffic level. Traffic level 3 has significantly higher field density (94% G_{mm}) than traffic level 4 and 5, while traffic level 4 and 5 are not significantly different, with their field densities both around 93% G_{mm}.

The significant effect of traffic level on field density is a result of the different requirements of N_{design} and aggregate angularity for different traffic levels. Higher traffic level mixtures require higher N_{design} and higher aggregate angularity than lower traffic level mixtures. The details of the requirement have been introduced in section 1 and section 3.2. More specifically, requirements of N_{design} and aggregate angularity are more different between traffic level 3 and 4 than that between traffic level 4 and 5, which explains why the field densities are also more different between traffic level 3 and 4, than that between traffic level 4 and 5. This explanation is confirmed later by the correlation analysis in section 5, where significant correlations of field density with N_{design} and aggregate angularity are identified.

The interaction effect between NMAS and traffic level is shown Fig. 2.9. All groups separated by both NMAS and traffic level are significantly different from each other, except for the pair between traffic level 4 & NMAS =12.5 and traffic level 5 & NMAS=12.5. It can be seen that the trend line becomes steeper as NMAS increases from 9.5 to 12.5mm, which means the negative effect of traffic level on field density becomes more significant as NMAS increases from 9.5 to 12.5mm.

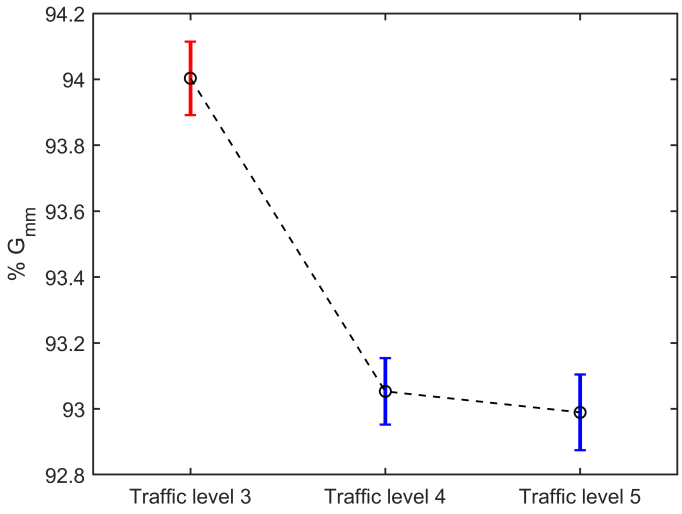

Figure 2.8: Comparison between mixtures grouped by different traffic levels.

2.5 Correlation Analysis

An analysis is conducted to identify the significant correlations between mixtures' compaction properties (represented by field densities (FD) and N_{design}) and material properties. The material properties include the asphalt binder content (AC), reclaimed asphalt pavement content (RAPC), aggregate gradation (characterized by NMAS, CA, FA_c, FA_f, and d_{MDL}), and aggregate angularity (characterized by FAA, CAA1, and CAA2). The meanings of these parameters were previously introduced in section 3.

In this investigation, we interpret FD as an indicator of field compactability since, physically, FD means how dense the mixture can be compacted under a relative consistent field compaction effort. Field compactability of mixtures increases with the increase in FD. Similarly, N_{design} can be interpreted as an indicator of laboratory compactability, since, physically, N_{design} is the laboratory compaction effort (number of gyration) needed to reach the design air voids (4%). A higher N_{design} indicates a less compactable asphalt mixture in laboratory conditions. This interpretation of N_{design} is different from the original one[50] in which N_{design} was related to traffic volume compaction, and, indirectly, to rutting resistance.

Table 2.8 shows the p-value of the correlation analysis. If the p-value of a pair is less than the significance level of 0.05, then we can conclude the correlation of that pair is statistically

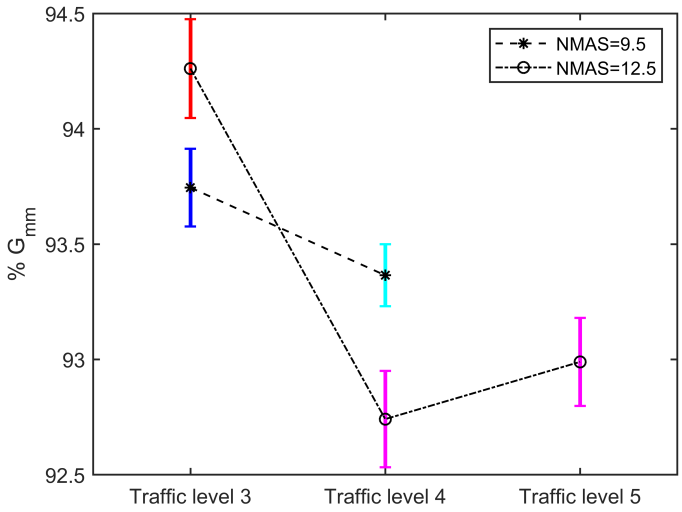

Figure 2.9: Comparison between mixtures grouped by both NMAS and traffic level.

significant. Eleven pairs are shown having significant correlations, and they are shaded in Table 2.8. The correlation coefficients are listed in Table 2.9, and the pairs having significant correlations are again shaded.

Table 2.8: p-values for the correlation analysis

	FD	N_{design}	AC	RAPC	NMAS	PCSI	CA	FA_c	FA_f	d_{MDL}	FAA	CAA1	CAA2
FD	1	0.02	0.164	0.154	0.655	0.722	0.248	0.176	0.546	0.563	0.005	0.87	0.595
N_{design}		1	0.635	0.089	0.984	0.517	0.843	0.042	0.907	0.642	<0.001	0.205	0.715
AC			1	0.135	0.716	0.68	0.621	0.904	0.479	0.855	0.164	0.925	0.077
RAP				1	0.727	0.2	0.158	0.118	0.17	0.778	0.247	0.216	0.428
NMAS					1	0.207	0.003	0.843	0.935	0.001	0.817	0.269	0.019
PCSI						1	0.121	0.303	0.003	0.757	0.685	0.591	0.932
CA							1	0.267	0.317	0.001	0.777	0.235	0.428
FA_c								1	0.047	0.882	0.009	0.922	0.966
FA_f									1	0.35	0.695	0.664	0.722
d_{MDL}										1	0.829	0.535	0.067
FAA											1	0.367	0.877
CAA1												1	<0.001
CAA2													1

Table 2.9: Coefficients of correlation

	FD	N_{design}	AC	RAPC	NMAS	PCSI	CA	FA_c	FA_f	d_{MDL}	FAA	CAA1	CAA2
FD	1	-0.59	0.38	0.39	-0.13	0.1	-0.32	0.37	-0.17	-0.16	-0.73	-0.05	0.19
N_{design}		1	-0.13	-0.45	-0.01	-0.18	0.06	-0.53	0.03	-0.13	0.94	0.38	-0.13
AC			1	-0.4	0.1	-0.12	0.14	-0.03	0.2	0.05	-0.41	0.03	0.58
RAP				1	0.1	0.35	-0.38	0.42	-0.37	0.08	-0.35	0.37	0.28
NMAS					1	-0.35	0.71	0.06	-0.02	0.74	-0.07	0.33	0.72
PCSI						1	-0.42	0.29	-0.71	0.09	-0.12	-0.16	0.03
CA							1	-0.31	0.28	0.77	0.09	-0.35	0.28
FA_c								1	-0.52	-0.04	-0.69	0.03	0.02
FA_f									1	-0.26	0.12	-0.13	-0.13
d_{MDL}										1	-0.07	-0.19	0.6
FAA											1	0.27	-0.06
CAA1												1	0.98
CAA2													1

The significant correlations identified are illustrated in Fig. 2.10. The variables are grouped according to their physical meanings into two categories: compactability and material properties. Material properties are further separated into two categories: aggregate angularity and gradation. The significantly correlated pairs are connected by arrows, and the coefficients of correlation are listed along the arrows.

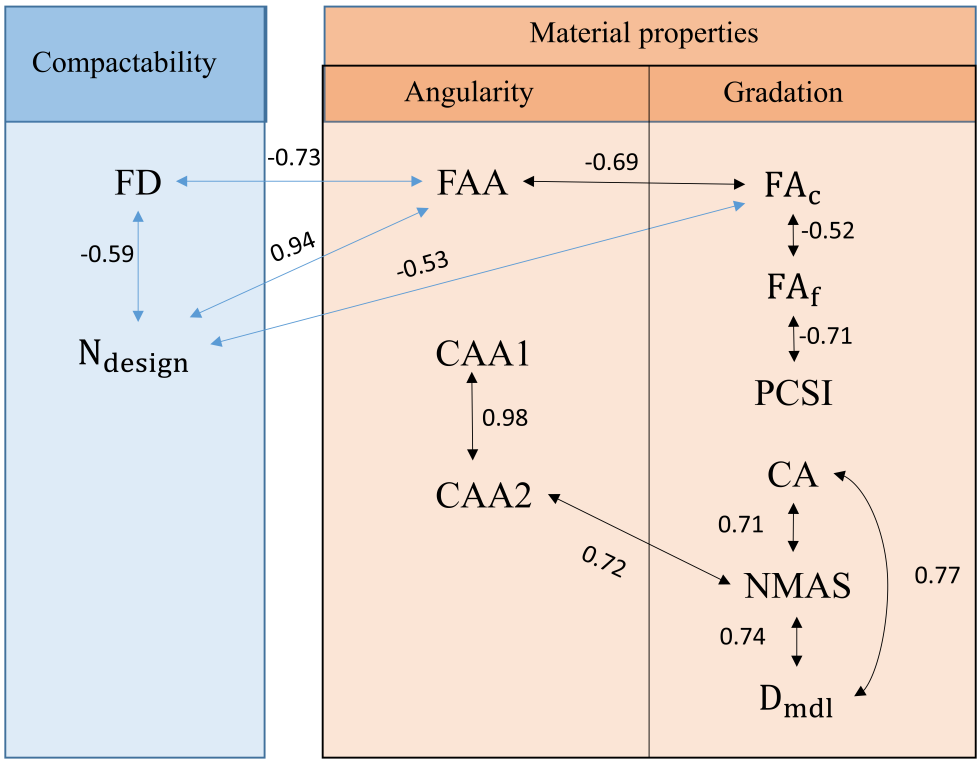

Figure 2.10: Diagram of the identified significant correlations.

It can be seen from Fig. 2.10 that within the category of compactability, FD and N_{design} are significantly correlated, with a negative coefficient of correlation of -0.59. Given that FD and N_{design} represent field and laboratory compactability of mixtures, respectively, their correlation indicates that the laboratory gyratory compaction and field compaction are consistent. In other words, mixtures that compact better in the laboratory also compact better in the field. This finding is critical, because it suggests that field compaction can be reasonably predicted by laboratory gyratory compaction, which lays the foundation for the design of more compactable asphalt mixtures.

The main focus is the correlations between compactability variables and material properties. It can be seen that both field compaction (FD) and laboratory compaction (N_{design}) are significantly correlated to FAA. More specifically, better field and laboratory compaction are achieved with lower FAA. Also, laboratory compaction (N_{design}) and FAA are both significantly correlated to FA_c that characterizes the gradation of the coarse portion of fine aggregate. More specifically, better laboratory compaction is achieved with higher FA_c.

The correlation analysis reveals significant effects of fine aggregate angularity (FAA) and fine aggregate gradation (FA_c) on mixtures' compactability. Both fine aggregate angularity and fine aggregate gradation point to the packing properties of fine aggregates. Mesoscopically, the compactability depends on the packing of aggregate which further depends on aggregate angularity and gradation. Therefore, the identified effects of fine aggregate gradation and angularity on compaction indicate an overall strong effect of fine aggregate packing on compactability. This is not entirely surprising given the fact that in the current test method (AASHTO, T304, method A), FAA actually represents a measure of fine aggregate packing.

These significant correlations suggest that a first step towards designing more compactable mixtures is using a denser fine aggregate packing that can be achieved by decreasing FAA or increasing FA_c. Decreasing FAA, however, may reduce rutting resistance, since the original requirement on FAA was intended to control rutting. Therefore, reducing FAA needs to be combined with other changes to ensure rutting resistance is not affected, such as optimizing coarse aggregate packing, using Bailey method.

In Fig. 2.10, a number of correlations within the material properties are also identified, and are shown the pairs connected by black arrows, in contrast to blue arrows used for pairs in different categories. However, material properties should be independent of each other. For example, CAA2 and NMAS are the coarse aggregate angularity and aggregate size, respectively. They are clearly independent because physically aggregates can have any angularity regardless of the particle size. These correlations are artificial and are a result of the low representativeness of the sampling. For example, the positive correlation between CAA2 and NMAS shows that the mixtures investigated happen to have more angular coarse aggregates as their NMAS increases. Also, the 15 mixtures investigated use similar aggregates and similar gradations, which could be another reason for these significant correlations between material properties.

2.6 Conclusions

In this research work, the current situation of field densities in Minnesota was investigated, to identify possible changes to the current mix design to improve field compactability. The following conclusions were drawn from this study.

1. The as-constructed field density data obtained from 15 projects in Minnesota, approximately follows a normal distribution, with a mean of 93.4 % G_{mm}, and a standard deviation of 1.45 % G_{mm}.

2. The vast majority (87%) of field cores are less dense than 95% G_{mm}, which is considered the desired field density level for a Superpave 5 mixture. Therefore, to achieve this desired field density level, most of the current mixtures need to be redesigned to improve their field compaction.

3. Field densities vary significantly between mixtures designed for different traffic levels. Higher field densities are achieved for mixtures designed for lower traffic levels, which can be attributed to the different requirements for N_{design} and aggregate angularity compared to mixtures designed for higher traffic levels.

4. Field density is significantly correlated to N_{design} of mixtures. Higher field density is achieved with lower N_{design}, which shows the consistency between field compaction and laboratory compaction, and indicates that field density can be controlled in the mix design phase by choosing an appropriate N_{design}.

5. Field density is significantly correlated to fine aggregate angularity and fine aggregate gradation. Higher field densities are achieved using a lower fine aggregate angularity and a finer coarse portion of fine aggregate. Both fine aggregate angularity and fine aggregate gradation affect fine aggregate packing.

The results of this research indicate that a possible way to design more compactable mixtures is to optimize fine aggregate packing to improve compactability, while concurrently optimizing coarse aggregate packing to ensure that rutting resistance is not sacrificed.

Chapter 3

Effect of Tribological Property of Asphalt Binder on Compaction of Hot Asphalt Mixtures[1]

Recent studies proved that the addition of small percentages of graphite nanoplatelets (GNPs) could significantly reduce the compaction effort required to densify HMA. Viscosity measurements showed, however, that the addition of GNPs increased the viscosity of the binder. This observation pointed towards the presence of a different mechanism responsible for the reduction of compaction effort. A new test method, used for lubricants and based on tribology, has been recently proposed in order to characterize the lubricating behaviour of asphalt binders. In this study, the tribological characterization of an asphalt binder modified with GNPs is performed. A novel approach, in which aggregate surface microtexture is simulated using rough surfaces of the testing fixtures, shows that indeed the addition of GNPs lowers the friction coefficient, and therefore, enhances the lubrication properties of the binder when mixed with mineral aggregates.

[1]This chapter is adopted from the following manuscript:
T. Yan, L. P. Ingrassia, R. Kumar, M. Turos, F. Canestrari, X. Lu, and M. Marasteanu. Evaluation of graphite nanoplatelets influence on the lubrication properties of asphalt binders. *Materials*, 13(3):772, 2020

3.1 Introduction

Significant efforts have been devoted to developing new types of asphalt pavement materials, which exhibit better mechanical performance and enhanced durability. With the major advance in nanotechnology, there has been an emerging interest in applying nanoscale materials to asphalt pavement materials [52, 53, 54]. Among them, considerable interest has been directed to carbon-based nanomaterials. One common type of such materials is the carbon nanotubes (CNTs). It was shown that the addition of CNTs could reduce fatigue and permanent deformation of asphalt mixtures, enhance the resistance to thermal cracking, and reduce aging [55, 56, 57]. However, the high cost of CNTs makes them unsuitable for large-scale application to asphalt pavements. A much more cost-effective carbon-based nanomaterials is represented by graphite nanoplatelets (GNPs). The GNPs are nano-discs with a sub-micrometer diameter and a thickness of approximately one nanometer. The GNPs are produced from either graphene or natural graphite. If GNPs are prepared directly from graphene, each platelet typically consists of several layers of graphene sheets, which are a single layer of carbon atoms. Depending on its type and carbon purity, the cost of GNPs is around 3 $/lb (i.e. about 6 euro/kg), which is about three times the price of a typical modifier, SBS, but it is significantly lower than the cost of multi-wall CNTs.

In recent studies, Le et al. [31, 32] have shown that the addition of small amounts of GNPs to asphalt binders can significantly improve the cracking resistance of asphalt binders and mixtures at low temperatures. A moderate addition of GNPs of 3% to 6% by weight of the binder resulted in 130% increase in flexural strength. For some asphalt mixtures, the addition of 6% GNP by weight of binder almost doubled the fracture energy. However, one of the most interesting results was the significant reduction in the number of gyrations required to achieve a target air void content. As shown in Fig. 3.1, to reach 95% compaction, mixtures with no GNP, 6% GNP, and 8% GNP need about 30, 40, and 60 gyrations respectively.

Viscosity measurements indicated, however, that the addition of GNPs increased the viscosity of the binder [2]. Such discrepancies between the binder viscosity and the mixture compaction behaviour have been already observed by other authors, who pointed out the drawbacks of an experimental approach based only on the study of viscosity [58, 59]. In addition, other studies [60, 61] have shown that the mixture compactability does not improve linearly as the temperature increases, but, on the contrary, it gets worse above a certain level of temperature, although viscosity decreases progressively with temperature.

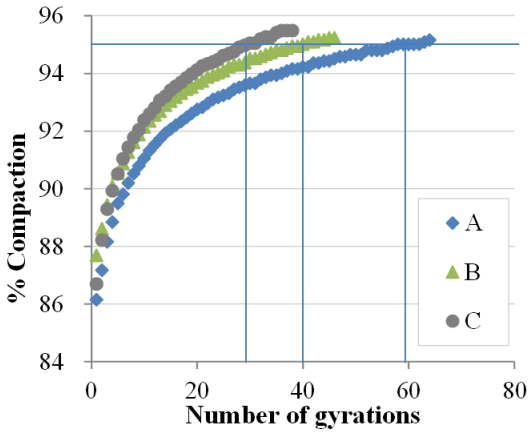

Figure 3.1: Compaction curves for mixtures prepared with asphalt binders with and without GNPs (blend A represents the original PG 58-28 plain binder with no GNP, blend B represents the binder with 6% GNP of binder weight and blend C represents the binder with 8% GNP of binder weight).

Most likely, a different mechanism is responsible for the reduction of compaction efforts. In this regard, a new test method, used for lubricants and based on tribology, has been recently proposed in order to characterize the lubricating behaviour of asphalt binders [62, 63, 64, 65]. In this study, the tribological characterization of asphalt binders modified with GNPs is performed. A novel approach, in which aggregate surface is simulated using rough surfaces of the testing fixtures, shows that indeed the addition of GNPs lowers the friction coefficient, and, therefore, enhances the lubrication properties of the binder.

3.2 Mechanism of Friction and Lubrication

In tribology, the lubrication properties of a material placed between two solids in relative motion is normally described through the Stribeck curve (Fig. 3.2), which shows the evolution of the coefficient of friction μ as a function of the sliding speed [63, 64]. The change in the coefficient of friction values is due to the variation of the thickness of the lubricating film, as shown in Fig. 3.2. The Stribeck curve can be generally divided into four regions, which correspond to different regimes of lubrication [63, 64]:

- the boundary regime (a), occurring when the lubricating film is thin and, consequently, a high μ is determined by the strong interaction between the asperities of the solids;

- the mixed regime (b), where a reduction of μ occurs, because of the increased thickness of the lubricating film, which reduces the direct contact between the solids;
- the elasto-hydrodynamic regime (c), in which the minimum μ is reached, because the thickness of the lubricating film is able to completely separate the solid surfaces;
- the hydrodynamic regime (d), where the film is so thick that there is a new increase of μ, depending on the viscous drag of the lubricant.

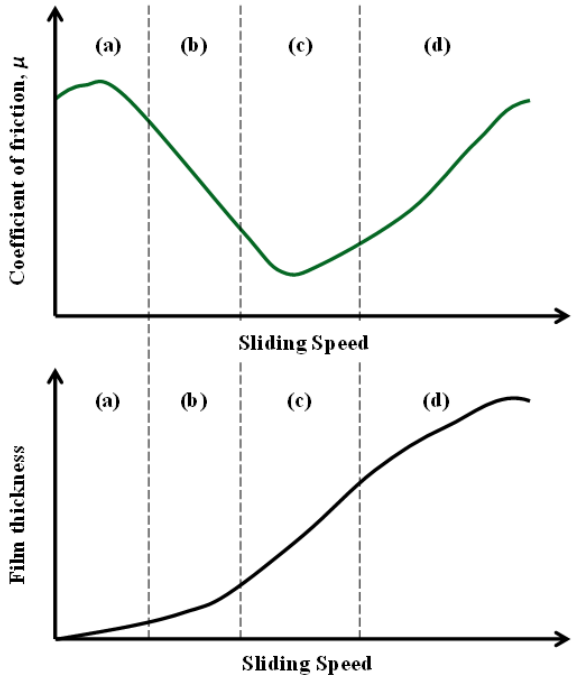

Figure 3.2: Stribeck curve.

However, beside the sliding speed, other important parameters also govern the phenomenon. Since friction is not an intrinsic property of the material but of the overall system, it strongly depends also on the nature, surface roughness and wear of the solids in contact [63, 64]. Such factors are extremely crucial mainly when the lubricating film is not thick enough to separate all solid asperities. Furthermore, the thickness of the lubricating film depends also on the normal load between the solids and, for thermo-dependent materials such as bitumen, on the temperature, which controls the viscosity [64].

Even though the use of nanoparticles to improve the lubrication properties of asphalt mix is new to the world of asphalt binder, their use in the lubrication industry is well established. The role of nanoparticles in friction reduction has been investigated by many researchers and the mechanism involved can be described as follow: rolling effect [66, 67], protective film [68, 69, 70], mending effect [71] and polishing effect [72]. The first two mechanisms belong to the direct effect of nanoparticles on lubrication improvement. Spherical nanoparticles are likely to roll between the frictional surfaces and play the role of ball bearings (Fig. 3.3(a)). In addition, the nanoparticles form a thin protecting film on the surface thereby reducing the friction between two surfaces (Fig. 3.3(b)). The other two mechanisms are the secondary effect of nanoparticles on surface enhancement. The nanoparticles deposit on the frictional surface forming a tribo-film to compensate for the loss of mass known as mending effect (Fig. 3.3(c)). In addition, the roughness of the rubbing surfaces is reduced due to the abrasiveness of the hard nanoparticles known as polishing effect (Fig. 3.3(d)).

For the problem of interest (i.e. the compaction of GNP modified asphalt mixtures), a phenomenon similar to the mending effect is expected to occur, as hypothesised in a previous study [2]. Indeed, GNPs could place between the asperities of the aggregates, providing overall a reduced roughness and therefore an improved lubrication with respect to the base bitumen, as schematized in Fig. 3.4.

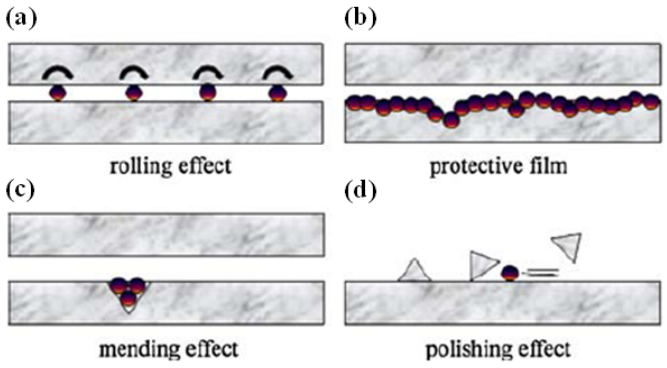

Figure 3.3: Lubrication mechanisms of nanoparticles: (a) rolling effect; (b) protective film; (c) mending effect; (d) polishing effect (from [1]).

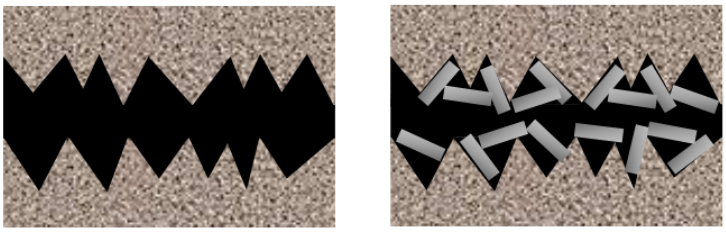

Figure 3.4: Scheme of the bitumen film between aggregate surfaces: (a) without GNPs; (b) with GNPs [2].

3.3 Experimental Investigation

In this study, a plain PG58-28 bitumen was used as base binder. A GNP made of a synthetic graphite material with 99.66% carbon and 0.34% ash, characterized by an enhanced surface area equal to 250 m2/g, was added to the asphalt binder in two proportions: 3% and 6% by weight of the binder. The 3% and 6% blends were prepared at University of Minnesota (USA) using a high shear mixer to better disperse GNP into binder. No clustering of GNPs was observed during the preparation of the samples. The blends were then stored in 85 g cans. Half of the cans were shipped to Nynas (Sweden) to be tested and the other half was kept and tested at University of Minnesota.

Tribological tests were performed using a ball-on-three-plates fixture mounted on a Dynamic Shear Rheometer (DSR). The fixture employed at Nynas is schematized in Fig. 3.5. The coefficient of friction μ is determined according to Eq. 3.1:

$$\mu = \frac{F_{F-TOT}}{F_{N,tribo-TOT}} \tag{3.1}$$

where F_{F-TOT} and $F_{N,tribo-TOT}$ are, respectively, the total friction force and the total normal force experienced by the specimen, calculated as in Eq. 3.2 and 3.3:

$$F_{F-TOT} = 3 \cdot \frac{T}{3 \cdot r_{ball} \cdot \sin\alpha} = \frac{T}{r_{ball} \cdot \sin\alpha} \tag{3.2}$$

$$F_{N,tribo-TOT} = 3 \cdot \frac{F_N}{3 \cdot \cos\alpha} = \frac{F_N}{\cos\alpha} \tag{3.3}$$

where F_N is the axial force of the DSR, T the torque, r_{ball} the radius of the ball and

α the angle between the plates and the horizontal plane (45° for the ball-on-three-plates fixture, see Fig. 3.5). Since the geometry of the fixture is known, in order to determine the coefficient of friction, it is sufficient to impose the axial force and the rotational speed and measure the resulting torque value.

The ball-on-three-plates fixture used at the University of Minnesota is similar to the one presented in Fig. 3.5, but some parts are slightly different from the ones used at Nynas. As shown in Fig. 3.6, the fixture has five different components: a lower cup, three steel plates, a steel ball, a shaft and a ring to attach the ball to the shaft. In the lower cup there are three plates with an angle of 45° with respect to the horizontal plane and the asphalt sample. The steel ball is attached to the shaft, which then gets attached to the DSR head. It is worth pointing out that, unlike the fixture used at Nynas, in which the plates are screwed and therefore perfectly fixed in the lower cup, in the fixture used in Minnesota the plates are not screwed but they are simply placed into three flat grooves in the lower cup (Fig. 3.6(c)). For the abovementioned reason, they have a certain degree of freedom to move at the very beginning of the test, resulting in an initial compliance of the fixture not observed with the equipment used at Nynas, as shown hereafter.

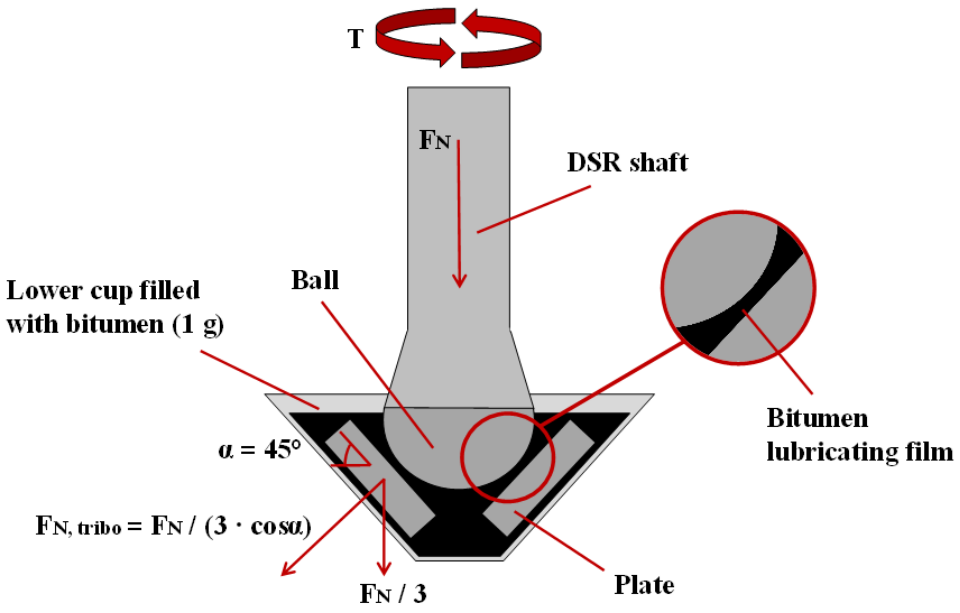

Figure 3.5: Scheme of the tribological fixture used for testing at Nynas (9).

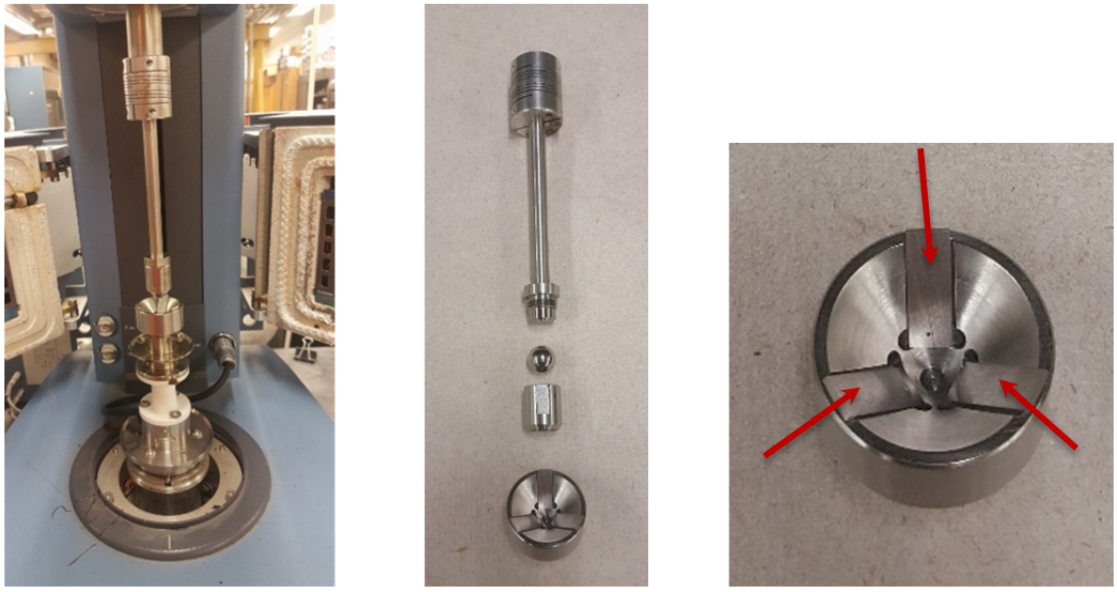

Figure 3.6: Tribological fixture used at University of Minnesota: (a) general view; (b) components of the fixture; (c) lower cup and testing plates.

In order to simulate as much as possible the typical compaction temperatures for hot mix asphalt (HMA) and warm mix asphalt (WMA) mixtures, 110°C, 130°C and 150°C were considered as testing temperatures. All tests were carried out with steel ball and steel plates as substrate. Specifically, the contact points between ball and plates were always different for each specimen, in order to avoid the possible influence of wear and thus reduce the number of variables in the experiments. During the tests, the axial force F_N was kept constant and equal to 10 N, while the rotational speed was increased in logarithmic steps from 0.1 to 1433 rpm. These testing conditions were selected for comparison with previous studies [62, 64]. All tests were performed based on a protocol previously developed by Ingrassia et al. [64].

The experimental investigation also included viscosity tests. In Sweden, the tests were performed using the DSR cone and plate geometry, characterized by a radius of 20 mm and a slope of 2°, while in Minnesota viscosity was obtained with a Brookfield viscometer equipped with the standard SP 27 spindle. The same temperatures as tribological tests (110°C, 130°C and 150°C) were investigated.

All testing performed at Nynas was done using an Anton Paar DSR equipment, while

all tribological testing performed at University of Minnesota was done using an AR 2000 TA Instruments DSR equipment.

3.4 Viscosity Results

As an example, Fig. 3.7 shows the viscosity results obtained at Nynas. As expected, the viscosity values decrease with the increase in temperature. Moreover, it is worth noting that the adopted cone and plate configuration seems reliable for evaluating the shear rate dependency of the binders. In this sense, only for the binder with 6% GNP at 110°C the viscosity value may slightly depend on the shear rate.

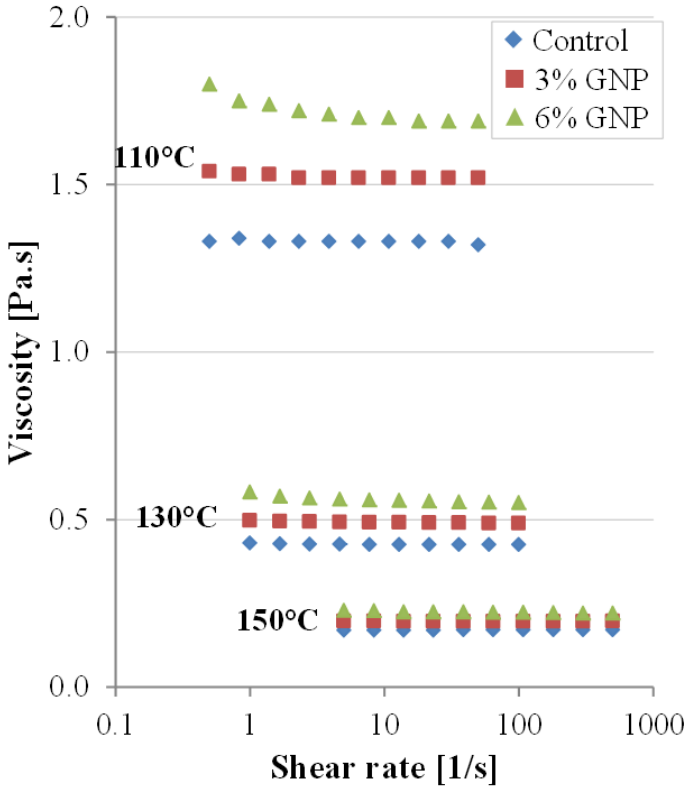

Figure 3.7: Cone and plate viscosity results (Nynas).

Similar results were obtained at the University of Minnesota by using a Brookfield viscometer. Table 3.1 summarizes the average viscosity values at 110°C, 130°C and 150°C, at which Newtonian behaviour could be broadly assumed for all binders. It can be noted that

the viscosity values obtained at Nynas and University of Minnesota are generally comparable. Based on the values of the cone and plate viscosity, the increase in viscosity (with respect to the control bitumen) due to the addition of GNPs is approximately equal to 15% and 30% for the binders with 3% GNP and 6% GNP, respectively, at all testing temperatures. In the case of Brookfield data, the viscosity increase is smaller (around 5-10% for the blend with 3% GNP and about 25% for the blend with 6% GNP).

In summary, these results confirm that the improvement in the workability of GNP mixtures, observed by Le et al. [31, 32], cannot be explained by a viscosity reduction.

Table 3.1: Average viscosity values of the binders tested [Pa·s]

Temperature [°C]	Control (PG58-28)		3% GNP		6% GNP	
	Cone & plate	Brookfield	Cone & plate	Brookfield	Cone & plate	Brookfield
110	1.32	1.28	1.52	1.35	1.69	1.57
130	0.43	0.37	0.49	0.4	0.55	0.48
150	0.17	0.15	0.2	0.16	0.22	0.19

3.5 Tribological Results Using Smooth Surfaces

The tribological results obtained with smooth substrates are shown in Fig. 3.8 (Nynas) and Fig. 3.9 (University of Minnesota). At Nynas, the Stribeck curves were obtained as the average of at least eight replicates (four consecutive replicates on each specimen tested). Specifically, according to the protocol by Ingrassia et al. [64], the first replicate on the specimen was discarded, because it was considered as a "pre-run" to allow the formation of the lubricating film. At University of Minnesota, the Stribeck curves were obtained similarly, by discarding the first replicate and considering the average of the five subsequent replicates on the specimen.

In Fig. 3.8, the boundary (a), mixed (b) and elasto-hydrodynamic (c) regimes can be qualitatively identified according to Fig. 3.2. From Fig. 3.8(a), it can be observed that, at 110°C, the three lubrication regimes are identified at very low, intermediate and high speeds, respectively. With the temperature increase, the same lubrication regimes are identified for progressively higher values of speed (Fig. 3.8(b)-(c)), due to the lower viscosity of the binder. Moreover, a general lubrication improvement is achieved by increasing the temperature, since the values of μ are between 0.08 and 0.22 at 110°C, between 0.06 and 0.18 at 130°C and

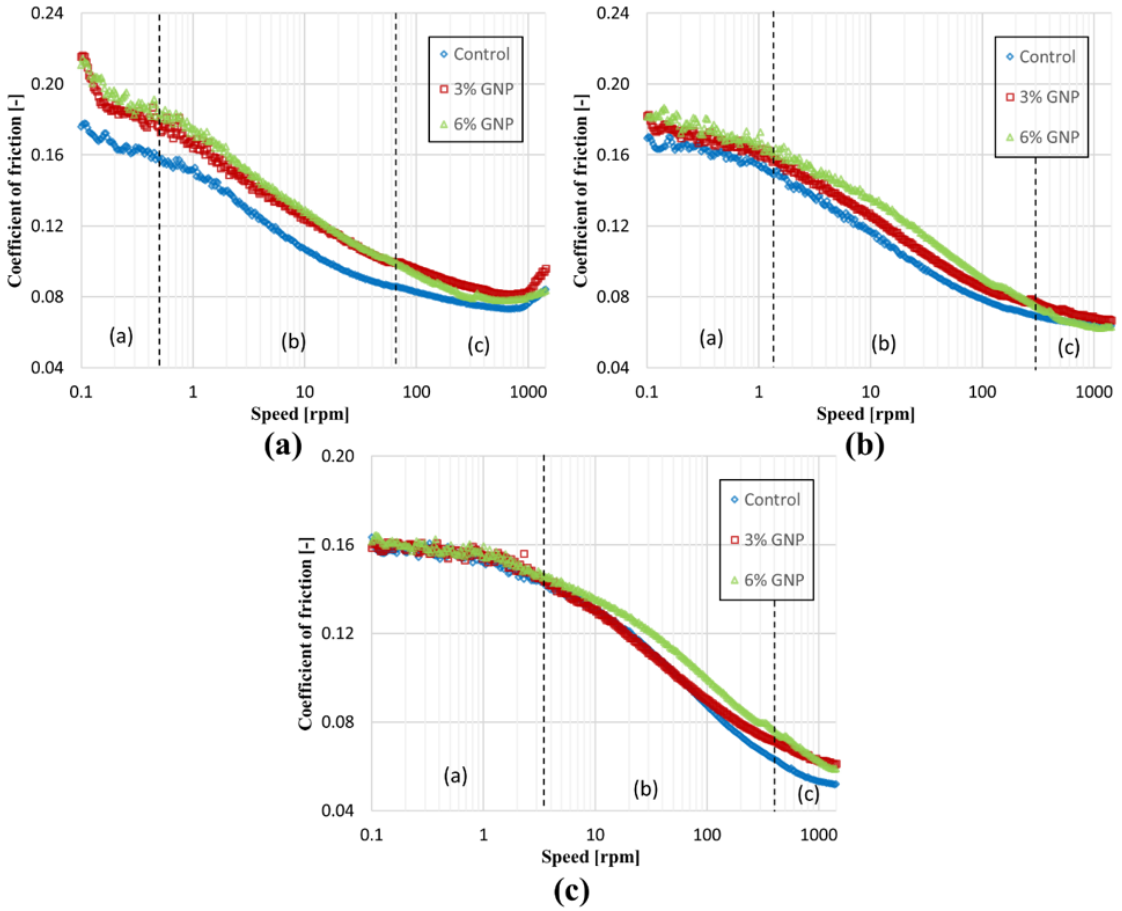

Figure 3.8: Tribological results with smooth surfaces obtained at Nynas: (a) 110°C; (b) 130°C; (c) 150°C.

between 0.05 and 0.16 at 150°C (Fig. 3.8). As for the results from University of Minnesota (Fig. 3.9), the same regimes are observed as well as their shift towards higher speeds when temperature increases. However, the intervals of speed related to every lubrication regime are relatively different as compared to Nynas results. In addition, in general, lower values of μ were obtained in Minnesota with respect to those obtained in Sweden, probably because of the slightly different properties of the ball and plates provided by the two manufacturers (and, more generally, due to the differences between the devices employed). Nevertheless, the determination of the absolute value of the friction coefficient is not the main focus of this study, whose objective is primarily to evaluate the effect of GNP modification (which is

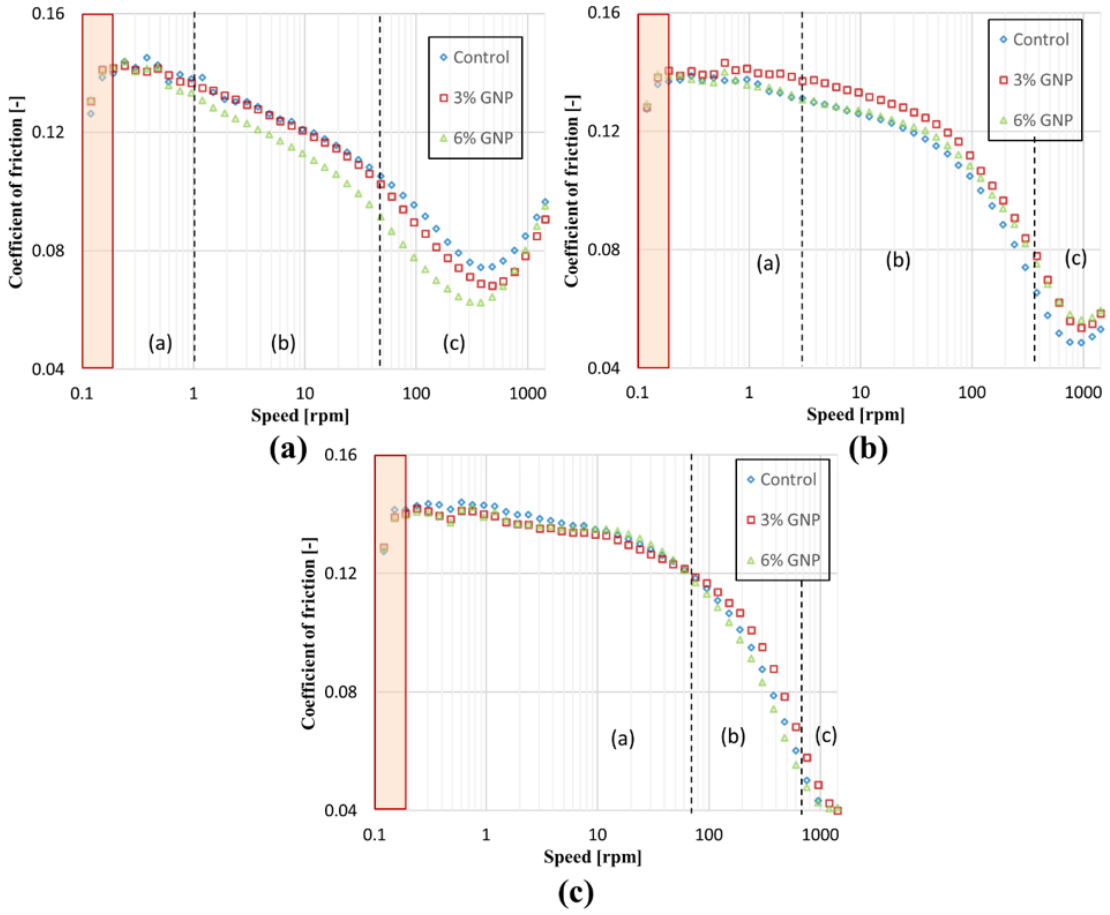

Figure 3.9: Tribological results with smooth surfaces obtained at University of Minnesota: (a) 110°C; (b) 130°C; (c) 150°C.

discussed below). It has also to be noted that the main difference between the values of μ measured at Nynas and those measured at University of Minnesota is at very low speeds ($\leq$ 0.2 rpm), in the region highlighted in Fig. 3.9. As already explained above, this difference is due to the fact that the fixture employed in Minnesota shows a certain compliance at the beginning of the test because of the sliding of the plates. Consequently, these results should be neglected. Also in this case (as for the Nynas results), a slight reduction of friction is observed as temperature increases, especially in the elasto-hydrodynamic regime (c) (Fig. 3.9).

As far as the comparison between the binders is concerned, a general increase of the

coefficient of friction is observed for all temperatures and lubrication regimes after the addition of GNPs in the case of Nynas results (Fig. 3.8). Specifically, the blend with 3% GNP generally exhibits intermediate values of μ as compared to the control bitumen and the blend with 6% GNP. On the contrary, in terms of ranking of the binders, a clear trend linked to GNP content cannot be observed from the University of Minnesota results (Fig. 3.9). It is also worth noting that, in general, the differences between the blends seem smaller with the increase in temperature (Fig. 3.8 and Fig. 3.9).

Overall, it can be stated that the testing protocol adopted in Sweden as well as in Minnesota leads to consistent results and the proposed test method (adapted from the lubricants' field) is appropriate to investigate the lubricating properties of asphalt binders, with or without any kind of modification.

However, in both cases (Fig. 3.8 and Fig. 3.9), the possible improvement of the lubrication properties of the control binder due to the addition of GNPs is not observed, at least for the testing conditions considered.

As a possible interpretation of these results, Fig. 3.10 shows a direct correlation between the viscosity and the minimum coefficient of friction measured in the elasto-hydrodynamic regime (c) for all binders and temperatures, based on the results obtained at Nynas. The high value of the correlation coefficient R^2 indicates that in the elasto-hydrodynamic regime (c) the lubricating behaviour of the material mainly depends on its viscosity, as already observed by Ingrassia et al. [64] in a previous study on WMA binders. Therefore, given the increased viscosity obtained after the addition of GNPs, the potential lubrication improvement cannot occur in this regime. In addition, it is unlikely that during the compaction of the asphalt mixture a thick film of bitumen completely separates aggregates (as it would happen in the hydrodynamic regime (d)), because of the high working temperatures normally adopted. Consequently, a possible reduction of friction due to GNPs should be sought in the boundary (a) and mixed (b) regimes, in which, however, the influence of the substrate properties is crucial.

Based on such considerations, a second testing phase was carried out, as described in the following section.

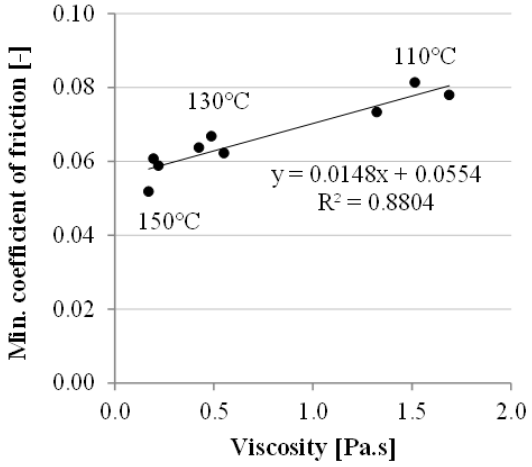

Figure 3.10: Correlation between minimum coefficient of friction and viscosity, based on Nynas results.

3.6 Tribological Results Using Rough Surfaces

During the first part of this study, the original manufactured geometry was used on both DSR devices, in which the ball and the plates have shiny and smooth surfaces. However, the use of smooth surfaces is not representative of the surface roughness of natural aggregates in asphalt mixtures. In the second testing phase, the surfaces of the ball and of the plates were roughened to better simulate the surface of the aggregates. The method consisted in immersing the ball and the plates in hydrochloric acid (HCl) for three days. Hydrochloric acid corroded the surfaces of the parts and made them rough and looking like an orange skin. Fig. 3.11(a)-(b) present the original smooth ball and plate, whereas Fig. 3.11(c)-(d) present the ball and plate after they were removed from the acid.

Also for these tests, the contact points between ball and plates were always different for each specimen to avoid the influence of wear. During all the tests, the axial force was kept constant and equal to 10±0.1 N, while the rotational speed was increased in logarithmic steps from 0.01 radian/sec (≈ 0.1 rpm) to 150 radian/sec (≈ 1433 rpm), analogously to the previous experimental phase. All tests were carried out at University of Minnesota.

The test performed using the ball and three plates with rough surfaces resulted in a different output. The adoption of rough surfaces (Fig. 3.12) implies–as somehow expected–a significant increment of the coefficient of friction, which is up to three times higher (even

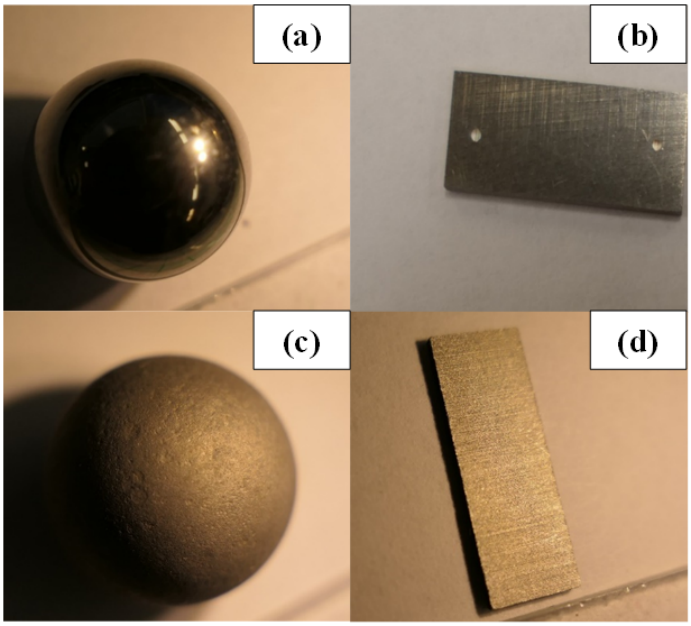

Figure 3.11: (a) smooth ball; (b) smooth plate (used); (c) rough ball; (d) rough plate.

more at 150°C) as compared to the case of smooth substrates (Fig. 3.9). A change in the lubrication regimes can be also noted with respect to Fig. 3.9, as the boundary (a) and mixed (b) regions are identified at all temperatures, but the distinction between them is not very clear from the shape of the curves (Fig. 3.12). In addition, at all temperatures, the minimum of the Stribeck curve is not reached for any binder, probably because under such conditions the complete separation between the solid asperities is harder to be achieved and the minimum shifts towards higher speeds, even though the mixed (b) regime tends to the elasto-hydrodynamic (c) one at high speeds. As already noticed for the smooth substrate (Fig. 3.9), also in this case the values of μ measured at low speeds should be neglected, due to the sliding of the plates in the lower cup. For the rough surfaces, however, the initial value of μ at low speeds is around 0.2 for all binders and temperatures (Fig. 3.12), whereas for the smooth substrate this value was around 0.12 (Fig. 3.9). Such different values somehow provide a measure of the friction given by the steel-on-steel contact, which is obviously higher for the rough surfaces and almost independent from the testing temperature. Moreover, the speed range where the possible sliding of the plates occurs gets wider with the temperature increase (up to about 0.3 rpm at 110°C, 0.4 rpm at 130°C and 0.6 rpm at 150°C, as

highlighted in Fig. 3.12). It is interesting to observe that, contrarily to what emerged in the case of smooth substrates (Fig. 3.8 and Fig. 3.9), the coefficient of friction remarkably increases for all binders as the testing temperature is increased, especially in the boundary regime (a). This is probably due to the fact that the decrease of the binder viscosity allows a greater contact between the solid asperities, resulting in higher friction. This finding suggests that a temperature increase may not always be beneficial for the compaction of the asphalt mixture.

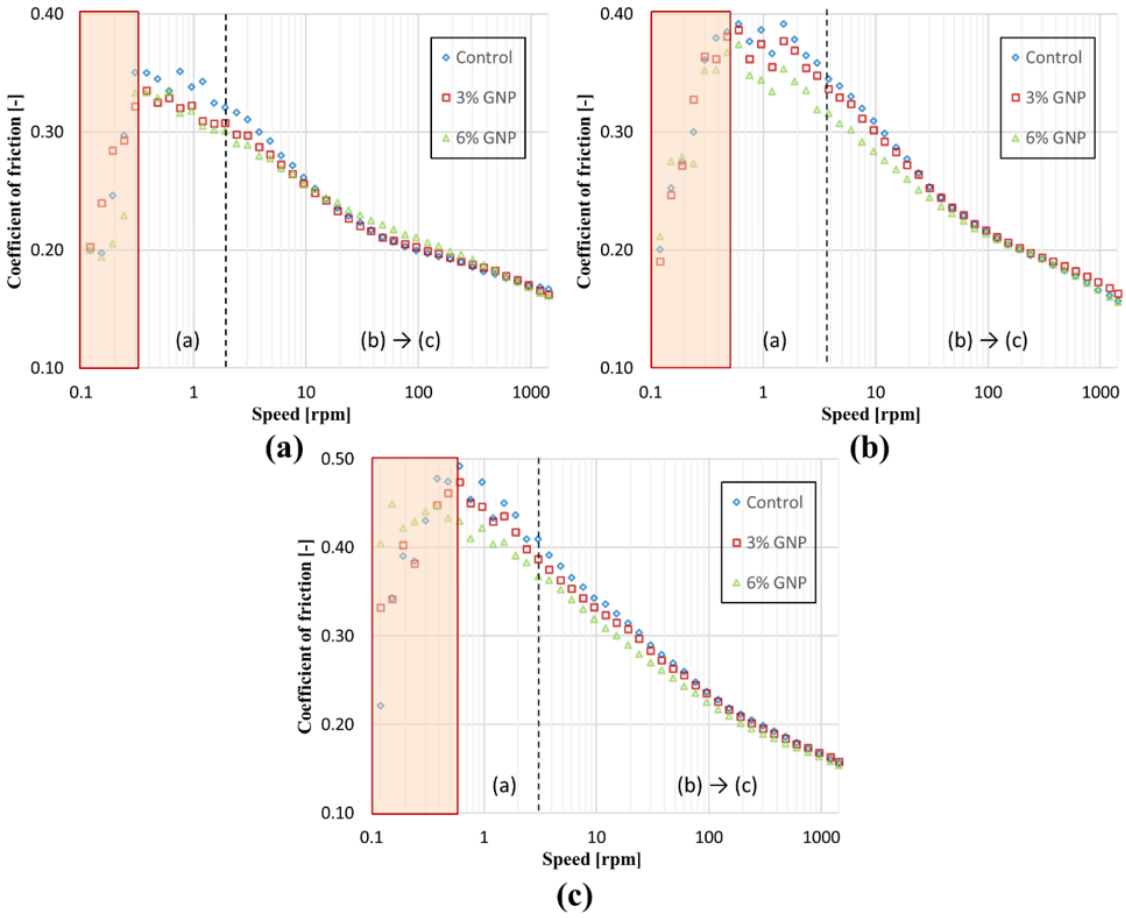

Figure 3.12: Tribological results with rough surfaces (University of Minnesota): (a) 110°C; (b) 130°C; (c) 150°C.

As for the effect of GNP modification, at all three temperatures the coefficient of friction is reduced by the addition of GNPs in the boundary (a) as well as in the mixed (b) regime

(Fig. 3.12). At all temperatures, the lubrication properties of the binder are progressively improved as the GNP amount increases. Specifically, the friction reduction with respect to the control bitumen increases with the temperature and it is about 20% for the blend with 6% GNP at 150°C. Conversely, the results are almost the same for all blends once the speed increases and the regime tends to the elasto-hydrodynamic (c) one.

These results provide a possible explanation for the reduced compaction effort required to densify HMA with GNPs observed in previous studies [31, 32]. During the compaction process, the aggregates move with a small relative speed, which is probably comparable to the boundary (a) and mixed (b) speed regime of this test, and, thanks to an effect similar to the mending one, the nanoparticles stored on the aggregates' rough surface improve the compaction properties of asphalt mixtures.

3.7 Conclusions

The objective of this study was to examine the effect of graphite nanoplatelets (GNPs) on the lubricating behaviour of asphalt binders in an attempt to correlate the lubrication properties of the GNP modified binder with the enhanced compactability observed for GNP modified asphalt mixtures. Three binders were tested: the PG 58-28 binder (control), the PG 58-28 binder with 3% of GNP by weight, and the PG 58-28 with 6% of GNP by weight. Both viscosity and tribological tests were conducted to study the viscous and lubricating behaviour of the binders, respectively. In the tribological experiments, smooth and rough substrates were considered.

It was observed that the viscosity of the binder increases with the quantity of GNPs. This observation confirmed that the reduced compaction efforts for GNP asphalt mixtures cannot be attributed to the reduction in the viscosity of the binder. From the tribological tests, it was found that GNPs do not improve the lubricating behaviour of the binder in the case of smooth substrates. Conversely, when rough substrates were considered, the lubrication properties of the binder were progressively improved in the boundary and mixed regimes as the GNP amount increased. Since the rough substrate mirrors the actual aggregate roughness more accurately than the smooth substrate, the enhanced workability of GNP modified mixtures can be attributed to the fact that GNPs may occupy the space between the asperities of the aggregates, reducing the overall roughness and thus improving the lubrication. Moreover, the tribological tests performed with rough substrates demonstrated

that, for a given binder, friction increases significantly as the temperature increases (i.e. the viscosity decreases), especially in the boundary regime. This finding once again confirms that the viscosity is not the only parameter involved in the compaction of asphalt mixtures, as the interaction between the aggregates plays a crucial role.

Future research can be focused on: 1) Assess more binders and GNP types with rough surfaces tribological test to further validate this approach; 2) Identify a representative parameter from tribological tests, to characterize the lubrication effect of binder; 3) Investigate more in details the correlation between compactability and tribological test results.

Chapter 4

Mesoscopic Mechanisms of Compaction of Hot Asphalt Mixtures[1]

Compaction of asphalt mixtures is a complex physical process, which has not been fully understood. In this chapter, we investigate the physical mechanisms of compaction, based on which we propose a new method to evaluate the compactability of asphalt mixtures. Two mesoscopic physical mechanisms are introduced. One is related to the jamming of aggregates, which governs the densification process of the mixture. The other is related to the binder-aggregate interaction, which is responsible for the change of shear resistance of mixtures during compaction. Based on these mechanisms, six indices are proposed to characterize the compactability of asphalt mixtures. The proposed indices are applied to analyse seven asphalt mixtures from the test sections of MnROAD research facility. Statistical analysis is performed to identify correlations between mixtures compactability indices and material compositions, such as gradation and binder content. Based on the most significant correlations, multiple linear regression models are developed, which can be used to design more compactable mixtures.

[1]This chapter is adopted from the following manuscript:
T. Yan, M. Marasteanu, and J.-L. Le. Mechanism-based evaluation of compactability of asphalt mixtures. *Road Mater. Pavement Des.*, 22(sup1):S482–S497, 2021

4.1 Introduction

During the construction of asphalt pavements, asphalt mixture is compacted from a loose state to a dense state by a combination of compression, shear and vibration forces. In this process, air voids are extruded out from the mixture and the internal aggregate structure is rearranged to a state such that some level of aggregate interlocking is obtained. Numerous studies have emphasized the paramount importance of compaction in building a durable and resilient pavement [74, 5, 6, 7, 8].

In spite of significant research efforts on compaction, inadequate compaction is still a common problem in current practice. A previous study investigated 40 construction projects in the United States, and it showed that 55% of them had as-constructed densities less than 92% of the theoretical maximum specific gravity, G_{mm}, and 78% projects had as-constructed densities less than desired value of 93% of G_{mm} [11]. The average ultimate density was 94.6% of G_{mm}, which is considerably lower than the design value (96% of G_{mm}). Inadequate compaction has a significant adverse impact on durability, causing pavement distresses such as cracking, moisture damage and raveling to initiate at early ages of pavement service life [11, 38, 10].

The primary reason for inadequate field compaction is the low compactability of asphalt mixtures. In the United States, the currently used Superpave mix design method (AASHTO R35 [12]) was developed in the 1990s to mainly control rutting, which was the most prevalent distress at that time. To prevent rutting, the design emphasized stiffer mixture after construction, while the effect on compactability during construction was mainly disregarded. After the implementation of Superpave, durability related distresses, such as cracking and raveling, became the most prevalent [13].

To ensure good durability of asphalt pavement, the compactability of mixtures must be considered in the design phase. Moutier [14] studied the laboratory gyratory compaction of asphalt mixture and observed an approximate linear correlation between density and logarithm of number of gyrations. Subsequent studies have focused on the energy dissipation during compaction process of asphalt mixtures [35, 16, 17, 18]. Based on the idea of energy dissipation, different energy indices were proposed to evaluate the compactability of mixtures [16, 17, 18]. Though slightly different, the energy indices were all defined as the integration of a certain region of the compaction curve, which are related to the area under the compaction curve. Though the slope of linear correlation and the energy indices serve as global indictors

of the overall compactability of mixtures, they are phenomenological in nature. There is lack of understanding how these indicators are related to the physical mechanisms of the compaction process. To explore the physical mechanism of the compaction process, the concept of locking point was proposed [15]. The locking point is defined as the number of gyration at which aggregates interlock with each other, and further compaction of mixture becomes very hard. While slightly different definitions of locking point have been proposed [15, 75, 36], they all share the same physical interpretation, which is that compaction process essentially stops after aggregates interlocking is achieved. However, locking of aggregates cannot explain how the shear force from the gyratory motion in gyratory compaction affects the compaction. Without shear, the static pressure alone can only compact mixture to a very limited level.

The gyratory compaction is a complex process. At the compaction temperature, the mixture is multiphase, involving solid aggregates, liquid asphalt binder, and air. Also, different phases are coupled; for example, aggregates interact with each other and also interact with the binder. In this paper, we introduce different physical mechanisms to characterize the behavior of the multi-phase compositions of mixtures. Based on these mechanisms, six compactability indices are proposed to characterize gyratory compaction curves. These indices are then used to evaluate the compactability of seven asphalt mixtures used in test sections constructed at the MnROAD research facility.

4.2 Mesoscopic Mechanisms of Compaction

Gyratory compaction of asphalt mixtures is performed under a combination of compression and shear forces. As shown in Fig. 4.1, during gyratory compaction, the asphalt mixture is confined in a cylindrical steel mold and is compressed by the external pressure P and gyratory sheared at an angle α. The direction of the shear is rotating at a rate of ω, called gyration rate. The deformation of material during gyratory compaction can be decomposed into the volumetric deformation and deviatoric deformation (distortion). The density change of materials is a result of the volumetric deformation, while density is conserved during pure distortion. The volumetric and deviatoric behaviors are often assumed to be uncoupled [76]. However, this is not the case for the compaction of asphalt mixture, where the densification and distortion influence each other. On one hand, the density of mixture affects the stress needed to distort the mixture, namely its shear resistance: the shear resistance first increases

and then decreases with the increase in density. On the other hand, the distortion also affects densification; in the gyratory compaction, the rate of densification increases with the increasing amplitude of distortion, which is the angle of gyration α [77].

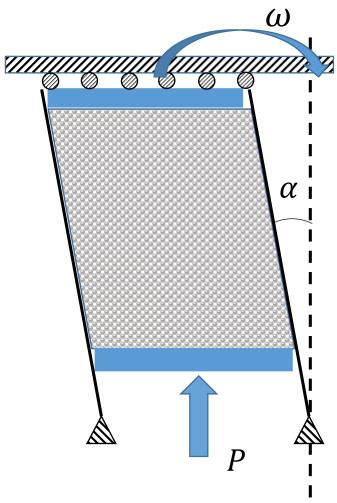

Figure 4.1: Sketch of gyratory compaction

This coupling effect of densification and distortion originates from the material composition of asphalt mixture. In this study, two mesoscopic physical mechanisms are proposed to explain these coupling effects, namely the effect of shear motion on densification process, and the effect of densification on shear resistance. The corresponding physical mechanisms proposed are the jamming of aggregates and the binder-aggregate interaction.

The jamming mechanism was first proposed and discussed in granular physics [78, 79]. However, it has not been used before to investigate the compaction of asphalt mixtures. For this reason, we will first briefly introduce the original concept of jamming, and then describe how the jamming concept can be applied to the compaction process. Since the concept of jamming mechanism was originally proposed for dry granular systems [78, 79], it cannot fully explain compaction process, which also involves interstitial fluid like asphalt binder. Therefore, in this study we propose to consider another mechanism, namely the binder-aggregate interaction, to account for the effect of asphalt binder on compaction. By adding the binder-aggregate interaction, we extend the original jamming concept to granular-liquid systems, such as asphalt mixtures.

4.2.1 Jamming of aggregates

For granular materials, jamming of aggregates is believed to be the main physics accounting for the transition between the fluid-like and solid-like phase [78, 79, 80]. Granular materials, such as sand and aggregates, can flow under vibration or shear, but will jam to a certain state when the intensity of vibration or shear is lowered. A jammed state of aggregates is the state in which aggregates interlock with each other and cannot have any further movement under a static loading.

The jamming process can be illustrated by the jamming phase diagram [79]. As shown in Fig. 4.2(a), jamming is affected by two factors, the volume fraction of aggregate ϕ and the shear resistance τ. The system of aggregates gets jammed when ϕ reaches a critical value ϕ_J. When $\phi > \phi_J$, the system can still get unjammed, by applying a shear force higher than the shear resistance. Note that, by considering the possibility of unjam the system beyond the locking point, we can further explain the effect of shear on the densification process of compaction.

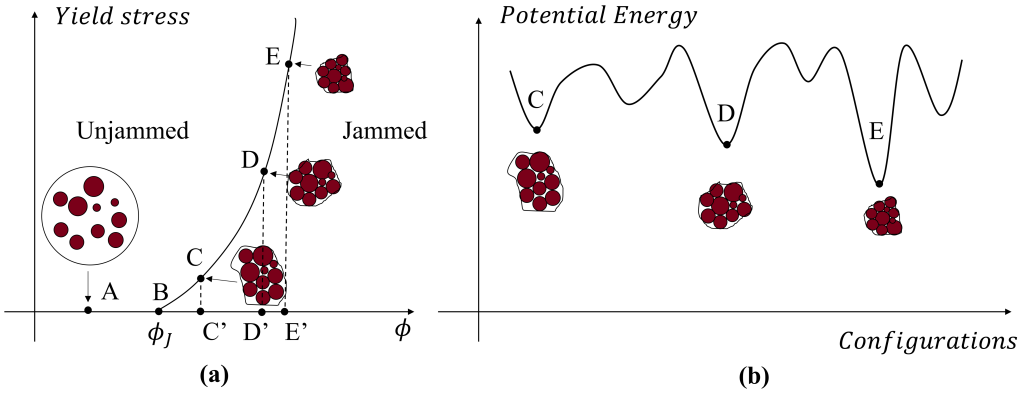

Figure 4.2: (a) Jamming phase diagram, (b) potential energy of different configurations.

The jamming phase diagram is then used to explain the densification process during compaction. As shown in Fig. 4.2(a), when $\phi < \phi_J$, the state represented by point A, the aggregates are separated from each other, and the system can be easily deformed with zero shear resistance, which corresponds to the fluid-like phase. If a static pressure is applied to reduce the total volume of the system, ϕ will increase and reach the critical volume fraction ϕ_J that represents the beginning of the jammed phase. Once ϕ_J is reached (point B), aggregates become jammed, and cannot be further densified by pure static compression.

Therefore, ϕ_J represents the maximum volume fraction of aggregates that the system can reach under static compression.

Once the aggregates are jammed, the system starts to develop shear resistance. To further densify the material, external excitations, such as shear or vibration, need to be applied to overcome the shear resistance to unjam the system, and enable it to evolve to a denser state. This is shown in Fig. 4.2(a): the system evolves from point C to D, and then to E. If the system is at a state represented by point C', a jammed state, it cannot evolve to the denser state D' through the line C' $\rightarrow$ D' directly. Instead, the feasible path is C' $\rightarrow$ C $\rightarrow$ D $\rightarrow$ D', which means that, in order to evolve to point D, the jammed state C' is first unjammed to state C by applying excitations to overcome shear resistance.

The jamming mechanism can also be understood from the analysis of the energy landscape [81], which is also applicable to the compaction of asphalt mixtures. For a system of aggregates, the potential energy provided by the static compression decreases as the volume of the system decreases. Therefore, potential energy decreases with the increase in volume fraction of aggregates ϕ, as shown in Fig. 4.2(b). If aggregates are free to move and rearrange, the whole system tends to evolve to the state with the minimum potential energy, which is also corresponding to the densest state of aggregate packing (greatest ϕ). Each jammed state of aggregates represents a local minimum of the potential energy, as shown in Fig. 4.2(b). Under pure static compression, without external excitations, the system is trapped in that local minimum state. If external shear or vibration is applied, the external energy enables the system to overcome the energy barrier (i.e., enable the aggregates to unjam so that they can rearrange) and move to configurations with lower and lower energy states, which correspond to denser and denser packing states of aggregates. The transition from C to D and E in Fig. 4.2(b) exemplifies this process.

Based on the physical mechanism of jamming, the densification process of compaction can be viewed as the evolving of jammed states of aggregates under the excitation of shear (e.g., laboratory gyratory compaction) or vibration (e.g., vibration roller compaction in the field).

4.2.2 Binder-Aggregate Interaction

The physical mechanism of aggregate jamming explains the effect of shear on densification process, but it cannot fully explain the evolution of shear resistance during compaction. As

shown in Fig. 4.2(a), jamming mechanism alone predicts that the shear resistance increases as the density increases. However, as shown by the experimental data of this study and other studies [35, 16, 17, 36], the shear resistance in gyratory compaction first increases but then decreases with increase in density. In this study, we postulate that the decrease in shear resistance of mixture during the latter part of compaction is caused by the binder-aggregate interaction. To explain the interaction between aggregates and binder, we adopt the pore pressure and effective stress concepts from critical state in soil mechanics [82]. Similar to the role of water in soil, binder in the mixture can also develop pore pressure when most of air voids are extruded out (when ϕ reaches a certain level). The total stress is the sum of effective stress from the solid contact of aggregates and the pore pressure in the liquid binder, i.e.:

$$p = p_{eff} + p_{pore} \tag{4.1}$$

where p is the total stress; p_{eff} is the effective stress; p_{pore} is the pore pressure.

At a constant p, an increase in p_{pore} leads to a decrease in p_{eff}. The shear resistance of granular materials depends on the friction between their constituent particles, and the friction is proportional to p_{eff} [82]. The pore pressure p_{pore} of binder does not contribute to friction, since the binder serves as lubricant in the aggregate-binder system.

We now explain the compaction process of asphalt mixtures by combining the mechanisms of jamming and aggregate-binder interaction. A schematic jamming phase diagram for asphalt mixtures with a certain binder content can be sketched in Fig. 4.3(a). At the beginning of the compaction process, when the mixture is in a relatively loose state, e.g. point C, when mixture is compressed, the binder can flow to occupy the space from available air voids, and pore pressure cannot develop. In the latter phase of compaction, e.g. point D, the available space from air voids has decreased considerably, and the binder has no space to flow and p_{pore} increases. Since the total stress is kept constant during compaction, p_{eff} decreases accordingly, which therefore, causes the decrease of shear resistance.

It should be noted that Fig. 4.3(a) differs from Fig. 4.2(a) because of the binder-aggregate interaction. Since the interaction between aggregates and binder becomes more evident as the binder content increasing, the binder content should be considered as another parameter for the jamming phase diagram of an aggregate-binder system. We therefore propose a more general phase diagram for aggregate-binder system as sketched in Fig. 4.3(b), in which the third axis, the volume fraction of binder (ϕ_{binder}), is added. As shown, when

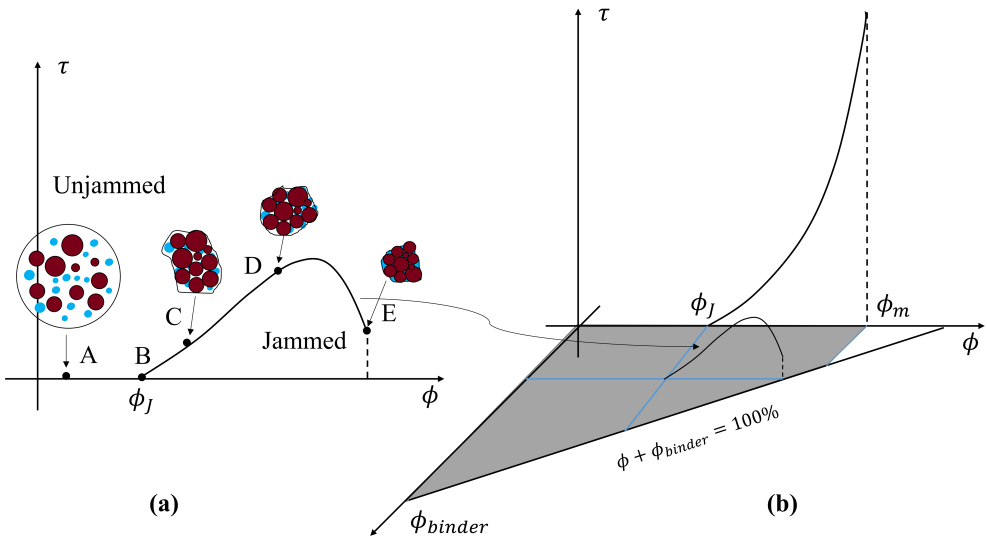

Figure 4.3: (a) Jamming Phase diagram of mixture with a fixed binder content, (b) generalized Jamming phase diagram of the aggregates binder system.

$\phi_{binder} = 0\%$, there is no aggregate binder interaction, so the $\phi - \tau$ relationship returns to that shown in Fig. 4.2(a), whereas for a certain amount of binder content ϕ_{binder}, due to the aggregate binder interaction, the $\phi - \tau$ relationship becomes that shown in Fig. 4.3(a). More generally, τ can be viewed as a function of both ϕ and ϕ_{binder} and can be represented by a surface in the $\tau - \phi - \phi_{binder}$ coordinates.

The feasible domain of ϕ and ϕ_{binder} has to satisfy three additional constrains listed in Eq. 4.2.

$$\begin{cases} 0\% < \phi < \phi_m \\ 0\% < \phi_{binder} < 100\% \\ \phi + \phi_{binder} = 100\% \end{cases} \tag{4.2}$$

The first inequality says that ϕ is bounded by 0% and the maximum volume fraction ϕ_m corresponding to the closest packing of aggregates. The second one says that ϕ_{binder} is bounded by 0% and 100%. The third one says that the volume fraction of binder plus aggregates cannot exceed 100%. Based on these three inequalities, the feasible domain is marked as the grey trapezoid region in Fig. 4.3(b).

Drawing an analogy with soil consolidation, for gyratory compaction of asphalt mixture

the condition can be viewed as undrained, since material is confined in the steel mold. Even for field compaction, where there is no real confinement, due to the high viscosity of the binder, the time scale for binder to drain out is very large compared to the speed of the compaction, therefore, the proposed mechanism of binder-aggregate interaction is applicable to both laboratory gyratory compaction and field compaction.

4.3 Interpretation of Gyratory Compaction Curves and Mechanism-Based Compactability Indices

The two physical mechanisms proposed in the previous section are now used to interpret gyratory compaction curves. Compaction data, obtained from a typical gyratory compaction test, is used in Fig. 4.4(a), (b), and (c) for this purpose.

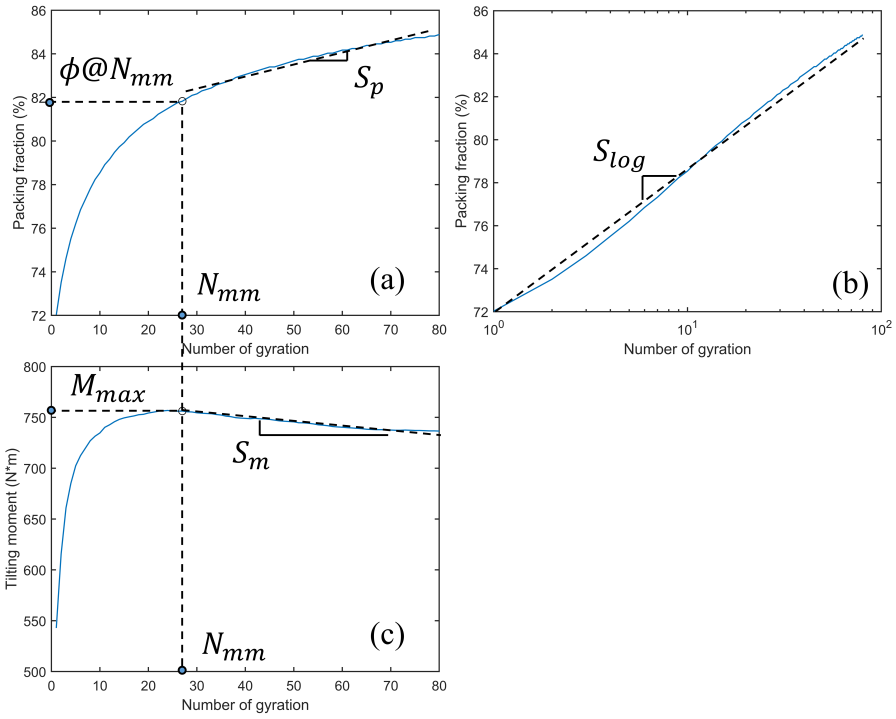

Figure 4.4: Typical compaction curves, (a) densification curve, (b) semi-logarithmic densification curve, (c) shear resistance curve.

Fig. 4.4(a) shows the densification process that takes place during compaction. In order

to emphasize the role of the jamming process, the volume fraction of aggregate ϕ is chosen as the y-axis, instead of the commonly used % G_{mm} (percentage of the theoretical maximum specific gravity).

Fig. 4.4(c) shows the change of shear resistance with number of gyration. The shear resistance of the mixture is evaluated by the tilting moment, measured during gyratory compaction using the Gyratory Load Plate Assembly (GLPA) of the Pine G2 gyratory compactor. The GLPA has three load cells from which the eccentric moment of the static pressure on the upper loading plate can be measured. This eccentric moment is called the tilting moment [35]. The tilting moment measures the moment needed for shearing the mixture to a fixed angle, the angle of gyration. Therefore, the tilting moment can serve as a good representation of the shear resistance of mixtures.

As shown in Fig. 4.4(c), the shear resistance reaches its maximum at a certain number of gyration, then starts to decrease. This phenomenon of the maximum shear resistance was first studied by Guler et al. [35] and was considered as an indication of unstable mixtures. In a later study, Shamsi and Mohammad [36] showed that the number of gyration at which the shear resistance was maximum had a high correlation with the traditional locking point, which implies that a certain degree of locking may have already formed. However, no explanation was given for why there is a maximum shear resistance as the density increases.

This phenomenon can be explained by the proposed physical mechanisms. The increase in the shear resistance at the beginning of compaction is a result of the aggregate jamming, in which the shear resistance increases with an increasing volume fraction of aggregates ϕ, as shown in Fig. 4.2(a). The decrease in the shear resistance in the later part of compaction is a result of aggregate binder interaction. As ϕ increase, at a certain point, the increase in pore pressure of binder will cause the reduction of the effective stress p_{eff} in aggregates and therefore reduces the shear resistance of mixture.

Fig. 4.4(b) presents the same data as Fig. 4.4(a) but in the semi-logarithmic scale. As shown, N and ϕ exhibit an approximately linear relationship in the semi-logarithmic scale plot, which confirms the results of Moutier [14].

Based on this interpretation of gyratory compaction curves, the following indices are proposed to evaluate the compactability of mixtures:

1. N_{mm}: the number of gyrations, corresponding to the maximum tilting moment.

2. M_{max}: the maximum tilting moment, corresponding to the maximum shear resistance.

3. $\phi@N_{mm}$: packing fraction at N_{mm}.

4. S_p: the slope of the linear least squares regression of ϕ versus N, for $N > N_{mm}$ which characterizes the rate of evolution of jammed states after N_{mm} is reached.

5. S_m: the slope of the linear least squares regression of the tilting moment versus N, for $N > N_{mm}$ which characterizes the rate of evolution of shear resistance after N_{mm} is reached.

6. S_{log}: the slope of the linear least squares regression of ϕ versus $\log N$, which characterizes the rate of densification.

These proposed indices provide a more detailed characterization of the compaction process, including the characterization of both the densification process and the change of shear resistance. Since the proposed indices are anchored by physical mechanisms, they are expected to exhibit better correlations with material compositions. It is important to note that the proposed indices cannot be obtained for dry aggregate systems, for which a critical gyratory number N_{mm} does not exists.

4.4 Material Composition of MnROAD Asphalt Mixtures

A statistical analysis is performed next to investigate how the material composition of the asphalt mixture, such as binder content and aggregate gradation, relate to the proposed compactability indices.

4.4.1 Material Information

Seven asphalt mixtures, used in the construction of test sections at MnROAD in 2016, were selected for the analysis. Detailed information is shown in Table 4.1. The composition is presented in terms of weight percentages. RAP_AC denotes the asphalt binder contribution from recycled asphalt pavements (RAP), and RAS_AC denotes the asphalt binder contribution from recycled asphalt shingles (RAS). RAC represents the total Reclaimed Asphalt Binder Content, which includes both RAP and RAS. No rejuvenators were used in these mixtures.

The aggregates used to make the seven mixtures come from similar sources, and therefore, they have similar properties. The coarse aggregate angularity is 98 (percentage of at least

Table 4.1: Mixture information

Mixture ID	Mix 1	Mix 2	Mix 3	Mix 4	Mix 5	Mix 6	Mix 7
Cell Number	Cell 16	Cell 17	Cell 18	Cell 19	Cell 20	Cell 21	Cell 23
Binder PG	64S-22	64S-22	64S-22	64S-22	52S-34	58H-34	64E-34
% RAP	20	10	20	20	30	20	15
% RAS	5	5	0	0	0	0	0
% RAP_AC	1.23	0.62	1.23	1.23	1.85	1.23	0.92
% RAS_AC	0.87	0.87	0	0	0	0	0
% RAC	2.1	1.49	1.23	1.23	1.85	1.23	0.92
% Total AC	5.27	5.43	5.43	5.7	5.32	5.38	5.23

two fractured faces). The fine aggregate angularity is 47 (fine aggregate packing fraction). The percentage of flat and elongated particles (dimensional ratio larger than 5:1) is 3%. The only difference in aggregate properties for these mixtures is the aggregate gradation.

4.4.2 Aggregate Gradation Analysis

The gradations of the aggregates are listed in Table 4.2. The mixtures share the same nominal maximum aggregate size (NMAS), which is 12.5 mm.

Table 4.2: Aggregate gradation of mixtures

	Percent passing, %						
Sieve size, mm	Mix 1	Mix 2	Mix 3	Mix 4	Mix 5	Mix 6	Mix 7
19	100	100	100	100	100	100	100
12.5	93.9	93.1	93.7	93.7	93.3	93.7	93.1
9.5	83.1	81.1	82.7	82.7	81.4	82.7	81
6.25	68	65.2	67.4	68.3	66	67.4	64.3
4.75	61	57.9	60.4	61.6	58.9	60.4	56.6
2.36	45.5	42.2	43.5	45.3	43.7	43.5	39.8
1.18	32.5	29.9	30.8	31.5	31	30.8	28.1
0.6	22	20.3	21	20.7	20.7	21	19.3
0.3	13.3	12.7	12.8	11.8	11.9	12.3	12
0.15	8	7.8	7.6	6.5	6.7	7.6	7.3
0.075	5.3	5.2	5	4.1	4.3	5	4.9

The Bailey method and distance from the maximum density line are used to characterize aggregates gradation. The Bailey method is an empirical method for selecting and adjusting aggregate gradation in mixture design [20]. Studies have shown that the Bailey method

parameters are strongly correlated with the compactability of mixtures [21, 83].

In the Bailey method, three critical sieve sizes are defined. The first is the Primary Control Sieve (PCS), which separates the coarse and fine aggregates. The PCS is defined as the closest sieve to 0.22×NMAS. Similarly, the Secondary Control Sieve (SCS) is defined as the closest sieve to 0.22×PCS, and the Tertiary Control Sieve (TCS) is defined as the closest sieve to 0.22×SCS.

The passing percentage of PCS (%PCS) shows the overall fineness of the blend. The larger the %PCS, the finer the blend.

Three ratios of passing percentage are defined to characterize the gradation at different scales. Coarse Aggregate ratio (CA) is defined as Eq. 4.3, to characterize the gradation of coarse aggregates. Similarly, Fine Aggregate Coarse ratio (FA_c) and Fine Aggregate fine ratio (FA_f) are defined as Eq. 4.4 and 4.5, to characterize the gradation of the coarse portion and fine portion fine aggregates, respectively.

$$\mathrm{CA} = \frac{\%\text{Half Sieve} - \%\text{PCS}}{100\% - \%\text{Half Sieve}} \tag{4.3}$$

$$\mathrm{FA_c} = \frac{\%\text{SCS}}{\%\text{PCS}} \tag{4.4}$$

$$\mathrm{FA_f} = \frac{\%\text{TCS}}{\%\text{SCS}} \tag{4.5}$$

where "%" before the critical sieve sizes meaning the passing percentage of the corresponding sieve. As the CA, FA_c, or FA_f increases, the corresponding portion of the aggregates becomes finer.

Compactability of mixtures is also related to how close the gradation curve is to the maximum density line (MDL) [40, 19]. The MDL is defined as a power-law gradation curve, i.e., %Pass of sieve size $D_i = 100 \times (D_i/D_{max})^n$, where D_{max} is the maximum aggregate size and n=0.45 [84, 85]. The MDL on the 0.45 power gradation chart is represented by a straight diagonal line [86]. Therefore, we define another parameter called the distance to MDL (d_{MDL}), which is calculated as the sum of the absolute difference between the gradation curve and MDL at each sieve size:

$$\mathrm{d_{MDL}} = \sum_{i=1}^{\text{number of sieves}} \left| \%\text{Pass of sieve i} - 100 \times (\frac{D_i}{D_{max}})^n \right| \tag{4.6}$$

The calculated Bailey method parameters and d_{MDL} for the seven mixtures are summarized in Table 4.3.

It is important to note that the seven mixtures studied are fine-graded, and the critical sieve sizes had to be adjusted [20]. All critical sieve sizes are scaled down by a factor of 0.22. FA_f cannot be calculated since, after the adjustment, the new TCS becomes too small (less than 0.075mm).

Table 4.3: Parameters to characterize gradation

Mixture ID	Mix 1	Mix 2	Mix 3	Mix 4	Mix 5	Mix 6	Mix 7
% PCS	48.4	48.1	48.3	45.7	47.4	48.3	48.5
CA Ratio	0.808	0.78	0.772	0.783	0.811	0.772	0.752
FA_c Ratio	0.364	0.384	0.362	0.314	0.324	0.362	0.378
d_{MDL}	55.3	41.6	50.3	58.2	48.9	50.8	38.7

4.5 Compactability Evaluation of MnROAD Mixtures

Gyratory compaction tests of the seven mixtures were conducted during the mix design phase, according to AASHTO T312 (2019). The compaction temperature was determined based on the equiviscous principle [44], and varied with the asphalt binder PG. For the seven mixtures studied, the compaction temperature ranged from 123 to 143°C. The external pressure P is 600 kPa, the gyration angle α is 1.16 °, and the rate of gyration ω is 30 gyrations per minute. Specimen diameter was 150 mm and the height was 115 ± 5 mm after compaction. For each mixture, gyratory compactions were conducted at three levels of total asphalt binder content, 5.0%, 5.5%, and 6.0% (for Mix 3 only, the total binder content was 4.8%, 5.3%, and 5.8%, respectively). For each level of total asphalt binder content, two or three replicates were compacted, for a total of 48 gyratory compaction tests. An example of compaction curves for Mix 1 is shown in Fig. 4.5. The points corresponding to N_{mm} are identified by circles.

As seen in Fig. 4.5(a), the replicates with higher total binder content are more compactable, since at a same gyration number, they have a higher packing fraction of aggregates. As seen in Fig. 4.5(b), the mixtures with the highest total binder content (6%) have a higher decreasing rate of tilting moment (S_m) after reaching N_{mm}. The compaction curves of all other mixtures exhibit similar trends, and are not shown. Based on the compaction curves,

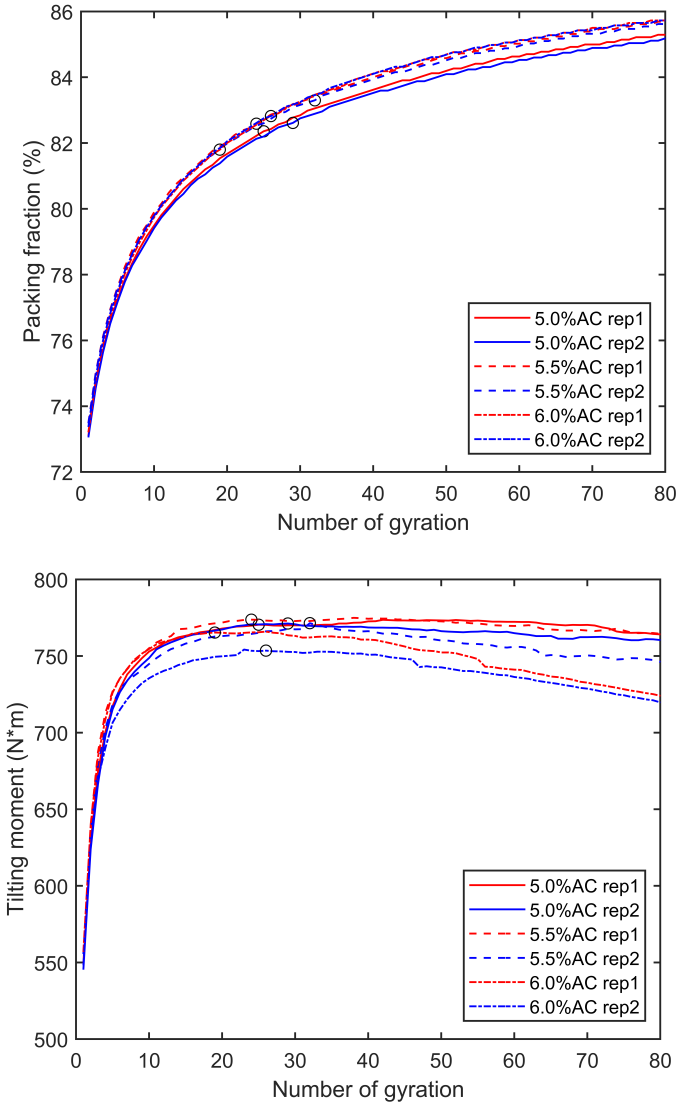

Figure 4.5: The compaction curves of Mix 1. (a): the densification curve; (b): the shear resistance curve. Note: the circles identifies N_{mm}, when shear resistance is maximum

the physical indices are computed and listed in Table 4.4.

Table 4.4: Compactability indices of different mixtures

	AC, [%]	N_{mm}	$\phi@N_{mm}$, [%]	M_{max}, $[N \cdot m]$	S_p	S_m	S_{log}
Mix 1	5	27	82.48	770.8	0.0519	-0.163	7.376
	5.5	28	82.94	772.6	0.0518	-0.345	7.493
	6	22.5	82.31	759.4	0.0591	-0.651	7.837
Mix 2	5	26.5	81.79	759.6	0.0569	-0.322	7.819
	5.5	18.7	80.96	768.1	0.0665	-0.326	7.683
	6	24.3	81.91	776.9	0.0601	-0.522	8.108
Mix 3	4.8	20.5	80.42	738.5	0.0611	-0.133	7.206
	5.3	22	81.76	768.8	0.0598	-0.32	7.507
	5.8	14	80.26	767.7	0.0788	-0.328	8.003
Mix 4	5	22	81.07	802.5	0.0468	-0.304	6.909
	5.5	19.5	80.62	824.6	0.0542	-0.488	7.27
	6	22	81.68	858.6	0.0505	-0.609	7.522
Mix 5	5	37.3	83.08	800.9	0.0441	-0.203	7.091
	5.5	11	79.98	858.1	0.0804	-0.24	7.495
	6	16	81.37	860.6	0.0673	-1.206	7.468
Mix 6	5	37.3	82.81	770.5	0.0485	-0.093	7.697
	5.5	29.5	82.57	772.7	0.0564	-0.189	7.953
	6	23.7	82.06	767.5	0.0629	-0.419	8.194
Mix 7	5	22	81.73	747.4	0.0628	-0.149	7.864
	5.5	25	82.35	738.9	0.0604	-0.368	8.128
	6	18	81.05	735.1	0.0712	-0.667	8.379

4.6 Correlations between Mixture Properties and Compactability Indices

A statistical analysis is conducted to identify correlations between mixtures' material properties and the proposed compactability indices. The investigated material properties include:

1. total binder content (%AC),
2. reclaimed binder content (%RAC),
3. Bailey method parameters (%PCS, CA, and FA_c), and
4. distance to the maximum density line (d_{MDL}).

Although the viscosity of binder has a profound influence on the compaction process, it is not investigated in this study since the gyratory compaction tests are conducted at

temperatures at which the binders have similar viscosities [44]. Meanwhile, shape and angularity of aggregates are also not considered in this study since similar aggregate sources were used to prepare the mixtures. The focus of this study is on the effects of asphalt binder content and aggregate gradation on compaction.

First, a correlation analysis is conducted to identify high correlation pairs. Then, multiple linear regression models for each compactability index are obtained using the best subset regression method.

4.6.1 Correlation Analysis

Scatter plots of mixtures' material properties (horizontal axis) versus the compactability indices (vertical axis) are shown in Fig. 4.6. The data is divided into three groups according to the total binder content.

In the correlation analysis, the Pearson correlation coefficients, r, and p-value are computed. The p-value is used for the hypothesis test which checks the statistical significance of the linear correlation. The null hypothesis is "the correlation coefficient is not significantly different from 0". If the p-value is less than the significance level (0.05), we can reject the null hypothesis, and conclude the linear correlation is statistically significant. Otherwise, we accept the null hypothesis. The calculated r and p-value are listed in Table 4.5. Pairs that passed the hypothesis test (p-value < 0.05) are identified in bold in Table 4.5.

For each of the correlated pairs, we examine whether the correlation can be explained by the proposed physical mechanisms. It is observed that the total binder content (%AC) has the most significant effect on compactability; it is correlated with most compactability indices, including N_{mm}, S_p, S_m, and S_{log}. The negative correlations of %AC with N_{mm} and S_m is reasonable from the viewpoint of binder-aggregate interaction. It is easier for mixtures to develop pore pressure when the binder content is higher, which causes a fewer number of gyration (N_{mm}) before reaching the peak shear resistance, and a faster dropping rate (S_m) of shear resistance when $N > N_{mm}$.

The positive correlations of %AC with S_p and S_{log} indicate that the increase of total binder content accelerates the densification process. These can also be explained using the proposed mechanisms; asphalt binder acts as the interstitial fluid that provides the lubrication between aggregates, and makes it easier for the jammed state to unjam by shear, and increases the rate of evolving from one jammed state to another.

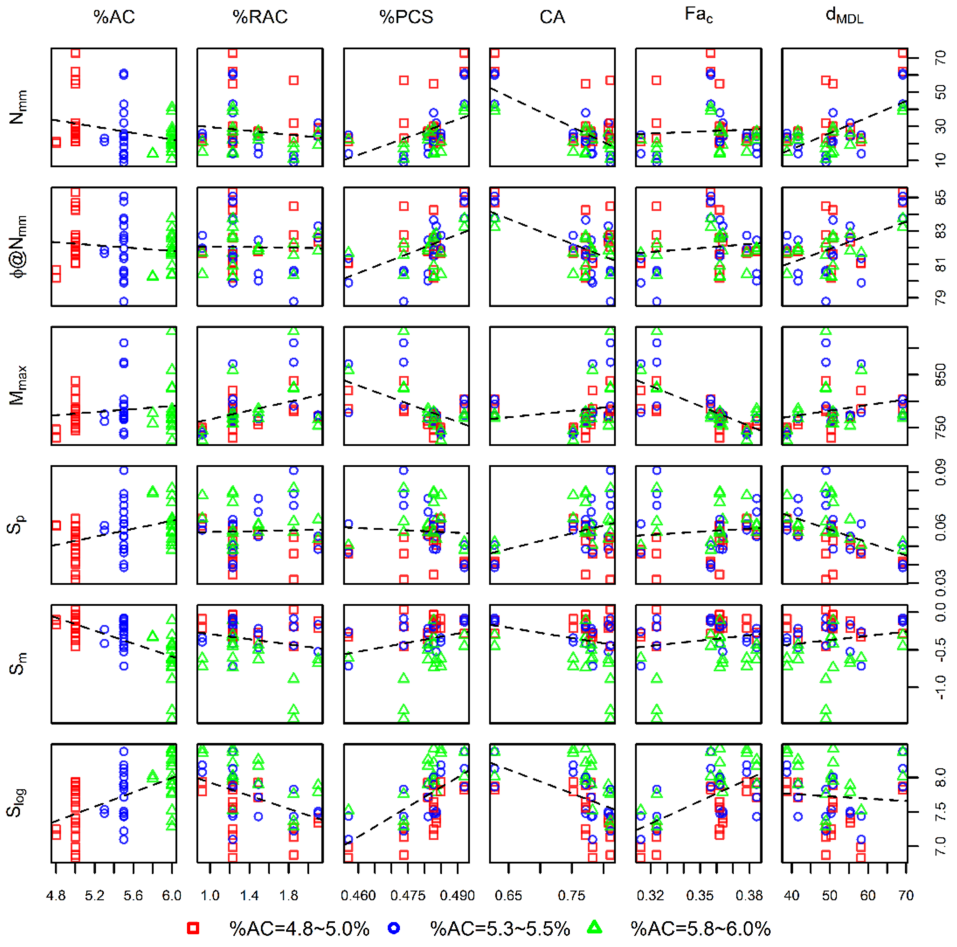

Figure 4.6: Scatter plots between mixture properties and compactability indices

The reclaimed binder content (%RAC) has a positive correlation with M_{max} and a negative correlation with S_{log}, which indicates that %RAC has an adverse effect on compaction, because it tends to increase shear resistance and decrease densification rate. These correlations are reasonable because, compared to virgin binder, reclaimed binder has higher viscosity and less lubricated which have adverse impacts on compaction.

The Bailey parameters are correlated with M_{max} and S_{log}. The results of %PCS shows that the increase in the proportion of fine aggregates (the increase in %PCS) decreases the maximum shear resistance (M_{max}), and increases the overall densification rate (S_{log}). The result shows that the increase in the fineness of the coarse portion of aggregates (the increase in the CA) leads to an increase in the maximum shear resistance (M_{max}), and a

Table 4.5: Results of pairwise correlation analysis.

	%AC	%RAC	%PCS	CA	FA_c	d_{MDL}
N_{mm}	**p=0.01** **r=-0.35**	p=0.85 r=0.03	p=0.39 r=0.13	p=0.94 r=-0.01	p=0.54 r=0.09	p=0.63 r=0.07
$\phi@N_{mm}$	p=0.39 r=-0.13	p=0.29 r=0.16	p=0.09 r=0.25	p=0.66 r=0.07	p=0.27 r=0.16	p=0.75 r=0.05
M_{max}	p=0.23 r=0.18	**p=0.01** **r=0.37**	**p<0.01** **r=-0.60**	**p<0.01** **r=0.57**	**p<0.01** **r=-0.71**	**p=0.02** **r=0.34**
S_p	**p<0.01** **r=0.41**	p=0.65 r=-0.07	p=0.16 r=0.20	p=0.60 r=-0.08	p=0.41 r=0.12	**p=0.03** **r=-0.32**
S_m	**p<0.01** **r=-0.65**	p=0.23 r=-0.18	p=0.23 r=0.18	p=0.13 r=-0.22	p=0.19 r=0.19	p=0.87 r=0.02
S_{log}	**p<0.01** **r=0.55**	**p=0.01** **r=-0.38**	**p<0.01** **r=0.59**	**p<0.01** **r=-0.54**	**p<0.01** **r=0.66**	**p<0.01** **r=-0.54**

Note: The boldfaced cells have p-value<0.05, which indicates the linear correlation is statistically significant.

decrease in the overall densification rate (S_{log}). The results of FA_c indicate that the increase in the fineness of the fine portion of aggregates (the increase in FA_c) causes a decrease in the maximum shear resistance (M_{max}), and an increase in the overall densification rate (S_{log}). The results of %PCS and FA_c are consistent with practical experiences that the compactability of mixtures increase with the increase in the fineness of aggregates. However, the results of CA suggest that the coarseness of the coarse portion of aggregates would improve the compactability.

The distance to the maximum density linear, d_{MDL}, is correlated to M_{max} , S_{log}, and S_p. A reduction in d_{MDL} helps compaction, since it decreases the maximum shear resistance (M_{max}), and increase the rate of densification (S_{log}, and S_p).

The identified correlations between compactability and aggregate gradation, including the Bailey parameters and d_{MDL}, can be reasonably explained by the physical mechanism of jamming. It is clear that different gradation will lead to different critical volume fraction ϕ_J and maximum dense packing fraction ϕ_m of jamming. Higher ϕ_J and ϕ_m are corresponding to higher compactability of mixtures. However, how exactly ϕ_J and ϕ_m are affected by gradation is not clear. Therefore, more research is needed to reveal this relationship.

4.6.2 Multiple Linear Regression

Multiple linear regression models are used to quantify the effect of each material property on the compactability indices, and to consider the joint effect between different material properties.

As shown in the correlation analysis, for a compactability index, not all material properties have significant correlation with it. Therefore, including all the six material properties as predictors will over fit the compactability index. A predictor selection process is conducted to identify the best subset of all material properties.

The best subset selection method [87] is adopted to perform a predictor selection. In this study, there are 6 material properties, so the subset can have a size ranges from 1 to 6. For a certain size k, the best subset selection method finds the subset of k predictors that produces the best fit in terms of the coefficient of determination, R^2. The best subsets of different k are then compared by the adjusted R^2. The subset that produces the highest adjusted R^2 is chosen as the final best subset. The adjusted R^2 compares the explanatory power of regression models that contain different numbers of predictors. It is a modified version of R^2 that has been adjusted for the number of predictors in the model [88].

Table 4.6 exemplifies the best subset selection process for S_{log}. For each subset size, the best subset is identified and marked in Table 4.6. Among different sizes of subset, it is found that when size = 4, adjusted R^2 gets its maximum (0.773). Therefore, the corresponding subset, containing 4 predictors (%AC, %PCS, CA, and d_{MDL}), is identified as best subset for the multiple linear regression model of S_{log}.

Table 4.6: Best subset regression for S_{log}

Size of subset	%AC	%RAC	%PCS	CA	FA_c	d_{MDL}	Adj. R^2
1					✓		0.423
2	✓				✓		0.688
3	✓		✓	✓			0.771
4	✓		✓	✓		✓	**0.773**
5	✓		✓	✓	✓	✓	0.771
6	✓	✓	✓	✓	✓	✓	0.766

Note: The highest adjusted R2 is boldfaced.

The same approach is applied for the other compactability indices, and the best linear regression models of each compactability index are summarized in Table 4.7.

Table 4.7: Results of multiple linear regressions

Compactability indices	Best subset regression model	Adj.R^2	R^2
N_{mm}	$N_{mm} = 65.4 - 7.7 \times \%\text{AC}$	0.104	0.123
$\phi@N_{mm}$	$\phi@N_{mm} = 65.3 + 34.2 \times \%\text{PCS}$	0.041	0.062
M_{max}	$M_{max} = 800.7 + 666.7 \times \text{CA} - 1264.1 \times \text{FA}_\text{c} - 1.86 \times \text{d}_\text{MDL}$	0.616	0.64
S_p	$S_p = 0.0276 + 0.0107 \times \%\text{AC} - 0.000538 \times \text{d}_\text{MDL}$	0.212	0.245
S_m	$S_m = 2.153 - 0.464 \times \%\text{AC}$	0.41	0.422
S_{log}	$S_{log} = 2.23 + 0.524 \times \%\text{AC} + 19.0 \times \%\text{PCS} - 7.89 \times \text{CA} - 0.00723 \times \text{d}_\text{MDL}$	0.773	0.793

R^2 is a goodness-of-fit measure of the regression model. As shown in Table 4.7, the values of R^2 of the regression models are relatively low (less than 0.8). This is expected given the intrinsic randomness of asphalt mixture as a heterogeneous material. Other factors, such as shape and texture of aggregate particles, which were not captured in this study, influence this randomness. Also, the regression models only considered the linear case while higher orders (nonlinear) correlations were ignored, which could be another reason for the low value of R^2.

As shown in Table 4.7, the regression models for Mmax and Slog have reasonable R^2s (0.640 and 0.793 respectively), considering the intrinsic randomness. These models quantified the effect of material properties on compactability, thus will be helpful for mixture design. The compactability of mixtures can be controlled in design phase by determine the criteria for Mmax and Slog. Then, these formulas can help determine or adjust the material properties.

For the regression models of other compactability indices, the R^2s are too low (less than 0.422). It implies that the six material properties selected are not capable to fully explain these compactability indices. To improve the performance of these models, more material properties need to be further considered, e.g., the shape and angularity of aggregate, and the rheology of binder and fine aggregate matrix (FAM).

4.7 Conclusions

In this paper, two physical mechanisms, jamming of aggregates and aggregate binder interaction, are proposed to explain the compaction process of asphalt mixture. Based on these mechanisms, six compactability indices characterizing gyratory compaction data are developed and used to evaluate the compactability of seven mixtures from MnROAD. Correlations between compactability and material properties, such as binder content and gradation, were analysed. The following conclusions were drawn from this study.

- Using the physical mechanism of aggregates jamming, compaction process of asphalt mixture can be interpreted as the evolving jammed states of aggregates under the excitation of shear or vibration. This interpretation explains why shear and vibration enhance densification, and why shear resistance increases with density, showing the coupling effects between shear and densification process of asphalt mixture.

- The physical mechanism of binder-aggregate interaction explains the decrease in shear resistance in the latter part of gyratory compaction.

- The statistical analysis identified several correlations between the compactability indices and the material properties. The identified correlations can be well explained by the physical mechanisms, which, offers support to the validity of the proposed mechanisms.

- The identified correlations between the compactability indices and aggregate gradation were not fully understood. The correlations can be attributed to the effects of aggregate gradation on the critical volume fractions of the aggregate jamming, ϕ_J and ϕ_m. However, further research is needed to better understand how ϕ_J and ϕ_m are affected by aggregate gradation.

- The identified correlations between the compactability indices and aggregate gradation were not fully understood. The correlations can be attributed to the effects of aggregate gradation on the critical volume fractions of the aggregate jamming, ϕ_J and ϕ_m. However, further research is needed to better understand how ϕ_J and ϕ_m are affected by aggregate gradation.

- Multiple linear regression models for each compactability indices were developed using

material properties. Potentially, the models can be used in mixture design to control the compactability of mixtures.

Due to the limited number of mixtures studied, the multiple linear regression models developed may not be applicable for all mixtures. A larger set of mixtures needs to be further studied to consider a wider range of material properties in the regression models, such as aggregate shape, angularity, and binder rheology. This study provides a general approach to evaluate the compactability of mixtures and design denser mixtures that can significantly improve the durability of asphalt pavements.

Chapter 5

One-Dimensional Nonlocal Model for Gyratory Compaction of Hot Asphalt Mixtures[1]

Gyratory compaction has widely been used to evaluate the compactability of hot asphalt mixture. Existing efforts on modeling of gyratory compaction have largely been devoted to sophisticated high-fidelity computational models. This paper presents a simple one-dimensional nonlocal model for gyratory compaction. The model is anchored by the principle of mass conversation, in which the local densification rate is formulated as a function of nonlocal packing fraction. The nonlocal model involves a material characteristic length scale, which is independent of the specimen size. The nonlocality gives rise to strong effects of specimen height on the overall compaction curve as well as on the profile of the local packing fraction. A set of gyratory compaction experiments is performed on specimens of different heights. It is shown that the model is able to capture the measured size effect on the compaction curves. A parametric study is performed to investigate the effects of nonlocality and model parameters on the predictions of compaction curve and profile of packing fraction.

[1]This chapter is adopted from the following manuscript:
T. Yan, M. Marasteanu, and J.-L. Le. One-dimensional nonlocal model for gyratory compaction of hot asphalt mixtures. *J. Eng. Mech.*, under review

5.1 Introduction

Compaction of asphalt mixture is an essential step of the construction of asphalt pavements. During the compaction, asphalt binder, aggregates, and fines are subjected to a combination of compressive and shear forces as well as external vibration. The compaction process directly determines the final air void ratio of the asphalt mixtures, and therefore has a significant consequence for the durability and resilience of asphalt pavements [74, 5, 6, 7, 8, 37]. A high air void ratio will lead to a low material strength [90], and at the same time also an increased moisture susceptibility [91]. On the other hand, an over-compacted mixture would be sensitive to high temperature [92]. Therefore, understanding the compaction process is of critical importance for design of asphalt pavements.

Over the past decades, extensive efforts have been devoted towards experimental investigation of compaction of asphalt mixtures in a laboratory setting. Many different laboratory compaction testing methods, such as Marshall impact compaction, kneading compaction, and gyratory compaction, have been developed [93, 94]. Among these methods, the gyratory compaction is considered as one of the best approaches to simulate the field compaction process [94]. It was adopted as the laboratory compaction method for the current asphalt mixture design method in the United States (i.e. Superpave mixture design method) [95]. Experimental investigation of gyratory compaction led to the development of different compaction indices, e.g., compaction slope [14, 21], locking point [15, 21], and energy indices [16, 96]. Based on these indices, different correlations between material properties and compactability were established. For example, it was observed that mixtures with more angular aggregates or less binder content are more difficult to compact [16, 18, 21].

With the advances in computational tools, major research efforts have been directed towards numerical modeling of the compaction process of asphalt mixtures. The existing computational models can be divided into two categories, namely the continuum and discrete modeling approaches. The continuum approach is anchored by material constitutive models. In some early attempts the critical state model of soil mechanics was adopted for finite element simulations of the compaction of asphalt mixtures [97]. Recent studies extended finite-strain elasto-viscoplasticity models to compaction of asphalt mixtures [23, 24, 25, 22]. The continuum models have been successfully used to simulate both the gyratory compaction and the field compaction of asphalt mixtures. These models are computationally efficient for large-scale simulations. However, due to the nature of continuum modeling, the models do

not capture the effect of mesoscale features, such as aggregate shape and size distribution, on the compactability of asphalt mixtures.

In the discrete approach, the asphalt mixture is modeled as an assembly of particles (aggregates), and some specific contact model is used to describe the particle interaction. The main advantage of discrete approach is that it explicitly captures the shape and size distribution of aggregates, which are believed to have a significant influence on the compaction performance. Chen et al. [27, 98] used the discrete element method to simulate different laboratory compaction experiments including gyratory compaction, vibration, and kneading. In the simulation, a visco-elastic-plastic contact law was used to describe the aggregate interaction. In recent studies, more realistic shapes of aggregates (e.g. elongated and flat aggregates), obtained from X-ray scan, were considered in the discrete modeling [99, 28, 29, 100]. The model was used to investigate the shape effect of coarse aggregates on the compaction. Man [30] recently developed a more realistic discrete element model for compaction of hot asphalt mixtures, in which the composite particle model was used to simulate the non-spherical aggregates. The inter-particle contact law considered both the Hertizian-Mindlin contact between coarse aggregates and the lubrication action of the viscous asphalt binder and fine aggregates. By capturing the motion of each aggregate, the discrete modeling approach provides more insights into the mechanism of compaction process. However, the main drawback is the excessive computational cost, which makes it prohibitive for application to large-scale simulations.

In contrast to computational modeling, very limited efforts have been devoted to analytical modeling of asphalt compaction. Analytical modeling is advantageous in terms of computational efficiency. Meanwhile, it also provides an effective means for investigating the relations between the material properties and the overall compactability of asphalt mixtures. In this study, we develop a one-dimensional (1D) nonlocal continuum model for gyratory compaction, based on the mesoscopic mechanism of granular compaction. The proposed model is calibrated and validated by a set of gyratory compaction tests.

5.2 Model Description

In the gyratory compaction, the loose mixture is contained in a rigid cylindrical mold. The top plate gyrates horizontally around the central axis at a constant angular velocity ω. The bottom plate is pushed vertically up under constant pressure P. The mixture is

compacted to a dense state under the combined compression and shear loading. As shown in Fig.5.1a, the compaction deformation occurs in the vertical direction, although there is shear deformation in the horizontal plane. Therefore, we may model the compaction process by using a one-dimensional model, in which each material point represents a cross-section of the specimen as shown in Fig.5.1b.

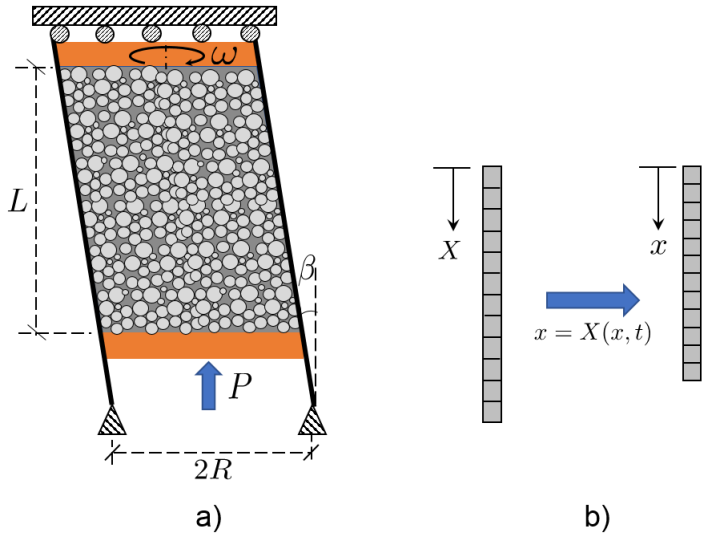

Figure 5.1: Schematics of gyratory compaction of asphalt mixtures: a) test set-up, and b) one-dimensional model.

5.2.1 Mass Balance Equation

Let $x(X,t)$ denote the position of material point X in the reference configuration at time t, and $\rho(x,t)$ be the average density of the material of a cross-section at location x and time t. The local form of mass conservation can then be written as [101, 102]

$$\frac{\mathrm{d}}{\mathrm{d}t}\left\{\rho[x(X,t),t]\frac{\partial x(X,t)}{\partial X}\right\}=0 \tag{5.1}$$

We define packing fraction ϕ as the volume ratio of aggregates and binder to the bulk volume of the mixture, and the air void ratio can be calculated by $1-\phi$. By this definition, ϕ can be computed as ρ/ρ_m, where ρ_m denotes the maximum possible density of the mixture, which corresponds to the case of a zero air-void ratio. It is clear that Eq. 5.1 can be rewritten

in terms of the packing fraction, i.e.

$$\frac{\mathrm{d}}{\mathrm{d}t}\left\{\phi[x(X,t),t]\frac{\partial x(X,t)}{\partial X}\right\}=0 \tag{5.2}$$

It is reasonable to consider that, for gyratory compaction, the initial packing fraction of the mixture is uniform since the effect of gravity is minimal, i.e. $\phi(X,0)=\phi_0$. With this initial condition, Eq. 5.2 yields

$$\phi[x(X,t),t]\frac{\partial x(X,t)}{\partial X}=\phi_0 \tag{5.3}$$

Eq. 5.3 relates the current configuration of the specimen to the local packing fraction based on mass conservation. It is clear that, to solve the problem, we need the second equation that relates the packing fraction to the deformation state. The role of this relationship in the present analysis is analogous to that of material constitutive model in stress analysis. Clearly, the relation between the packing fraction and deformation state must be tied with the mechanism of the compaction process.

In this study, we propose a model for the material point velocity $v(x,t)$. The rationale for investigating the material point velocity is that the compaction of asphalt mixture is driven by the rearrangement of aggregates in the medium of viscous binder. The aggregate rearrangement can be regarded as a process of transitions between different packing states [73]. During the compaction, the external excitation (gyratory motion and compression) supplies the energy to the system for aggregate rearrangement and transition from a loose packing state to a denser one. Therefore, the material point velocity $v(x,t)$ must be related to the rate of the transition between different packing states.

5.2.2 Nonlocal Densification Model

Here we consider a cluster of aggregates, which has a length of l_0 and a cross section same as the gyratory compaction specimen (Fig. 5.2a). As will be discussed later, l_0 represents an essential length scale of the present model. From the viewpoint of energy landscape, each packing state of the cluster (i.e. configuration of aggregate arrangement) can be considered as a metastable state. The transition between metastable energy states has been studied extensively in statistical mechanics, e.g. [103, 104, 105]. One well-known model is the transition rate theory, which leads to the Kramers equation for the escape rate of a deep energy

well [103]. The Kramers model is applied to study the general phenomena of state transition [106]. In the model, the frequency of the transition between two adjacent metastable states can be described by

$$f = f_0 \exp(-U_a/E_s) \tag{5.4}$$

where f_0 = reference frequency, U_a = energy barrier across two adjacent states, and E_s = intrinsic energy of the system, which is referred to as the system energy that can activate the transition between adjacent states. For instance, when applying Eq. 5.4 to thermally activated process of nanoscale structures, one can consider E_s = thermal energy ($E_s = k_b T$, k_b = Boltzmann constant and T = absolute temperature), and U_a as the activation barrier.

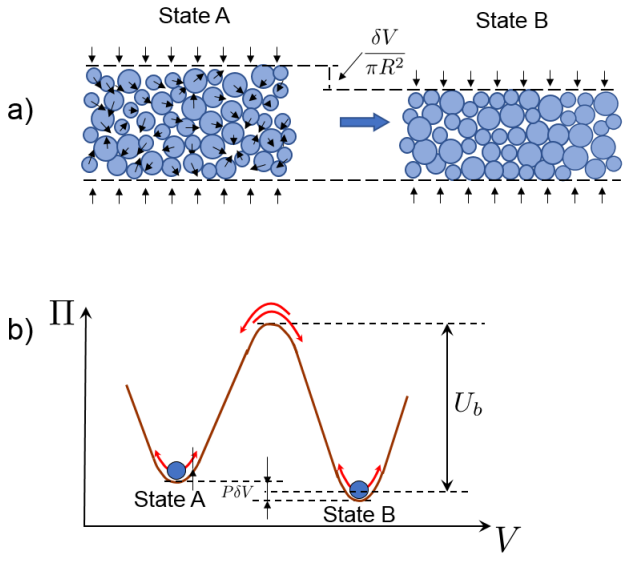

Figure 5.2: Aggregate rearrangement in a cluster: a) schematics, and b) energy landscape.

We apply Eq. 5.4 to the transition between different packing states during gyratory compaction. The aggregate rearrangement is driven by mechanical loading, which is not a thermally activated process. Here we consider that the intrinsic energy of the cluster of aggregates is related to the gyratory motion, which induces shearing of the loose asphalt mixture. As an analogy to the thermal energy for thermally activated process, we consider E_s to be associated with the kinetic energy of the aggregates induced by the shearing motion, which can be expressed by

$$E_s = C\rho_a V_a \dot{\gamma}^2 d_a^2 \tag{5.5}$$

where C = constant, ρ_a = aggregate density, $\dot{\gamma}$ = shear rate induced by the gyration, d_a = average aggregate diameter, and V_a = volume of the aggregates in the cluster.

Consider the transition between two adjacent packing states. The absolute volume difference of these two states is denoted by δV. This volume change is driven by the movement of the bottom plate. Therefore, the energy input by the vertical pressure is given by $P\delta V$. This energy input creates a bias of the energy landscape of the packing states. As shown in Fig. 5.2b, the energy barrier for transitioning from a loose state to a dense state is lower than that for transitioning from a dense state to a loose state. The net frequency of the transition can be written as

$$f_V = f_V^+ - f_V^- = f_0 \left[\exp\left(-\frac{U_b - P\delta V/2}{E_s} \right) - \exp\left(-\frac{U_b + P\delta V/2}{E_s} \right) \right] \tag{5.6}$$

$$= 2 f_0 e^{-U_b/E_s} \sinh\left(\frac{P\delta V}{2E_s} \right) \tag{5.7}$$

where f_V^+ = frequency of transition from a loose state to a dense state, f_V^- = frequency of transition from a dense state to loose state, and U_b = free energy barrier in absence of pressure P. Since the compaction is a continuous process consisting transitions between numerous packing states, we may consider $P\delta V \ll E_s$, and rewrite Eq. 5.7 as

$$f_V = f_0 e^{-U_b/E_s} \frac{P\delta V}{E_s} \tag{5.8}$$

Consequently, the volumetric strain rate can then be expressed as

$$\dot{\epsilon}_V = -f_V \delta V / V_0 = -f_0 \epsilon_0^2 e^{-U_b/E_s} \frac{P V_0}{E_s} \tag{5.9}$$

where $\epsilon_0 = -\delta V/V_0$ = volumetric strain induced by one state transition (the minus sign indicates that the cluster volume decreases during the transition).

The energy barrier U_b is related to the packing fraction ϕ. It is expected that the rearrangement of aggregates is easier when aggregates are loosely packed (e.g. ϕ is close to ϕ_0) and becomes increasingly difficult as ϕ increases. Therefore U_b must increase with the packing fraction. Meanwhile, it is important to note that the movement of one aggregate will cause the rearrangement of the neighborhood aggregates. This collective behavior is evidenced by the results of discrete element simulations [99, 28, 29, 100, 30].

Within the framework of continuum modeling, the interaction of the neighboring aggregates can be represented by a nonlocal model. In general there are two classes of nonlocal models, namely nonlocal integral and gradient models. In integral model, the nonlocal quantity is calculated as a weighted average of the local quantities in the neighborhood, whereas in the gradient model the nonlocal quantity is governed by a differential equation. It has been shown that in 1D the gradient model is equivalent to the integral model with a particular form of weighting function [107]. Here we adopt an implicit gradient model, in which the nonlocal packing fraction is governed by the following differential equation [107, 108, 109, 110]:

$$\bar{\phi}(x,t) - \frac{{l_a}^2}{2}\frac{\partial^2 \bar{\phi}(x,t)}{\partial x^2} = \phi(x,t) \tag{5.10}$$

where $\bar{\phi}(x,t)$ = nonlocal packing fraction of material point, $\phi(x,t)$ = local packing fraction of material point, and l_a = material characteristic length. Eq. 5.10 can be derived from the integral model by using the Taylor expansion to express the local quantities in the neighborhood [107, 109]. The material length l_a controls the size of nonlocal interaction zone. In the present model, it is natural to relate l_a to the cluster size l_0. Similar to nonlocal models for material damage [111, 112], here we consider l_a to be proportional to the mean aggregate size d_a ($l_a = \eta d_a$). Furthermore, during the gyratory compaction, the rearrangement of aggregates and consequently the proportionality constant η is affected strongly by the viscous behavior of the binder as well as the contact properties of aggregates.

It is clear that Eq. 5.10 must be supplemented by boundary conditions. For gyratory compaction, the rigid plates at two ends provide significant restraints to the motion of aggregates [113, 114, 34]. In the present model, this behavior is represented by two essential boundary conditions for Eq. 5.10, i.e.

$$\bar{\phi}(0,t) = \bar{\phi}(L,t) = 1, \text{ for } t \geq 0 \tag{5.11}$$

Based on the foregoing discussion, we propose a simple relation between the energy barrier and the nonlocal packing fraction as

$$U_b = U_0 + U_1 \langle \bar{\phi} - \phi_t \rangle^k \tag{5.12}$$

where $\langle x \rangle = \max(x, 0)$, and U_0, U_1, k, ϕ_t = constants. By substituting Eq. 5.12 into Eq. 5.9

and noting the one dimension nature of the present model, we obtain

$$\frac{\partial v(x,t)}{\partial x} = -C_1 P(x,t) \exp\left[-C_2 \langle \bar{\phi}(x,t) - \phi_t \rangle^k\right] \tag{5.13}$$

where $C_1 = f_0 \epsilon_0^2 V_0 / E_s \exp(-U_0/E_s)$ and $C_2 = U_1/E_s$. For a particular gyratory compaction operation on a given asphalt mixture, we may consider C_1, C_2, k, and ϕ_t constants. In the model, we further enforce densification rate $\partial v(x,t)/\partial x$ to be zero if the local packing fraction reaches one. This condition guarantees that the maximum packing fraction equals to one. It is interesting to note that a similar form of Eq. 5.13, but in a local framework, was used to describe the material-point velocity for modeling the density relaxation process of dry granular under tapping [115, 116, 117].

In Eq. 5.13, the local strain rate is related to the local pressure. Therefore, in principle, we would need to supplement Eq. 5.13 by an equilibrium equation. By neglecting the wall friction of the compactor and gravity, the present 1D model indicates that the pressure remain constant $P(x,t) = P$. Therefore, Eqs. 5.3 and 5.13 suffice for describing the behavior of the gyratory compaction in a simplified 1D setting.

5.2.3 Initial and Boundary Conditions and Numerical Solution

A finite difference numerical scheme is used to solve Eqs. 5.3, 5.10 and 5.13. Since the space is discretized in the reference configuration, it is more convenient to write Eqs. 5.10 and 5.13 in the reference configuration using the chain rule, i.e.:

$$\frac{\partial x(X,t)}{\partial X} = \frac{\phi_0}{\phi(X,t)} \tag{5.14}$$

$$\bar{\phi}(X,t) - \frac{{l_a}^2}{2}\left[\frac{\partial^2 \bar{\phi}(X,t)}{\partial X^2}\left(\frac{\phi(X,t)}{\phi_0}\right)^2 - \frac{\partial \bar{\phi}(X,t)}{\partial X}\left(\frac{\partial^2 x}{\partial X^2}\right)\left(\frac{\phi(X,t)}{\phi_0}\right)^3\right] = \phi(X,t) \tag{5.15}$$

$$\frac{\partial v(X,t)}{\partial X} = -\frac{C_1 P \phi_0}{\phi(X,t)} \exp\left[-C_2 \langle \bar{\phi}(X,t) - \phi_t \rangle^k\right] \tag{5.16}$$

In addition to the boundary condition of the nonlocal packing fraction (Eq. 5.11, we also impose the boundary condition for the top plate ($X = 0$), where the vertical movement of the top plate is restrained:

$$v(0,t) = v_0(t) = 0, \text{ for } t \geq 0 \tag{5.17}$$

$$x(0,t) = x_0(t) = 0, \text{ for } t \geq 0 \tag{5.18}$$

The initial condition of the system is given by $x_i(0) = X_i$.

In the numerical scheme, the reference domain Ω_0 ($X \in [0, L]$) is discretized into n equal intervals, and the nodal coordinates can be written as $X_i = i\Delta X$ ($i = 0, 1, ...n$), where ΔX = interval size. To facilitate the finite difference scheme, a pseudo node X_{-1} is added at $X = -\Delta X$. Let Δt denote the time step.

Consider we know all the nodal positions $x_i(t)$ at time t, and now try to calculate the nodal position at time step $t + \Delta t$. In the present analysis, the spatial derivatives of any variable y are evaluated by finite differences: $\partial y/\partial X|_{X_i} \approx [y_i(t) - y_{i-1}(t)]/\Delta X$, and $\partial^2 y/\partial X^2|_{X_i} \approx [y_{i+1}(t) + y_{i-1}(t) - 2y_i(t)]/\Delta X^2$, where the subscript indicates the coordinate of the grid. By substituting these finite difference approximations into Eqs. 5.14 to 5.19, we obtain

$$v_i(t + \Delta t) = \mathcal{F}_i[x_{-1}(t + \Delta t), x_0(t + \Delta t), ..., x_n(t + \Delta t)] \quad (i = 0, ..., n) \tag{5.19}$$

where function $\mathcal{F}_i$ relates nodal positions of all grids to the densification rate at grid i at time $t + \Delta t$. To ensure the stability of the solution, an implicit scheme is used to determine the new position of the node X_i, i.e. $x_i(t + \Delta t) = x_i(t) + v_i(t + \Delta t)\Delta t$. By substituting the expression of $x_i(t + \Delta t)$ into Eq. 5.19, we obtain a system of equations, from which we solve the new nodal position $x_i(t + \Delta t)$ by using the secant method.

5.3 Experimental Investigation

A set of gyratory compaction tests were conducted to calibrate and validate the model. The asphalt mixture was designed using the Superpave volumetric design method [95], with a target air-void ratio of 4% and a 20-year traffic level of 3-10 million equivalent single axle load (ESAL). The mixture has a binder content of 5.8% by weight. The performance grade of the binder is PG 58H-28 according to AASHTO M332 [118]. The theoretical maximum density of the mixture, ρ_m, is measured to be 2.495 g/cm^3 based on AASHTO T209 standard [119]. The nominal maximum aggregate size of this mixture is 9.5mm. The aggregate gradation of the mixture is listed in Table 5.1.

The salient feature of the present model is the consideration of nonlocality, which naturally involves a material length. A natural consequence is that the predicted compaction

Table 5.1: Aggregate gradation

Sieve size (mm)	12.5	9.5	4.75	2.36	1.18	0.6	0.3	0.15	0.075
Percent passing (%)	100	97	75	54	36	25	15	7	4.8

behavior would exhibit a strong size effect. To examine this size effect, three specimen sizes were used in the experiments. The sizes of specimens were controlled by the weight of the loose mixture used to compact the cylindrical specimens: 2.5, 3.5, and 4.5 kg, respectively. For each specimen size, two replicates were tested.

The standard method for gyratory compaction, AASHTO T312 [120], was followed. The loose mixture and the cylindrical gyratory mold were first heated in the oven at the compaction temperature. The mixture was then poured into the gyratory mold and compacted using the gyratory compactor of a diameter of 150 mm. During compaction, the height of the specimen h was recorded after each gyration. In this research, all specimens were subjected to 200 gyrations; the compaction temperature was 130°C. According to AASHTO T312 [120], the external pressure P is 600kPa; the gyration angle β is 1.16°; and the rate of gyration ω is 30 times per minute.

The temperature of the specimens was measured before and after the compaction. At the beginning of the compaction, all specimens have a similar temperature, which is slightly lower than the oven temperature 130°C. During the compaction process, the temperature of the specimen drops. It was observed that small specimens experience a more pronounced temperature drop. The temperature of 2.5 kg specimens decreases from 128°C to 96°C whereas, for 4.5 kg specimens, the temperature drops from 125.5°C to 105.7°C. This difference in temperature change is due to the fact that small specimens have a larger surface-to-volume ratio, which allows more heat dissipation.

At the end of gyratory compaction, the final bulk density of the compacted specimen ρ^f_{ave} was measured following AASHTO T166 [47]. The results are shown in Table 5.2. Based on the measured evolution of specimen height, the average bulk density of the specimen at the Nth gyration, $\rho_{ave}(N)$, can be calculated as

$$\rho_{ave}(N) = \rho^f_{ave}\frac{h^f}{h(N)} \tag{5.20}$$

where $h(N)$ denotes the specimen height at the Nth gyration. h^f denotes the final height of the specimen. The average packing fraction of the specimen at the Nth gyration, $\phi_{ave}(N)$,

can then be calculated as

$$\phi_{ave}(N) = \frac{\rho_{ave}(N)}{\rho_m} \tag{5.21}$$

Table 5.2: Average bulk density of compacted specimens

Specimen weight, kg	2.5		3.5		4.5	
	1	2	1	2	1	2
ρ^f_{ave}, g/cm^3	2.391	2.382	2.425	2.43	2.438	2.435

Fig. 5.3 shows the relationship between the average packing fraction ϕ_{ave} and the number of gyrations N, which is referred to as the compaction curve in this research. It is seen that, for all specimens, the compaction curves feature the same behavior. The packing fraction increases quickly during the early stage of the compaction ($0 < N < 50$), and in the subsequent gyrations the increase in packing fraction occurs at a much slower rate. This behavior is well expected since it becomes more difficult to rearrange the aggregates at a higher packing fraction.

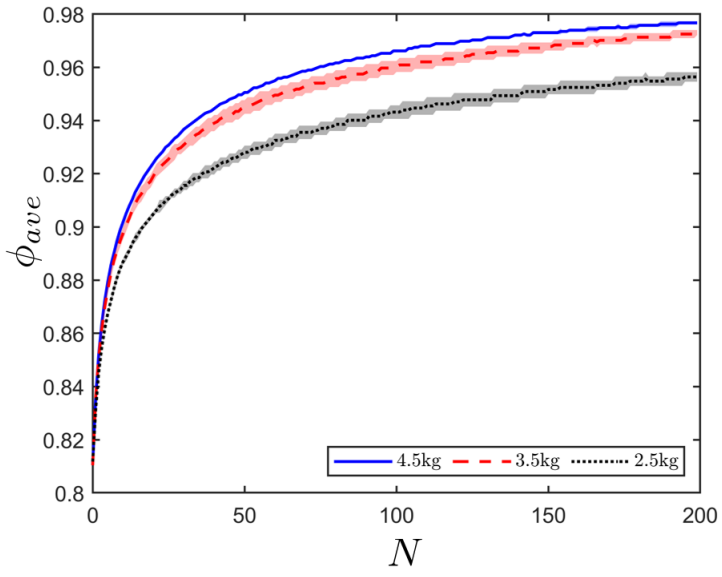

Figure 5.3: Experimental compaction curves of different size specimens (lines denote the average response and shaded areas denote the scatter of the data).

The notable result of the present experiment is that the specimen size has a profound effect on the compaction curve. For a given number of gyrations, the packing fraction of large

specimens is higher than that of small specimens. In other words, it is easier to compact large specimens as compared to small specimens. As shown in Fig. 3, the difference in compaction curve between specimens of different sizes occurs mainly at the initial stage of the compaction ($0 < N < 50$). In the later stage of the compaction, this difference remains almost unchanged. During the early stage of the compaction, the difference in temperature drop in specimens of different sizes would not be significant. Therefore, we may conclude that the difference in the measured compaction curves for specimen of different sizes is not due to the temperature effect. Within the framework of the present model, the effect of specimen size on the compaction curve is attributed to the nonlocality of the rearrangement of aggregates in the viscous binder.

5.4 Simulation of Gyratory Compaction Experiments

The proposed model is used to simulate the aforementioned compaction experiments. The initial specimen height and initial packing fraction are measured for each specimen prior to the experiments: $\phi_0 = 0.81$, and $L = 127$, 99, 72 mm for 4.5, 3.5, 2.5 kg specimens, respectively. The remaining parameters, C_1, C_2, k, l_a and ϕ_t, need to be calibrated. Due to the nonlocality, one cannot uniquely determine these parameters by the optimum fitting of the compaction curve of one specimen size. In this study, the model parameters are calibrated by fitting of the measured compaction curves of 127 mm and 99 mm specimens, and the calibrated model is then used to predict the compaction curve of 72 mm specimens.

Fig. 5.4 shows the optimum fitting of the experimental compaction curves of 127 mm and 99 mm specimens by the present model. It is seen that the model can match the experimental results of these two different size specimens very well, with the coefficients of determination, R^2's, being 99.55% and 99.69% for 127 mm and 99 mm specimens respectively. The fitting yields the following values of the model parameters $l_a = 20$ mm, $C_1 = 0.033$ MPa^{-1}s^{-1}, $C_2 = 341$, $k = 2.5$, and $\phi_t = 0.8$. Note that the calibrated nonlocal influence length is about twice the nominal maximum aggregate size.

These fitted parameters are then used to simulate the gyratory compaction of 72 mm specimen. As shown in Fig. 5.4, the prediction is in good agreement with the measured compaction curve. The essence of the present model is its capability of capturing the effect of specimen size on the compaction curve. This is the key consequence of employing the nonlocal model, which contains a characteristic material length scale invariant with the

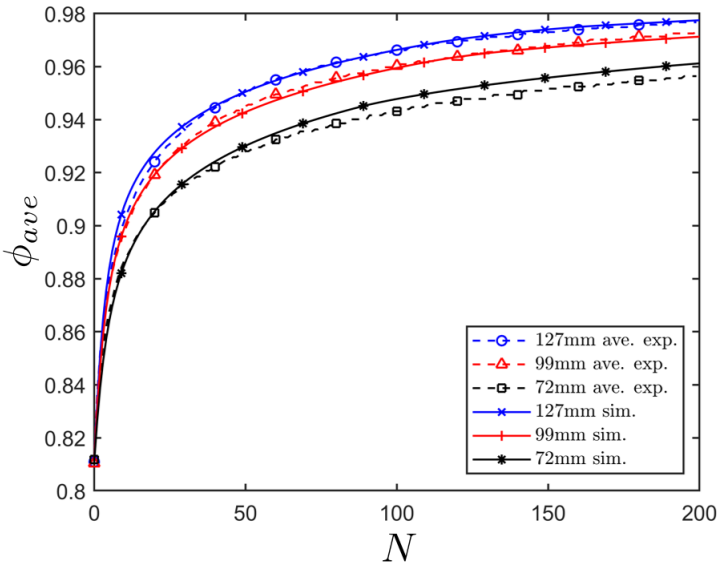

Figure 5.4: Comparison between experimental and simulated compaction curves of different size specimens.

specimen size. The effect of the nonlocality on the compaction behavior will be further discussed in the next section.

A common feature of the compaction curve is that the specimen first exhibits a high compaction rate, which is indicated by the slope of the compaction curve. As the compaction process proceeds, the compaction rate decreases significantly and the compaction curve flattens eventually. This collective behavior is well captured by Eq. 5.13 of the present model, which predicts a decreasing local densification rate for an increasing packing fraction.

In addition to compaction curves, the model also simulates the evolution of packing fraction profiles, as shown in Fig. 5.5a, b and c for the three different specimen sizes. It can be seen that for all specimen sizes, as the number of gyrations increases, the packing fraction profile evolves from the initial uniform distribution gradually to an inverted non-uniform distribution, which is featured by a low local packing fraction near the specimen ends, and relatively high local packing fraction in the middle. Such a spatial distribution of local packing fraction has been observed in previous experimental studies [113, 114, 3, 34] and DEM simulations [27].

The emergence of the non-uniform distribution of the local packing fraction can be attributed to the restriction of the rigid loading plates on the aggregate rearrangement

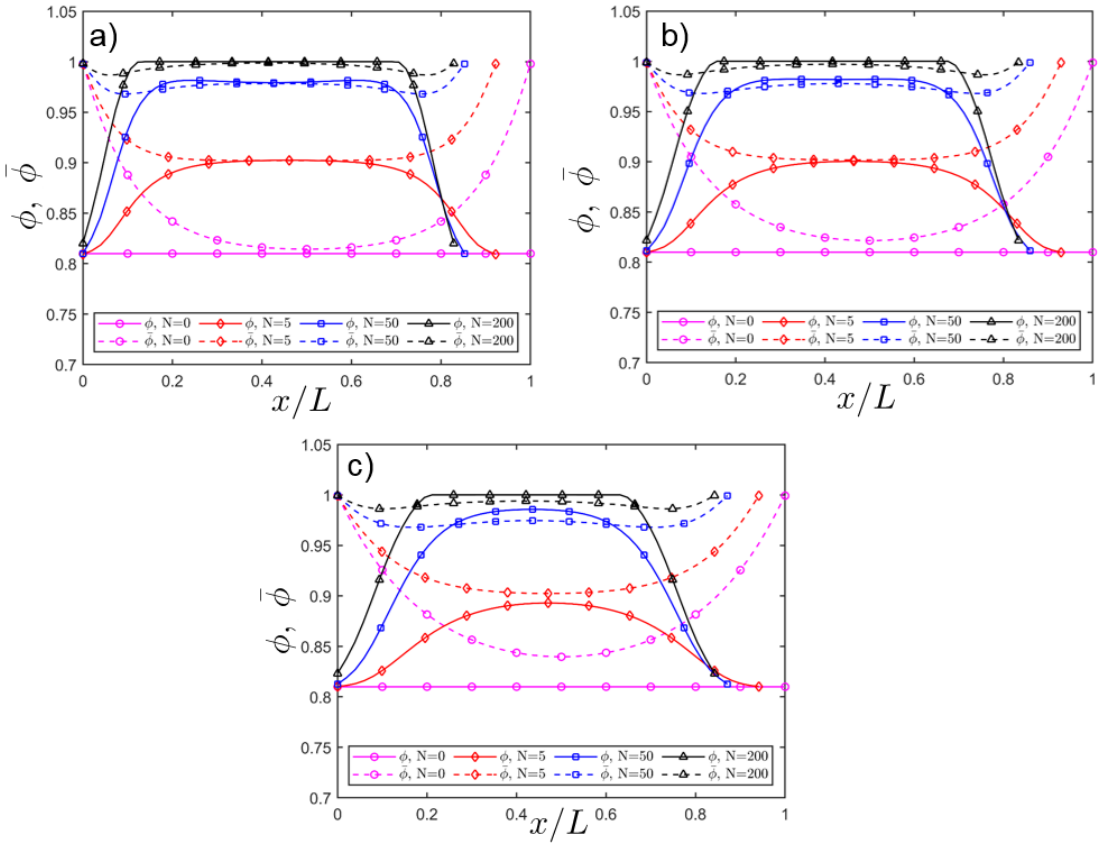

Figure 5.5: Simulated evolution of local and nonlocal packing fraction profile of different size specimens: a) 4.5kg specimen, b) 3.5kg specimen, and c) 2.5kg specimen.

and the nonlocal effect. The movement of aggregates near the two ends are significantly restrained by the loading plates, whereas this restraint effect gradually fades for aggregates that are away from the ends. In the present model, the effect of the rigid plates is captured by the nonlocal boundary condition (Eq. 5.11), which imposes a very low densification rate at the specimen ends. The gradual fading of this boundary effect towards the middle is described by the nonlocal model, where the nonlocal length governs how fast the restrain effect of the rigid plates disappears as we move away from the two ends. The model predicts a decreasing nonlocal packing fraction from the two ends towards the middle, as shown in Figs. 5.5 a-c. This behavior implies that the densification rate increases from the two ends towards the middle.

Based on the simulated spatial distribution of ϕ and $\bar{\phi}$ (Figs. 5.5 a-c), we can divide

the specimens into two parts: 1) transition region occurring near the two ends, in which the local packing fraction shows a considerable increase, and 2) stable region in the middle part, in which the local packing fraction exhibits almost a constant value. The foregoing discussion indicates that the material in the transition region is strongly affected by the boundary effect whereas the material in the stable region is less affected.

Comparison between Figs. 5.5a, b and c reveals a strong effect of specimen size on the spatial distribution of both local and nonlocal packing fractions. It is seen that the ratio of the transition region to the entire specimen size decreases as the specimen size increases. The size of transition region can be understood as the size range of the material that is affected by the rigid plates. In the present model, this size is intimately related to the nonlocal length scale l_a. In fact, the absolute size of the transition region for 72, 99, 127mm specimens is almost a constant. On the other hand, the local packing fraction of the stable region is almost a constant for all specimens. This implies that, at certain number of gyrations, large specimens would exhibit a higher average local packing fraction, which explains the size effect observed in Fig. 5.4.

5.5 Parametric Analysis

5.5.1 Nonlocal averaging length scale

The foregoing discussion reveals the crucial role of nonlocality in prediction of the compaction behavior of the specimen. In a 1D setting, the extent of nonlocal effect can be described by the length ratio l_a/L, Therefore, it is naturally expected that, for a given mixture, specimens of different sizes would exhibit different compaction behaviors. To further investigate the effect of nonlocality on the compaction behavior, we repeat the simulation for a wide range of l_a/L ($l_a/L = 0, 0.05, 0.1, 0.15, 0.2, 0.25, 0.3$), while the other parameters are kept unchanged. We simulate the compaction behavior for 50 gyrations.

Fig. 5.6 compares the simulated compaction curves for these six cases of l_a/L. It is seen that, as l_a/L decreases, the model predicts an increased compatability over the entire compaction process. Fig. 5.7 presents the packing fraction profile at 50 gyrations. It is seen that, for small values of l_a/L, the transition region becomes negligible. Therefore the specimen exhibits a lower overall nonlocal packing fraction, and consequently a higher densification rate and an increase in compatability. As l_a/L decreases to zero, the compaction

curve converges a limiting form, which corresponds to the solution of the local model.

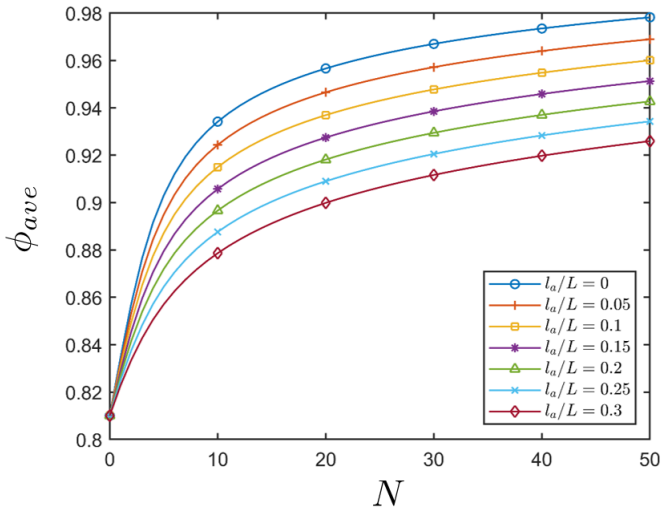

Figure 5.6: Effect of l_a/L on compaction curve.

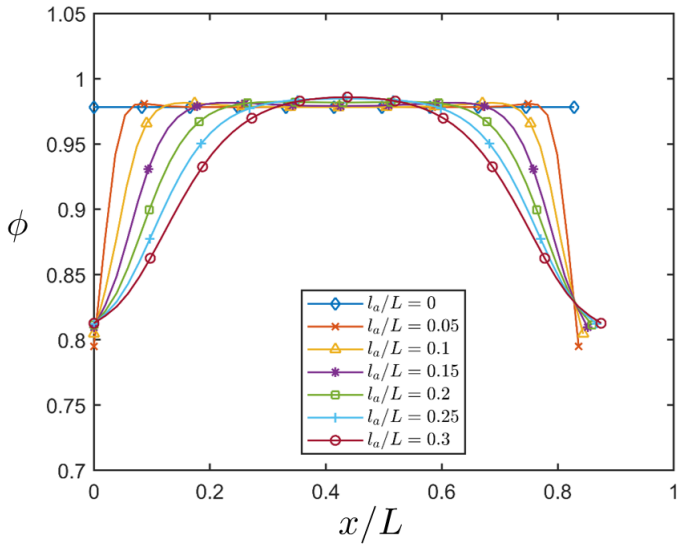

Figure 5.7: Effect of l_a/L on local packing fraction profile.

We denote the size of the transition region by l_m. Fig. 5.8 is generated to show more clear the relationship between l_m and l_a. It is seen that, when $l_a < 0.25L$, we have $l_m \approx 2l_a$, which implies that for a given mixture (given l_a) the size of the transition region is independent of

the specimen size. However, when $l_a > 0.25L$, the size of transition region is about half of the specimen. In this case, l_m is proportional to the specimen size. This is because, when the nonlocal length is sufficiently large, the entire specimen would be affected by the boundary, and therefore the stable region disappears. In this limiting case we have $l_m/L = 0.5$.

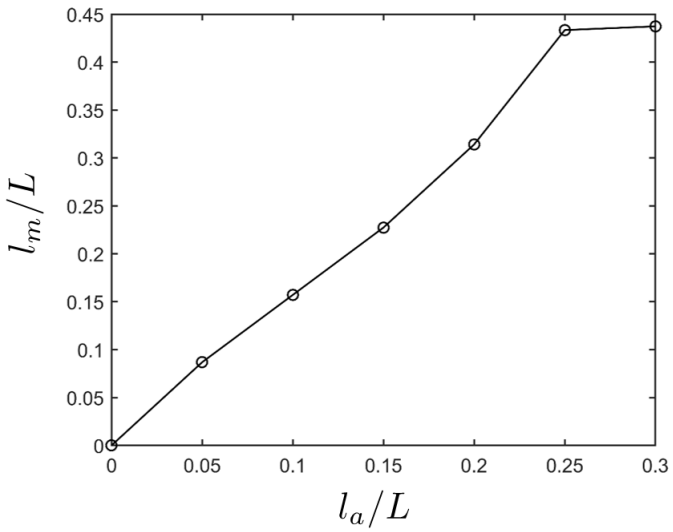

Figure 5.8: Relationship between l_m/L and l_a/L.

The foregoing discussion of nonlocal effect also implies the influence of aggregate size on the compactability of gyratory compaction specimen. Since the nonlocal averaging length is proportional to the maximum aggregate size, it is clear that the specimen with large aggregate size would exhibit a low compactability, which has been observed experimentally [121]. In addition to the maximum aggregate size, the aggregate gradation could also influence the nonlocal averaging length. Such dependence has not been studied so far. Nevertheless, if the size effect experiments on gyratory compaction on specimens made of different aggregate gradations are available, the present model can easily be used to explore the relation between the nonlocality and the characteristics of aggregate gradation described by some existing methods such as the Bailey method and the maximum density line [21, 20].

5.5.2 Parameters C_1, C_2 and k

Parameters C_1, C_2 and k influence the compaction process through the densification model (Eq. 5.13). These parameters are closely related to the material properties and gyratory

motion. Table 5.3 shows the three sets of simulation parameters for investigating the effects of C_1, C_2 and k on the overall compaction curve. In this set of parametric studies, we consider $l_a/L = 0.15$ and $\phi_t = 0.80$.

Table 5.3: Parameters for investigation of the effect of C_1, C_2 and k

Set	C_1 ($\text{MPa}^{-1}\text{s}^{-1}$)	C_2	k
1	0.01, 0.02, 0.03, 0.04, 0.05, 0.06	341	2.5
2	0.033	200, 300, 400, 500, 600, 700	2.5
3	0.033	341	1.5, 2.0, 2.5, 3.0, 3.5, 4.0

Figs. 5.9a-c show the effects of the parameters C_1, C_2 and k on the densification model respectively. It is seen that C_1 has a significant influence on the the densification rate when the nonlocal packing fraction $\bar{\phi}$ is close to ϕ_t. As $\bar{\phi}$ increases, the effect of C_1 on the densification rate attenuates. This behavior is reflected in Fig. 5.10a, which shows that a larger value of C_1 lead to a significant increase in the initial compaction rate, while compaction rate during the later stage of the process is not affected by parameter C_1.

In contrast to C_1, both parameters C_2 and k have a pronounced effect on the densification rate for intermediate values of $\bar{\phi}$ (Figs. 5.9 b and c). Figs. 5.10 b and c show the effects of C_2 and k on the compaction curve. It is seen that the compactability improves when C_2 decreases or k increases. As indicated by Figs. 5.9 b and c, the initial compaction rate is not affected by parameters C_2 and k. These parameters have a strong influence over the wide intermediate stage of the compaction process. Figs. 5.10 b and c also shows that, as compared to C_2, parameter k has a stronger effect on the compaction curve.

It is worthwhile to discuss the physical significance of parameters C_1, C_2 and k in terms of their relation to the loading conditions and material properties. Based on Eq. 5.13, C_1 and C_2 are related to the kinetic energy E_s of the aggregates in the cluster. For a given material, E_s is governed by the gyratory motion, which can be controlled by the gyratory angle and gyratory speed. An increase in either gyratory angle or gyratory speed would enhance the gyratory motion. Based on the relationships of C_1 and C_2 with E_s, an enhanced gyratory motion would lead to an increasing C_1 and a decreasing C_2. Therefore, the model predicts that both increases in gyratory angle and gyratory speed will accelerate the compaction process, which is consistent with the experimental observations [33, 122].

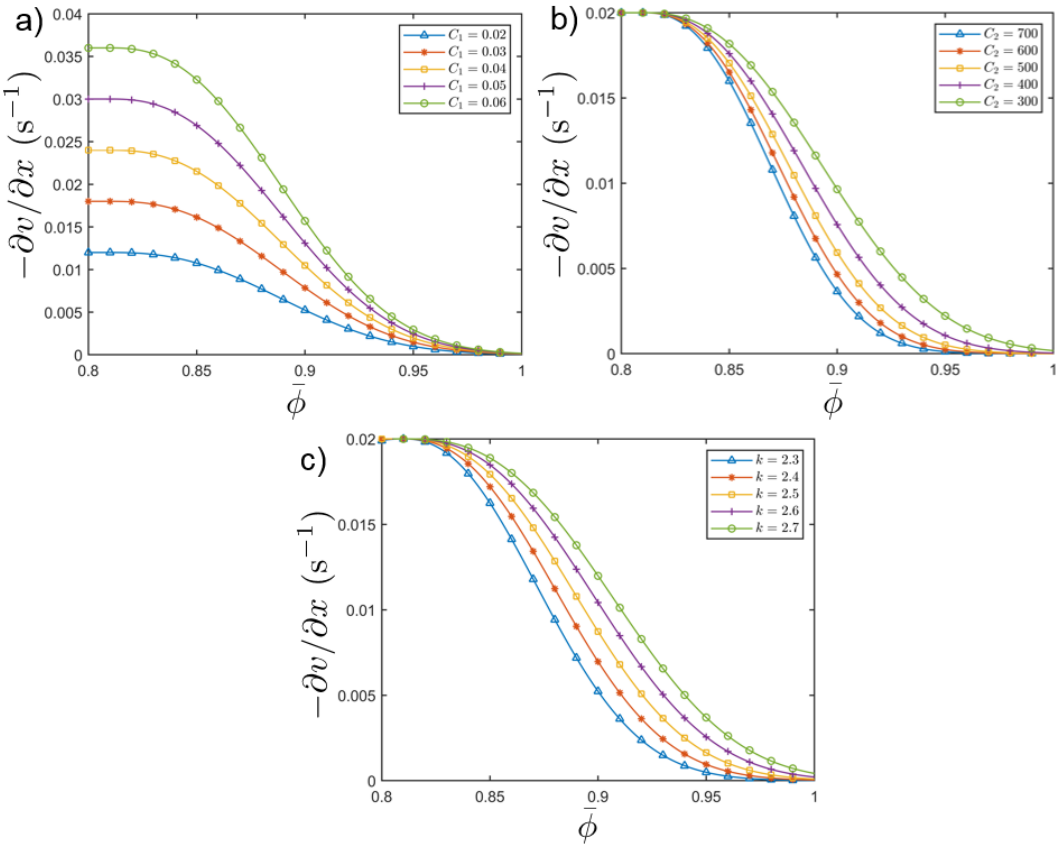

Figure 5.9: Effects of C_1, C_2 and k on nonlocal densification model: a) C_1, b) C_2 and c) k.

Meanwhile, C_1, C_2 and k also manifest the effect of material properties on the compactability of the mixture. It is widely accepted that the viscosity of binder is a key factor for the compaction process of asphalt mixture. In the present model, a higher binder viscosity implies a higher initial free energy barrier U_0 of aggregate rearrangements, and a more significant increase in the energy barrier due to the increase in packing fraction (i.e. a higher value of U_1 and a lower value of k), and meanwhile a lower reference frequency f_0 of transition between two adjacent states. This indicates a decrease in C_1 and k and an increase in C_2, which leads to a decrease in densification rate and a lower compatibility. Since the binder viscosity increases with decreasing temperature, the predicted effect of binder viscosity can also be used to explain the temperature effect on the compaction process.

In addition to the viscosity of binder, the angularity of the aggregates has a profound influence on compactability [21, 16, 123], and different experimental methods have been

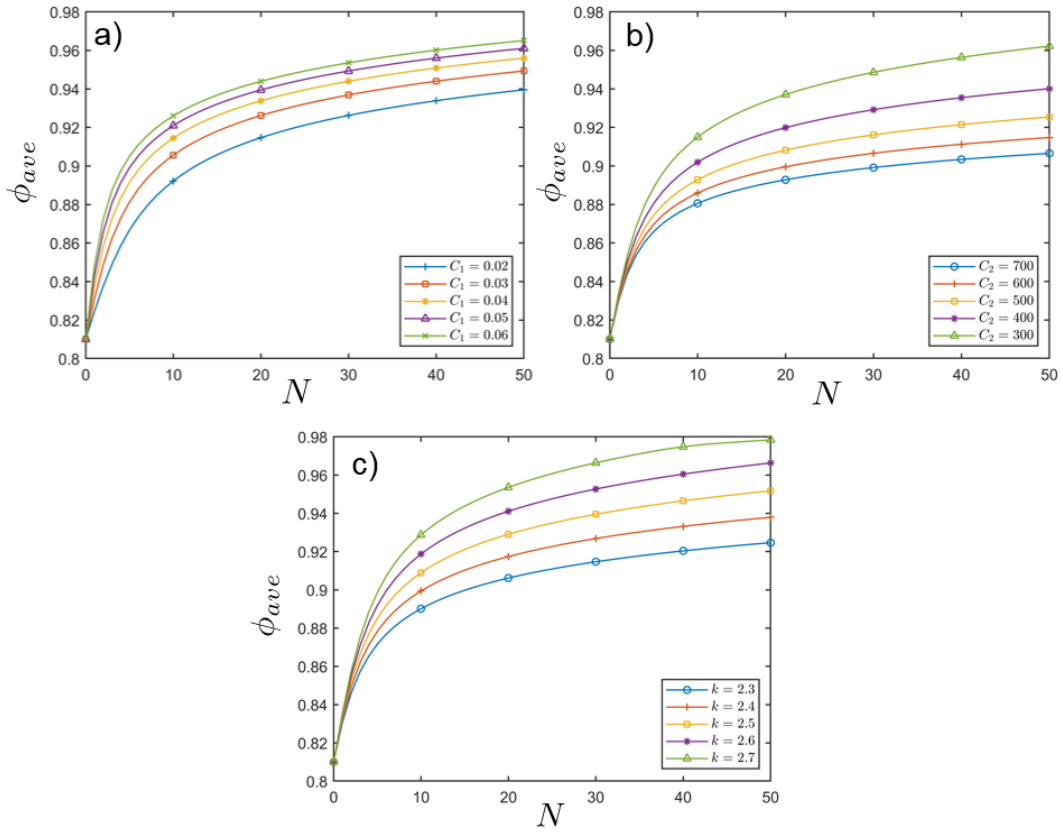

Figure 5.10: Effects of C_1, C_2 and k on compaction curve: a) C_1, b) C_2 and c) k.

developed to measure the angularity [45, 46]. The present model predicts the similar effect of aggregate angularity on compactability as that of binder viscosity. Large angularity will lead to a lower value of f_0, and a higher and steeper increasing U_b, which consequently decelerates the compaction process, which has been observed experimentally [21, 16, 123].

It should be mentioned that C_1, C_2 and k may also depend on other properties, such as the aggregate gradation. It is clear that a desirable aggregate gradation would correspond to a low free energy barrier and a high reference frequency of transition. Therefore, it is expected that the effect of aggregate gradation is qualitatively similar to that of binder viscosity and aggregate angularity. The quantitative relation between the characteristic of aggregate gradation and free energy barrier and reference frequency could be determined through optimum fitting of the measured compaction curves by the present model.

5.6 Conclusions

A one-dimensional nonlocal model is developed for simulate the gyratory compaction of asphalt mixtures. The model is formulated by combining the local mass balance law and a densification model of a cluster of aggregates. Inspired by the transition rate theory, the densification model relates the transition rate between adjacent states to the energy inputs by the gyratory motion and compression as well as to the nonlocal packing fraction.

The model predicts an intricate effect of specimen height on the overall compaction curve. It shows that, for a given number of gyration, the average packing fraction of the specimen decreases as the specimen height decreases. Meanwhile, the final spatial distribution of local packing fraction is also strongly dependent on the specimen height. The predicted size dependence of compaction behavior can be explained by the nonlocality of the local densification rate.

A set of gyratory compaction tests is performed on hot asphalt mixture specimens of different heights. The test results show that the compaction curve is strongly dependent on the specimen height. The comparison between the model prediction and experimental results validates the present model, which demonstrates the critical role of nonlocality in the continuum modeling of gyratory compaction.

Through a set of parametric studies, it is shown that the nonlocal length scale plays a critical role in determining the spatial distribution of the local packing fraction and consequently the overall compaction curve. The model parameters can be related to the set up of the gyratory compaction and the material properties, such as the binder viscosity, angularity of aggregates, and aggregate gradation. The model yields predictions on the qualitative effect of material properties on the compaction behavior, which are consistent with existing experimental observation. A more extensive experimental investigation would be required to establish the quantitative relations between these properties and compatibility.

Chapter 6

Effect of Randomness on Compaction of Hot Asphalt Mixtures

Randomness is inevitable in the construction process of asphalt pavements. Thus, characterizing randomness and its effect are essential for designing reliable asphalt pavements. In Chapter 5, a 1D nonlocal model was developed to simulate gyratory compaction process of asphalt mixtures. However, the effect of randomness is not studied; all model parameters were deterministic in Chapter 5. Based on the model developed in Chapter 5, this chapter focuses on investigating the effects of randomnesses on the gyratory compaction process of hot asphalt mixtures. To this end, the initial density profile and compaction effort are considered as a Gaussian random field and a normal random variable respectively. Monte Carlo simulations are then performed based on the 1D nonlocal model to compute the probability distribution of the average densities of gyratory compacted samples. Effects of the randomness in initial density profile and in compaction effort on the distribution of average density are studied.

6.1 Introduction

Field density is an important factor for the durability of asphalt pavement, and it is one of the main focuses of the quality control and quality assurance (QC/QA) of asphalt pavement construction. As have been analyzed in Chapter 2, field density exhibits considerable randomness, with the standard deviation being around 1.5 $\%G_{mm}$ in Minnesota (see Fig. 6.1

for an example of field density distribution). Such randomness level of field density clearly indicates that reliability concepts must be considered when designing the compaction of asphalt pavements.

However, we are still having a limited understanding of the field density distribution. For example, it is obscure why field density distribution is always left-skewed (skewness < 0) and leptokurtic (kurtosis > 3), as exemplified in Fig. 6.1. Understanding these features will be of critical importance for the reliability analysis of the compaction of asphalt pavements.

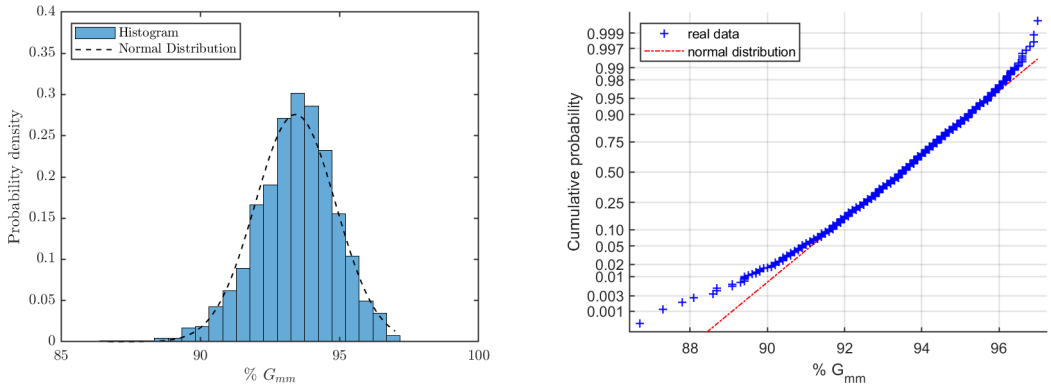

(a) (b)

Figure 6.1: Field density distribution of real projects (mean, standard deviation, skewness and kurtosis of the data are 93.4%, 1.45%, -0.44 and 3.68 respectively), (a) histogram, and (b) normal probability plot.

The randomness of field density is expected to arise from the randomness of the compaction process of asphalt mixtures, for example, the compaction effort, the material compositions, and the initial density. Therefore, to understand the features of field density distribution, it is important to understand how randomness in these factors affecting compaction process. To this end, the 1D nonlocal model for gyratory compaction presented in Chapter 5 is employed to simulate the compaction process, where the inputs of this model are considered as random variables. More specifically, randomness in the initial density profile ($\phi_0(x)$) and compaction effort (number of gyrations, N) are considered as a Gaussian random field and a Gaussian random variable respectively. Monte Carlo simulations are then performed to explore the effects of those random inputs on the probability distribution of the average density of gyratory specimens. By the results, the origin of the left-skewed and leptokurtic properties in the field density distribution is explained. Moreover, the implications

of the results on the reliability design of asphalt pavement compaction are discussed.

6.2 Simulate Initial Density Profile as a Gaussian Random Field

In Chapter 5, when simulating the gyratory compaction process, the initial density profile $\phi_0(x)$ is assumed as a constant. However, in reality, the initial density profile is a random field. $\phi_0(x)$ can be think of affected by numerous factors additively, so due to central limit theorem it is reasonable to assume $\phi_0(x)$ as a Gaussian random field. This section then focuses on the methodology of generating Gaussian random fields.

A Gaussian random field is characterized by a mean function $\bar{\phi}_0(x)$ and a covariance function $R(x, x')$. Assuming that the random field of $\phi_0(x)$ is stationary and isotropic, $R(x, x')$ can be simplified to $R(\tau)$, where τ is the distance, $\tau = |x - x'|$; and $\bar{\phi}_0(x)$ can be simplified as a constant, $\bar{\phi}_0(x) = c$. The covariance function is chosen as the squared exponential form as shown in Eq. 6.1, which simulates the fact that the correlation of the densities of two material points decreases as the increase in their distance.

$$R(\tau) = \sigma^2 \exp(-\frac{\tau^2}{2l_c^2}) \tag{6.1}$$

where σ is the standard deviation of the initial density at a local point; l_c is related to the autocorrelation length. More specifically, the autocorrelation length $\approx 3l_c$

6.2.1 Numerical Method: Spectral Method

To numerically simulate the Gaussian random field, the spectral method proposed by [124] is followed. First, the covariance function is transformed to the power spectral density function $S(\omega)$ by the Wiener-Khintchine Transformation.

$$S(w) = 1/2\pi \int_{-\infty}^{+\infty} R(\tau) \exp(-i\omega\tau) d\tau = \frac{\sigma^2 L}{\sqrt{2\pi}} \exp(-L^2\omega^2/2) \tag{6.2}$$

Then, the Gaussian random initial density field can be simulated by using the following series as $I \to +\infty$ [124]

$$\phi_0(x) = \sqrt{2} \sum_{i=1}^{I} A_n \cos(\omega_i x + \Phi_i) \tag{6.3}$$

where $\omega_i = i\omega_u/I$; $A_n = (2S(\omega_n)\omega_u/I)^{1/2}$; Φ_i are independent random phase angles distributed uniformly over the interval $[0.2\pi]$; ω_u is the upper cut-off frequency. Sufficient large I and ω_u shall be chosen to ensure accuracy.

Fig. 6.2 shows three realizations by the spectral method within a spatial domain of 100 mm . The following parameter values are used in the simulation: $\sigma = 0.02$, $l_c = 5$ mm, $\bar{\phi}_0 = 0.81$.

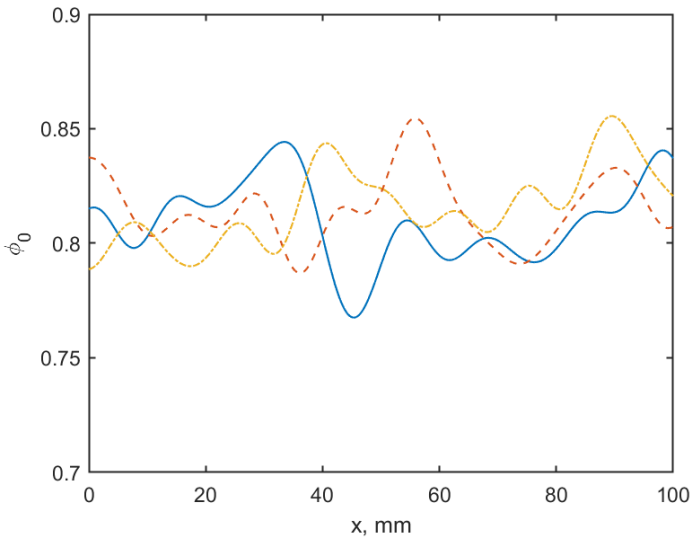

Figure 6.2: Three realizations of initial density profile simulated as Gaussian random field

To check the validity of this numerical method, the covariance function is estimated numerically by 10000 realizations, and then is compared with the target covariance function (Eq. 6.1). As shown in Fig. 6.3. the covariance function computed from the numerical simulation matches well the target covariance function. Therefore, the validity of Gaussian random field simulation is checked.

6.2.2 Estimate σ and l_c

It seen from Eq. 6.1 that the Gaussian random field of $\phi_0(x)$ can be fully described by the parameters σ and l_c. In this section, we try to estimate the magnitude of their values by using experimental data noted in a previous literature [3]. The test data are reprinted in Fig. 6.4 from the original paper [3]. The mixture tested in this research has a nominal maximum aggregate size (NMAS) of 19mm. The air voids $(1 - \phi)$ profile data at the 8 gyrations is

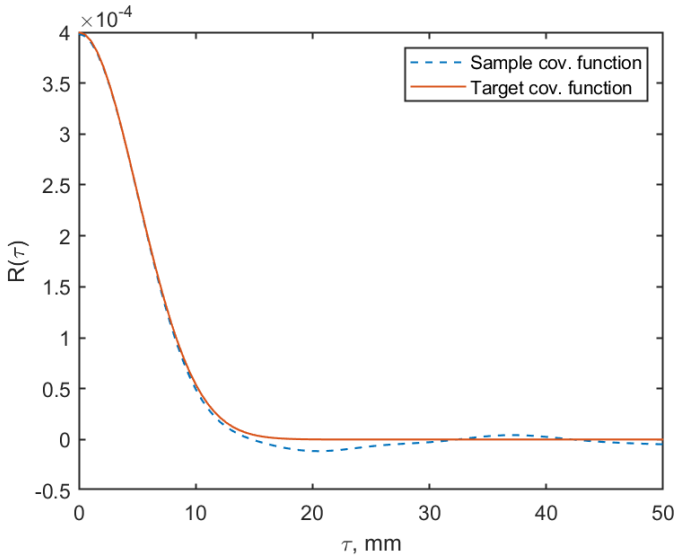

Figure 6.3: Comparison between the target covariance function and that computed from numerical simulated samples

extracted as shown in Fig. 6.5.

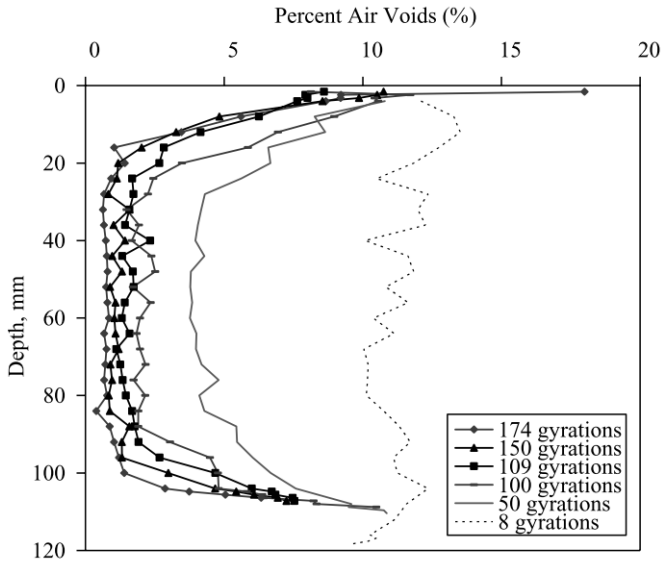

Figure 6.4: Air voids profile data reprinted from the paper [3]

Data in Fig. 6.5 are used to estimate the parameters of covariance function. Due to

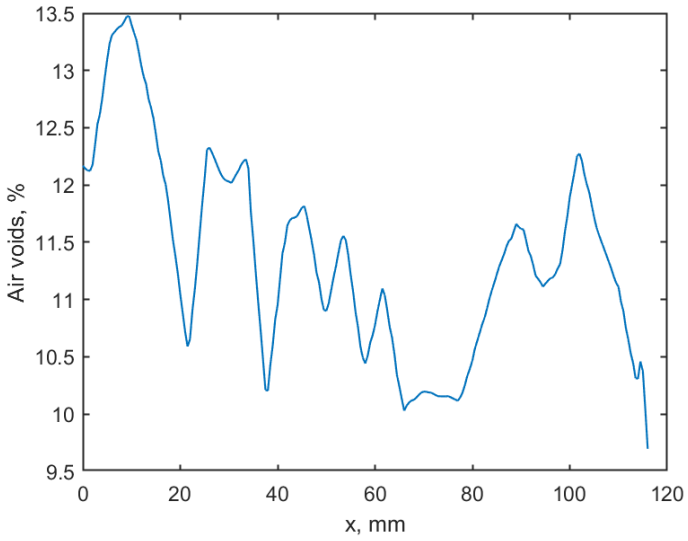

Figure 6.5: Initial air voids profile extracted from Fig. 6.4

ergodicity, $\bar{\phi}_0$ and $R(\tau)$ can be computed by the following spatial averages:

$$\bar{\phi_0} = \lim_{X\to\infty} \frac{1}{X} \int_0^X \phi_0(x)dx \tag{6.4}$$

$$R(\tau) = \lim_{X\to\infty} \frac{1}{X} \int_0^X (\phi_0(x) - \bar{\phi}_0)(\phi_0(x+\tau) - \bar{\phi}_0)dx \tag{6.5}$$

Since the data is only available in the finite domain of specimen size $[0, L]$, so the above expressions can only be approximately estimated by the following equation when $\tau \ll L$:

$$\bar{\phi} \approx \frac{1}{L} \int_0^L \phi_0(x)dx \tag{6.6}$$

$$R(\tau) \approx \frac{1}{L-\tau} \int_0^{L-\tau} (\phi_0(x) - \bar{\phi}_0)(\phi_0(x+\tau) - \bar{\phi}_0)dx \tag{6.7}$$

By these approximations, the estimated $R(\tau)$ is plotted in Fig. 6.6. It is important to note that Eq. 6.7 deviates from Eq. 6.5 as τ gets larger. Therefore, only the estimated $R(\tau)$ at τ close to zero is fitted to Eq. 6.1, as shown in Fig. 6.6. The fitted results are: $\sigma = 0.0083$, $l_c = 6.27$mm. Note that this estimation of σ and l_c can be very crude and may not be representative for mixtures with different aggregate size. However, the aim here is to

just estimate the order of magnitudes of these parameters based on data of real mixtures, which will provide with us some guidance when choosing the values of these parameters in the later sections. Moreover, notably, the estimated autocorrelation length ($3l_c$=18.8mm) is close to the nominal maximum aggregate size (NMAS), 19mm.

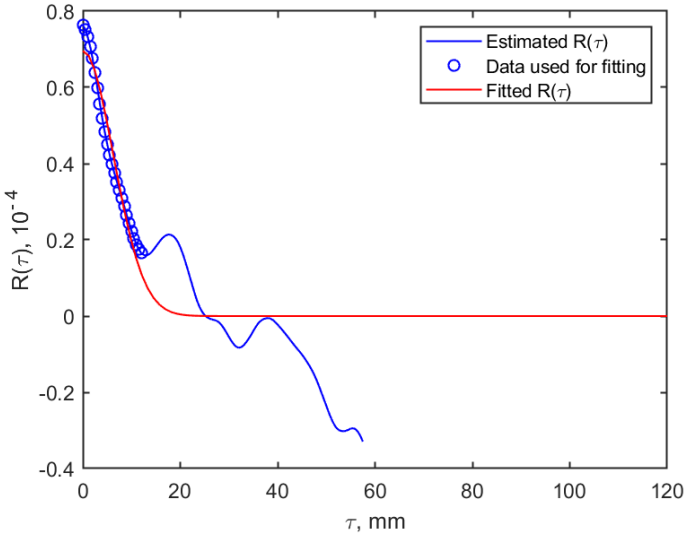

Figure 6.6: Fit the estimated $R(\tau)$ to Eq. 6.1

6.3 Gyratory Compaction Simulation with Random Initial Density Profile

In this section the initial density profile is considered as Gaussian random in the simulation of gyratory compaction. Compared with Section 5.4, the same material parameter values are used: $l_a = 20$ mm, $C_1 = 0.033$ MPa^{-1}s^{-1}, $C_2 = 341$, $k = 2.5$, $\phi_t = 0.8$. Three additional parameters, $\bar{\phi}_0$, σ, l_c, are needed to characterize the random field of initial density profile. The mean of random initial density profile $\bar{\phi}_0$ is chosen as 0.81 which is constant initial density used in Section 5.4. Based on the estimation in Section 6.2.2 and considering that the NMAS of the mixture (9.5 mm) is one half of of that in Section 6.2.2, we set $\sigma = 0.01$ and $l_c = 3$ mm.

Similar to Chapter 5, gyratory compaction processes of three specimen sizes are simulated. The initial specimen heights L are 127, 99, 72 mm respectively. Fig. 6.7 shows the

simulated gyratory compaction processes of the three specimen sizes.

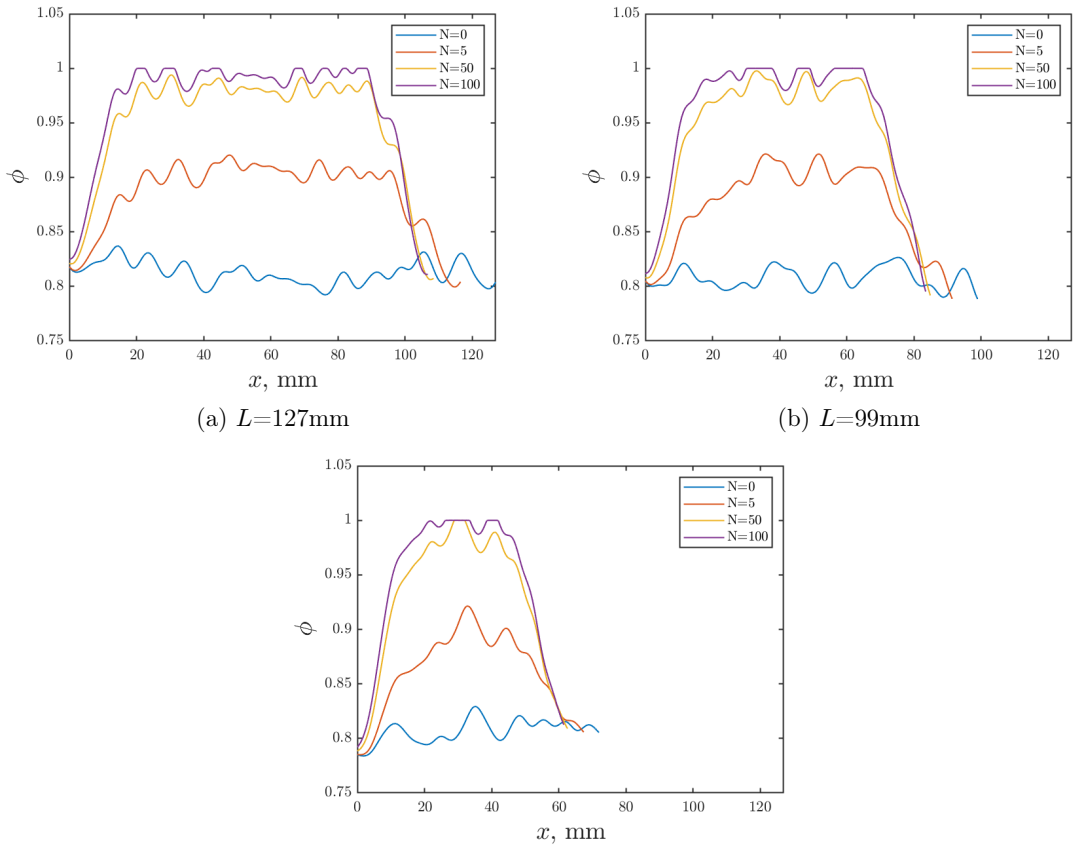

(a) L=127mm

(b) L=99mm

(c) L=72mm

Figure 6.7: Simulated gyratory compaction process for different specimen sizes, considering randomness in initial density profile

Compared with Fig. 5.5 where $\phi_0(x)$ is considered as a constant, Fig. 6.7 clearly simulates a more realistic case where the density profile exhibit certain amount of randomness. It is also noticed that the evolution of the density profile in Fig. 6.7 follows the same pattern as that in the deterministic case, Fig. 5.5

The simulated evolution of average density ϕ_{ave} with N is shown in Fig. 6.8 compared with the experimental results. It is seen that the simulated evolution of ϕ_{ave} matches well the experimental results. Notably, results in Fig. 6.8 are also similar to the results of the deterministic case, Fig. 5.4, which implies that the randomness in ϕ_0 have a minor effect on the evolution of ϕ_{ave}.

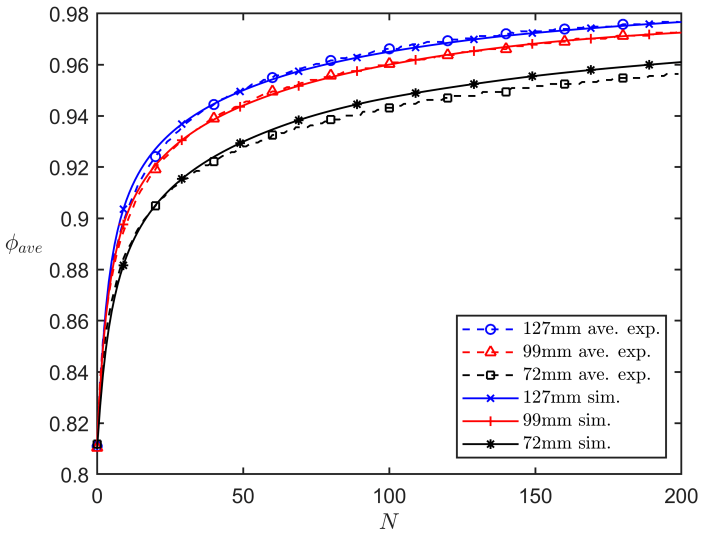

Figure 6.8: Comparison between simulated and experimental compaction curves

6.4 Monte Carlo Simulation–Considering the Randomness in Initial Density Profile

To further explore the effect of the randomness in $\phi_0(x)$ on gyratory compaction, Monte Carlo simulation is performed to compute the probability distribution of ϕ_{ave} due to the randomness in $\phi_0(x)$. We consider the case in which the only uncertainty is from the randomness in $\phi_0(x)$ while material parameters (l_a, C_1, C_2, ϕ_t, and k) are deterministic and of the same values as in Section 6.3. Randomness in $\phi_0(x)$ is characterized by the two parameter of its covariance function (Eq. 6.1), σ and l_c.

6.4.1 Effects of Gyration Number N and Specimen Size L

Due to the randomness in $\phi_0(x)$, ϕ_{ave} becomes a random variable whose probability distribution evolves with the number of gyration N and is affected by the size of specimens L. In this section, we studies the effects of N and L on the probability distribution of ϕ_{ave}.

Three specimen sizes are considered, i.e., L =127, 99, 72mm. For each specimen size, 1000 realizations of gyratory compaction process are simulated, given that the random field of $\phi_0(x)$ is characterized by $\sigma = 0.01$ and $l_c = 3$mm. Then, the probability distribution of ϕ_{ave} is computed at different N's for different specimen sizes based on the simulated

realizations.

The distribution of the simulated compaction curves is plotted in Fig. 6.9. It is plotted in the semi-log scale to show more clearly the difference in ϕ_{ave} at small N values.

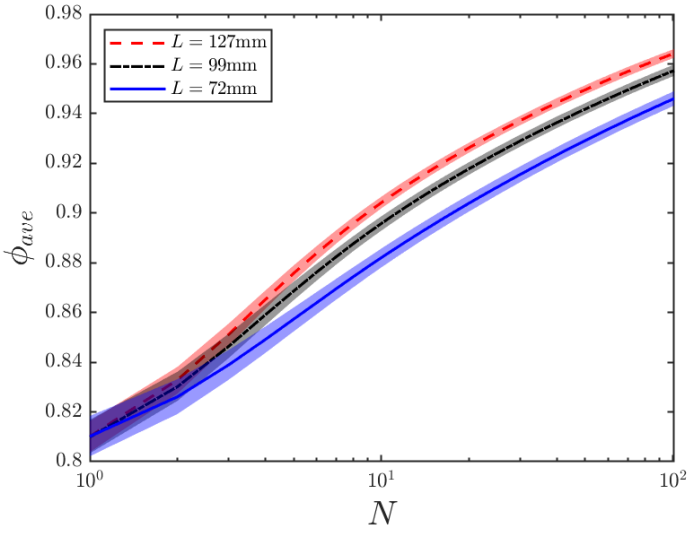

Figure 6.9: Distribution of compaction curves for different specimen sizes (the shaded band shows the range from 5th to 95th percentiles of the data)

It is seen from Fig. 6.9 that the standard deviation of ϕ_{ave} (σ_{ave}) decreases with N. To show more clearly this trend, the relationship between the standard deviation of ϕ_{ave} and N is plotted in Fig. 6.10. This trend is expected given the fact that rate of densification is higher for lower density regions, which is simulated in the present model by the densification rate model Eq. 5.13. This property naturally reduces the variation of ϕ between realizations as N increases. In other words, gyratory compaction is an asymptotic stable process. Since ϕ_{ave} is a spatial average of ϕ, the variation of ϕ_{ave} would also decrease.

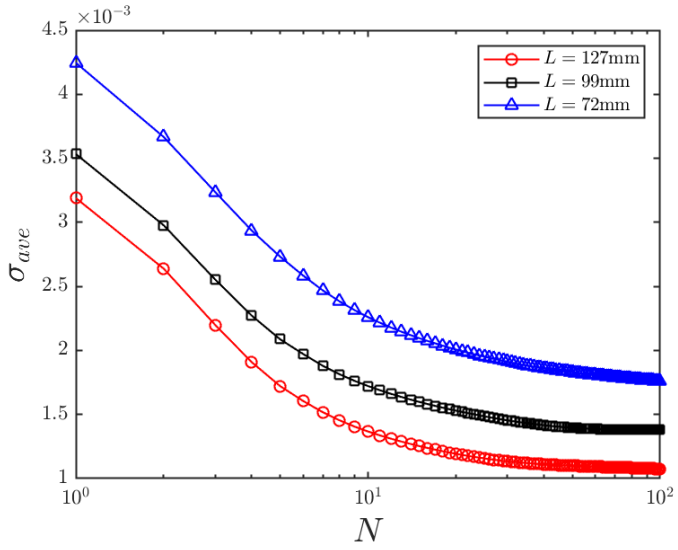

Figure 6.10: Relationship between N and standard deviation of ϕ_{ave}

Fig. 6.9 also shows that the standard deviation of ϕ_{ave} decreases with the increase in specimen size L. To show it more clearly, the relationship between the standard deviation of ϕ_{ave} and L is plotted in log-log scale in Fig. 6.11. As shown, there is an approximate scaling relationship: $\sigma_{ave} \propto L^{-0.5}$. This scaling relationship can be understood through central limit theorem. Given that ϕ_{ave} is a spatial average of ϕ over a domain of length L, it can be shown by central limit theorem that the distribution of ϕ_{ave} converges to normal distribution with

$$\sigma_{ave} \propto \sigma(l_c/L)^{0.5} \tag{6.8}$$

as $L/l_c \to \infty$.

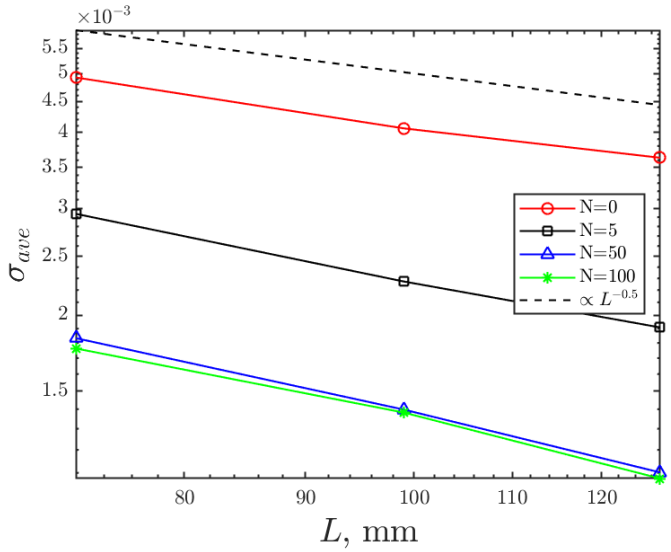

Figure 6.11: Relationship between L and standard deviation of ϕ_{ave}

The distribution of ϕ_{ave} at N=0, 5, 50, for the three different specimen sizes are plotted in Fig. 6.12. It is seen that the distribution of ϕ_{ave} is close to normal distribution.

To check the normality, the distributions of ϕ_{ave} are plotted by the normal probability plots, as shown in Fig. 6.13. It is seen that the distributions of ϕ_{ave} indeed follow normal distributions. Same conclusion can also be reached by checking the skewness and kurtosis values in Table 6.1.

Table 6.1: Basic statistics of the distributions of ϕ_{ave} at different L and N

	mean			st. dev., %			skewness			kurtosis		
N	0	5	50	0	5	50	0	5	50	0	5	50
127mm	0.81	0.884	0.95	0.36	0.17	0.11	-0.022	-0.014	0.003	2.55	2.60	2.72
99mm	0.81	0.876	0.942	0.41	0.21	0.14	0.061	0.009	0.089	2.58	2.77	2.82
72mm	0.81	0.864	0.93	0.49	0.27	0.18	0.053	-0.006	0.010	2.61	2.64	2.85

6.4.2 Effect of σ and l_c

The randomness of $\phi_0(x)$ is fully captured by the parameters in Eq. 6.1, i.e., σ and l_c. Therefore, it is interesting to see how these two parameters affects the probability distribution of ϕ_{ave}. To do that, Monte Carlo simulations are performed for different levels of σ and l_c, as listed in Table 6.2. Only one specimen size, $L = 127$mm, is consider in this section.

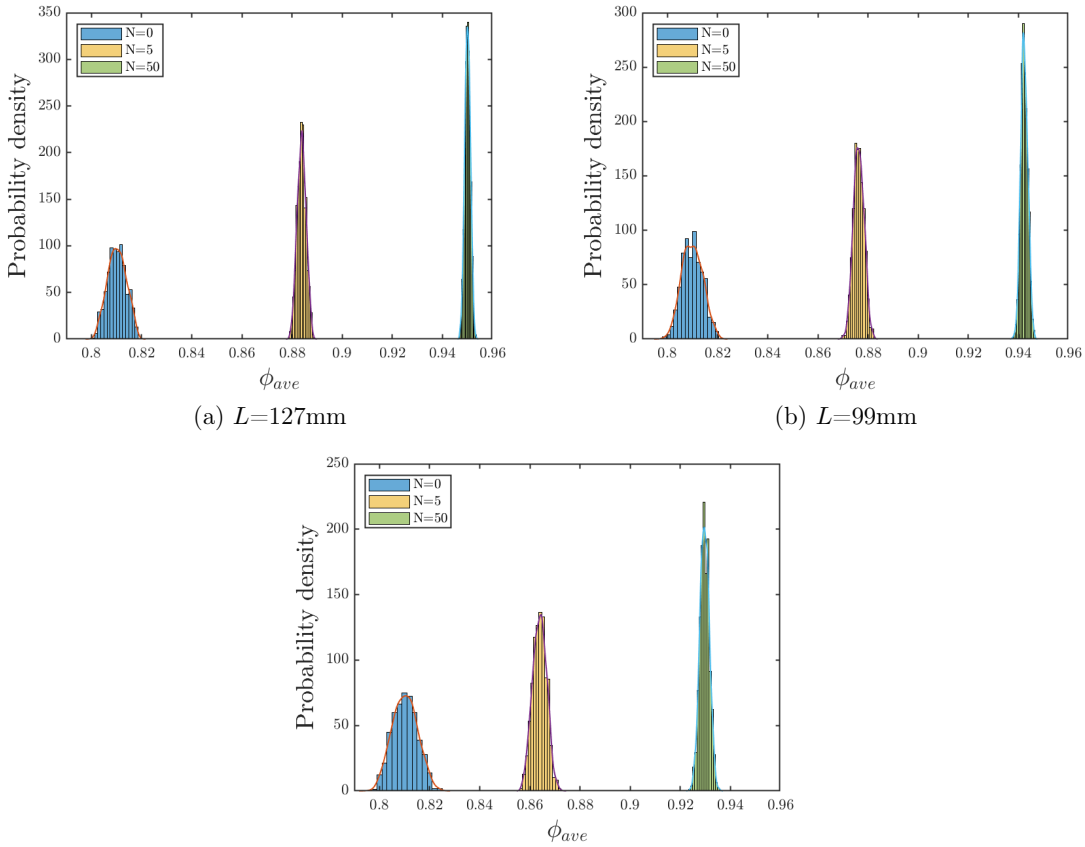

(a) L=127mm (b) L=99mm

(c) L=72mm

Figure 6.12: Distribution of ϕ_{ave} for different specimen sizes

Table 6.2: Values of σ and l_c for the parametric study

Set	σ	l_c, mm
1	0.01, 0.02, 0.03	2
2	0.02	1, 2, 3

We first study the effect of σ on the distribution of ϕ_{ave}. σ is changed to three different levels, while l_c is fixed as 3 mm, as listed in the first set of parameters in Table 6.2. For each σ level, 1000 realizations of gyratory compaction process are simulated in the Monte Carlo method. One realization is shown in Fig. 6.14 for each σ level. Clearly, the variation of ϕ at local points increases with σ.

Distribution of ϕ_{ave} is calculated by the 1000 simulated realizations for different σ levels.

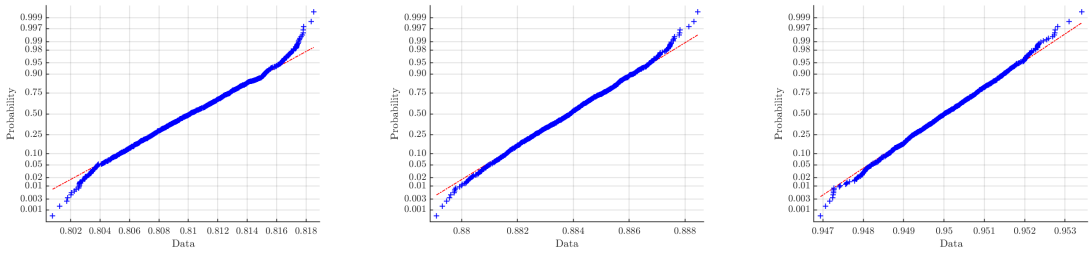

(a) 127mm, N=0 (b) 127mm, N=5 (c) 127mm, N=50

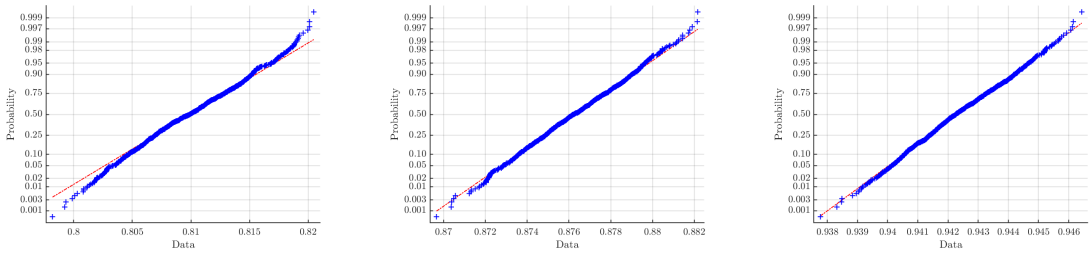

(a) 99mm, N=0 (b) 99mm, N=5 (c) 99mm, N=50

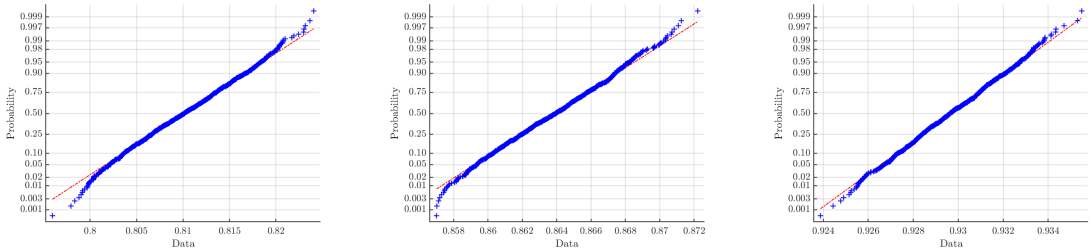

(a) 72mm, N=0 (b) 72mm, N=5 (c) 72mm, N=50

Figure 6.13: Normal probability plots of ϕ_{ave}

Fig. 6.15 shows how σ affects the standard deviation and mean of the ϕ_{ave}. It is seen from the log-log scale plot Fig. 6.15a that there is a scaling relationship: $\sigma_{ave} \propto \sigma$, which confirms Eq.6.8. As shown in Fig. 6.15b, σ has no effect on the mean of ϕ_{ave}.

Then, we study the effect of l_c on the distribution of ϕ_{ave}. l_c is changed to three different levels, while σ is fixed as 0.02, as listed in the second set of parameters in Table 6.2. For each l_c level, 1000 realizations of gyratory compaction process are simulated in the Monte Carlo method. One realization is shown in Fig. 6.16 for each l_c level. Clearly, the average wavelength of the spatial variation of ϕ increases with l_c.

Distribution of ϕ_{ave} is calculated by the 1000 simulated realizations for different l_c levels. Fig. 6.17 shows how l_c affects the standard deviation and mean of the ϕ_{ave}. It is seen from

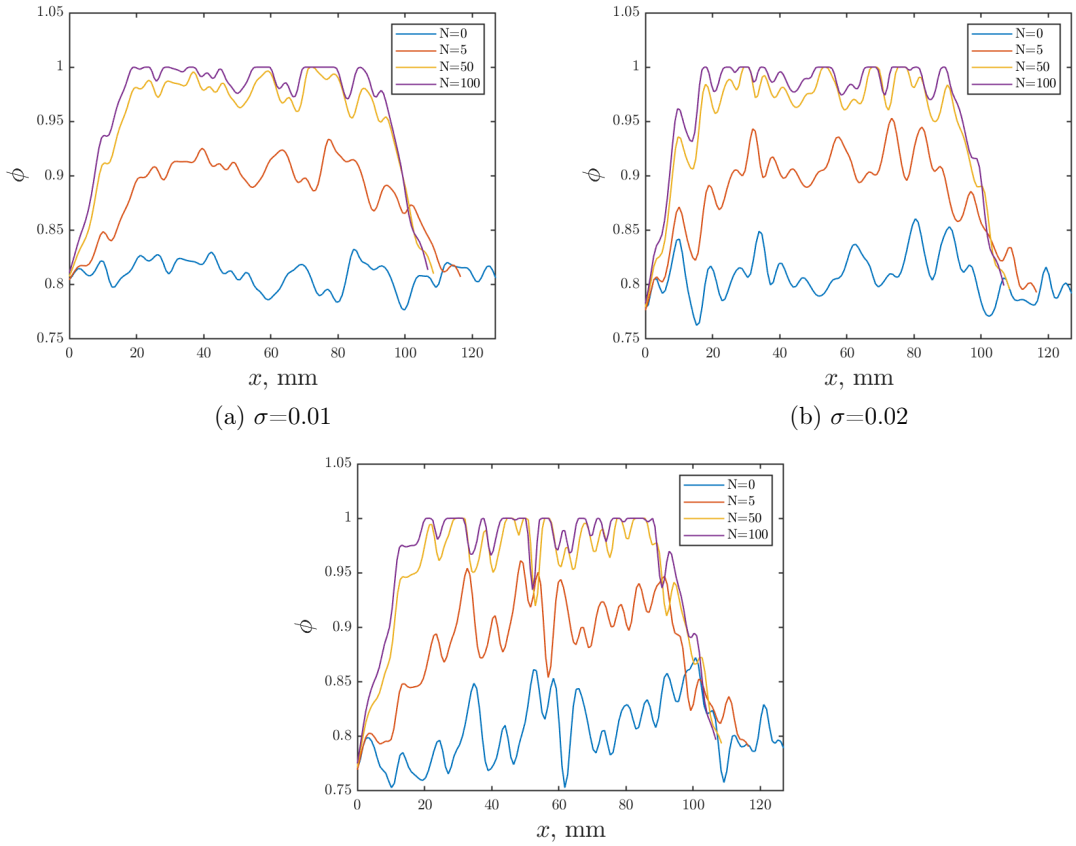

(a) σ=0.01

(b) σ=0.02

(c) σ=0.03

Figure 6.14: Simulated gyratory compaction process for different σ levels

the log-log scale plot Fig. 6.17a that there is a scaling relationship: $\sigma_{ave} \propto l_c^{0.5}$, which confirms Eq.6.8. As shown in Fig. 6.17b, l_c has no effect on the mean of ϕ_{ave}.

6.5 Monte Carlo Simulation–Considering the Randomness in Gyration Number

During the real construction process, there is also randomness in the compaction effort, which might be an important source for the real probability distribution of field densities, as shown in Fig. 6.2. To mimic the randomness in compaction effort in field, we consider the randomness in number of gyrations, N, which represents the compaction effort in laboratory testing condition.

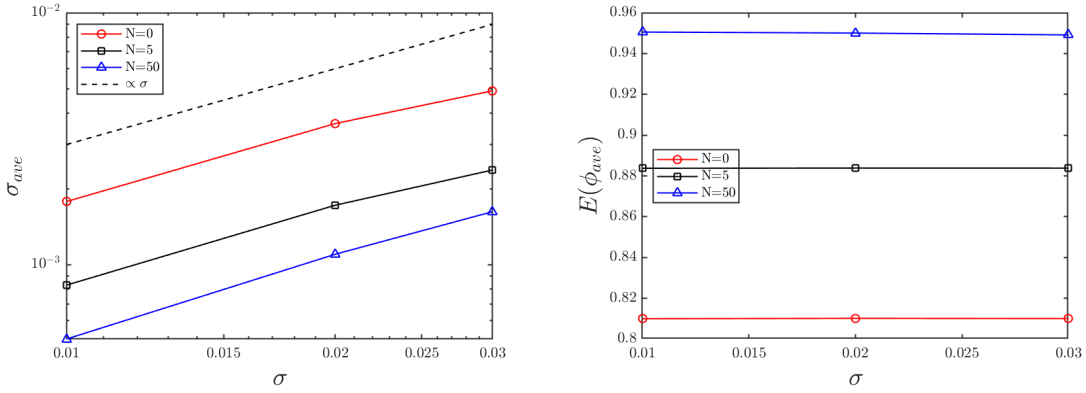

Figure 6.15: Effect of σ on the standard deviation and mean of ϕ_{ave}

Compaction effort can be regarded as a random variable, which is affected by numerous factors additively, so by central limit theorem, it is reasonable to assume N as normally distributed random variable.

$$N \sim \mathcal{N}(\bar{N}, \sigma_N) \tag{6.9}$$

where $\bar{N}$ is the average of the N; σ_N is the standard deviation of N.

Monte Carlo simulation is performed to evaluate the distribution of ϕ_{ave} due to the randomness of N. Values of other parameters are set as the same as that used in Section 6.3. Only one specimen size, $L = 127mm$, is considered.

Fig. 6.18 shows the simulated distribution of ϕ_{ave} when assuming $\bar{N} = 50$ and $\sigma_N = 10$. The basic statistics of this distribution is listed in Table 6.3. It is seen that with the consideration of the randomness in N, the left-skewed (skewness < 0) and leptokurtic (kurtosis > 3) properties of the real field density distribution (Fig. 6.1) can be simulated, which implies that the randomness in compaction effort might be an important source accounting for left-skewed and leptokurtic features of the real field density distribution.

Table 6.3: Basic statistics of the distribution of ϕ_{ave} when $N \sim \mathcal{N}(50, 10)$

	mean, %	st.dev., %	skewness	kurtosis
values	94.96	0.49	-0.81	3.97

To further study how uncertainty in N affects the distribution of ϕ_{ave}, Monte Carlo simulations are performed at different levels of σ_N=0, 5, 10, while $\bar{N} = 40$. The effect of σ_N

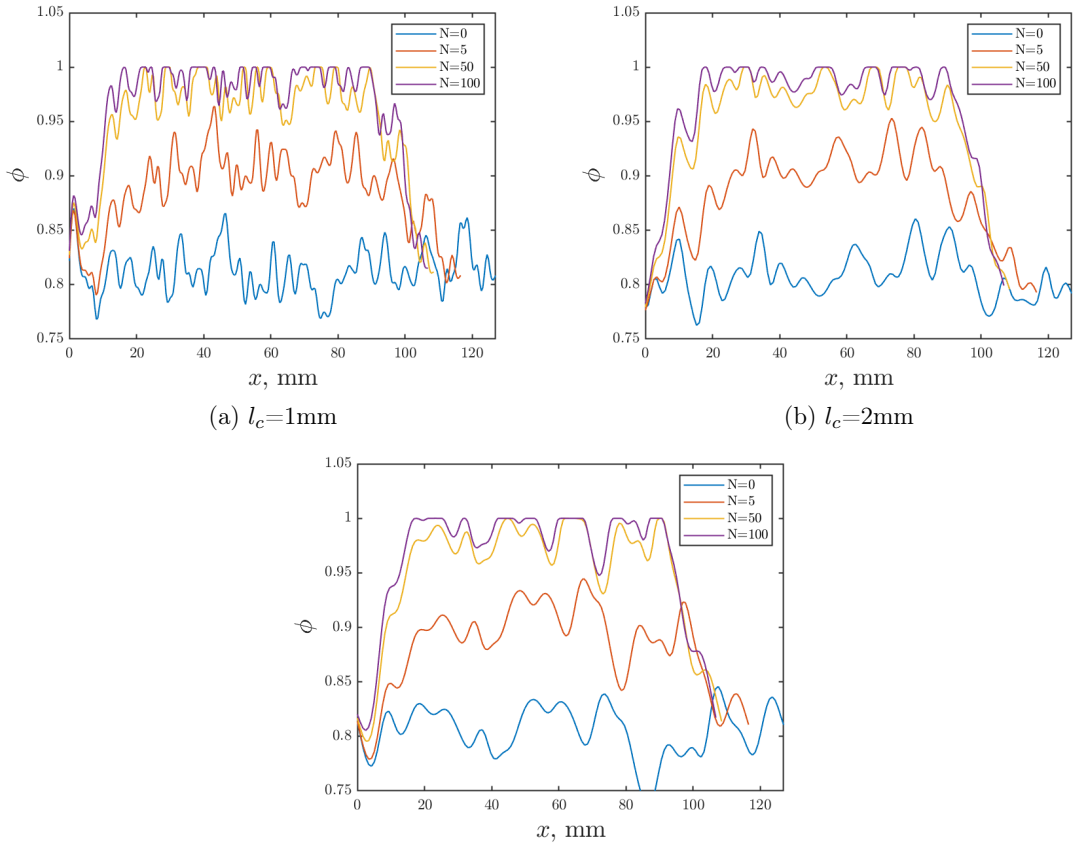

(a) l_c=1mm

(b) l_c=2mm

(c) l_c=3mm

Figure 6.16: Simulated gyratory compaction process for different l_c levels

on the basic statistics of ϕ_{ave} distribution is shown Fig. 6.19. It is seen that as σ_N increases the mean of ϕ_{ave} decreases slightly but almost remains unchanged. The standard deviation of ϕ_{ave} increases with the increase in σ_N. More importantly, as σ_N increases, skewness of ϕ_{ave} decreases while kurtosis of ϕ_{ave} increases, which means that as σ_N increases the distribution of ϕ_{ave} becomes more and more left-skewed and leptokurtic.

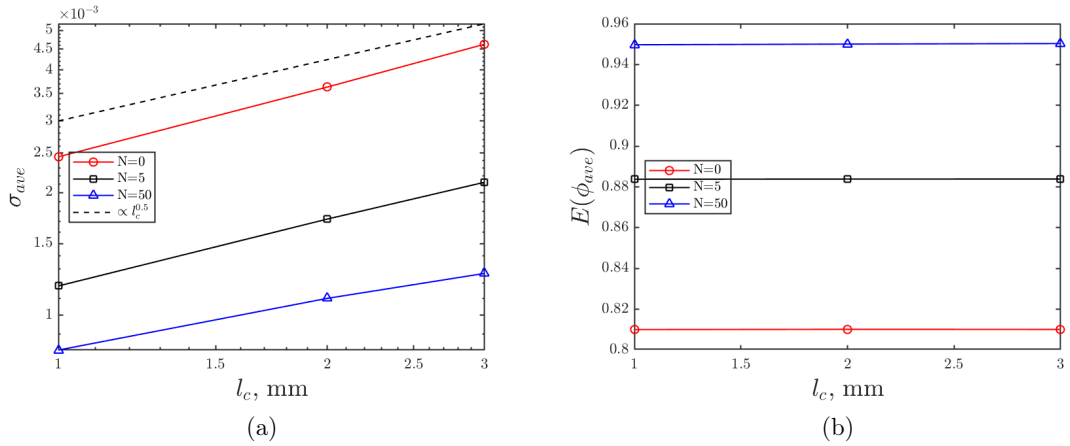

Figure 6.17: Effect of l_c on the (a) standard deviation and (b) mean of ϕ_{ave}

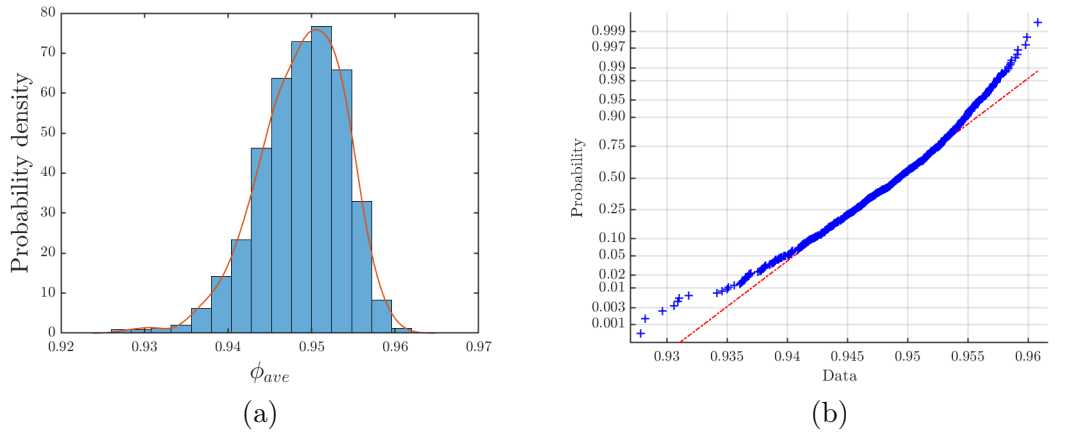

Figure 6.18: Simulated distribution of ϕ_{ave} when $N \sim \mathcal{N}(50, 10)$, (a) histogram, (b) normal probability plot.

6.6 Discussion

6.6.1 Explanation of Features of Field Density Distribution

In this study, we have considered two sources of the randomness in the gyratory compaction process: the randomness in initial density profile $\phi_0(x)$ and in compaction effort N. Given that the gyratory compaction simulates the field compaction to a great extent, the above Monte Carlo simulation results can shed some light on the origin of the features of field density distribution.

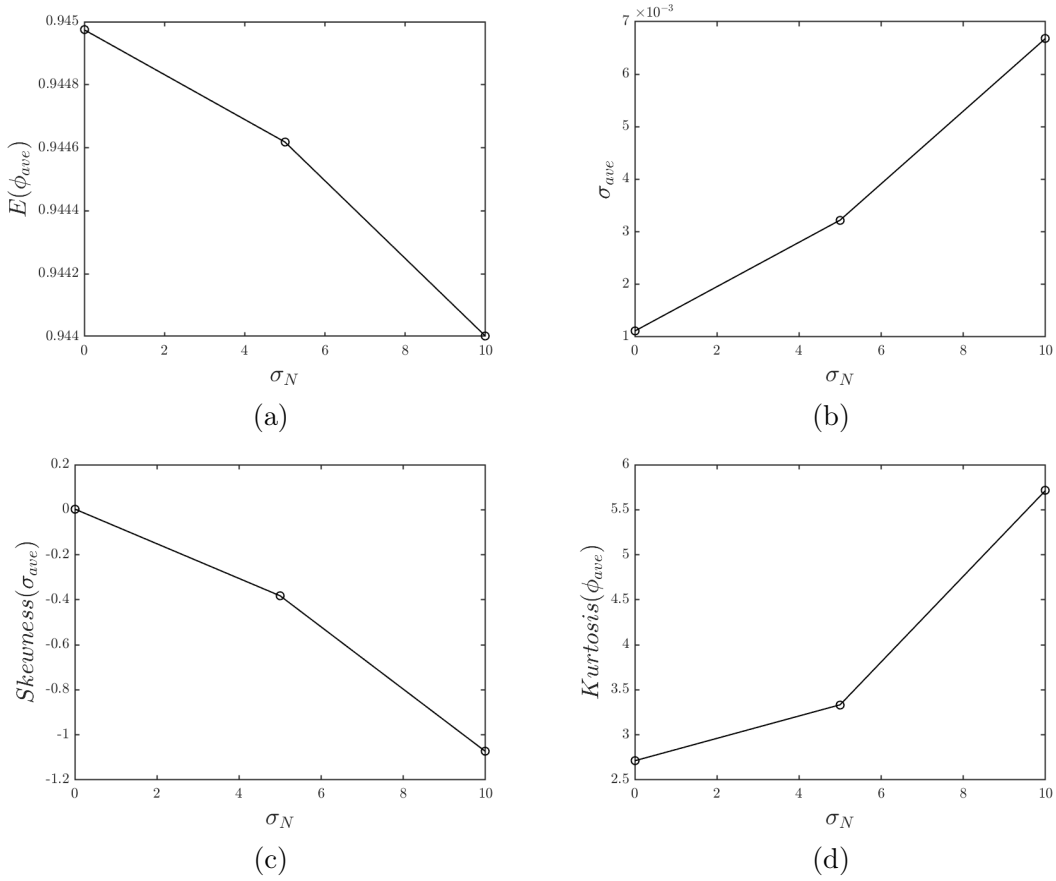

Figure 6.19: Effect of σ_N on the basic statistics of ϕ_{ave} distribution

It is found that the randomness in $\phi_0(x)$ is unlikely to be the main cause of the variation in field density. From Section 6.4, we see that if the source of randomness is only from $\phi_0(x)$, the consequent standard deviation of ϕ_{ave} (less than 0.2%) is much less than that of the real field density distribution (around 1.5%). Moreover, if the source of randomness is only from $\phi_0(x)$, the distribution of ϕ_{ave} would be a normal distribution, which is different from the left-skewed and leptokurtic distribution of field density.

On the contrary, randomness in compaction effort is likely to be the main source that caused the left-skewed and leptokurtic properties of the field density distribution, as has been demonstrated in Section 6.5. However, the randomness of compaction effort along cannot fully explain the field density distribution. As shown in Table 6.3, standard deviation of ϕ_{ave} due to randomness of N (about 0.5%) is still less than that of the field density distribution

(1.5%), which implies that there might be other major randomness sources that we have not yet consider, e.g., the randomness in material compositions.

6.7 Conclusions

In this chapter, the 1D nonlocal model for gyratory compaction (developed in Chapter 5) was employed to study the effect of randomness on compaction of asphalt mixtures. Two sources of randomness were investigated: the randomness in the initial density profile and the randomness in compaction effort. Monte Carlo simulations were performed to compute the probability distribution of average density due to these randomnesses. The main conclusions are the following:

- Randomness in initial density causes a normally distributed ϕ_{ave}. The effect of the randomness in initial density on the distribution of ϕ_{ave} can be summarized by this scaling relationship, $\sigma_{ave} \propto \sigma(l_c/L)^{0.5}$, which can be understood through central limit theorem.

- Randomness in compaction effort or number of gyration N lead to a left-skewed and leptokurtic distribution of ϕ_{ave}, which explains the left-skewed and leptokurtic features in the field density distribution.

Chapter 7

Conclusions

In this research, first, field density data from real construct projects were analyzed to achieve a thorough understanding of the current situation of field compaction. Then, physical mechanisms of compaction were investigated in different length scales. In the length scale of the thickness of asphalt binder films ($\sim$ 10 μm), the tribological property of asphalt binder was studied to understand the effect of asphalt binder on the compaction process of mixtures. In the length scale of asphalt mixtures ($\sim$ 10 cm), two mesoscopic mechanisms (aggregate rearrangement and aggregate-binder interaction) were proposed to explain the macroscopic phenomena observed in gyratory compaction process. Based on the mechanism of aggregate rearrangement, a 1D nonlocal model was proposed to simulate the gyratory compaction process of asphalt mixtures. Lastly, the model was employed to study the effect of randomness on compaction process. The following conclusions are drawn from this study:

(1) Field density exhibits significant randomness, with the mean and standard deviation being 93.4 % G_{mm} and 1.45 % G_{mm} respectively for recent Minnesota projects. The probability distribution of field density clearly exhibits left-skewed and leptokurtic features.

(2) Field density is significantly correlated with the design compaction effort, N_{design}. Higher field density is achieved with lower N_{design}, which shows the consistency between field compaction and laboratory compaction, and confirms that field density can be controlled in the mixture design phase by choosing an appropriate N_{design}. Field density is also significantly correlated with fine aggregate angularity. Higher field densities are achieved by mixtures with lower fine aggregate angularity.

(3) Tribological test characterizes the lubricating behavior (represented by friction coefficient) of a thin film of asphalt binder at varying sliding rate. Compared to the traditional viscosity characterization of asphalt binder, tribological test characterizes the interaction between binder and rough aggregate surfaces, and therefore provides a more comprehensive characterization of the effect of asphalt binder on the compactability of mixtures.

(4) Tribological test of GNP modified binders shows that GNP addition increases the lubricating effect of binder between rough surfaces, which explains why GNP addition improves the compactability of asphalt mixtures. The results also shows that, compared to viscosity, tribological property (friction coefficient) is more related to the compactability of asphalt mixtures.

(5) Two mesoscopic mechanisms are proposed to explain the main macroscopic phenomena in compaction process. The proposed mechanisms are jamming of aggregates and aggregate-binder interaction. By aggregates jamming, compaction process of asphalt mixture can be interpreted as the evolving jammed states of aggregates under the excitation of shear or vibration. This interpretation explains why shear and vibration enhance densification, and why shear resistance increases with density, showing the coupling effects between shear and densification process of asphalt mixture. The mechanism of aggregate-binder interaction explains the decrease in shear resistance in the latter part of gyratory compaction.

(6) A 1D nonlocal model is developed for simulating the gyratory compaction of asphalt mixtures, based on the physical mechanism of aggregate rearrangement (jamming). The model is formulated by combining the local mass balance law and a nonlocal densification model. The proposed model is validated by a set of gyratory compaction tests of different specimen sizes.

(7) The nonlocal densification model involves a material characteristic length scale, which gives rise to strong effects of specimen height and aggregate size on the overall compaction curve as well as on the density profile, which explains the size effect and the shape of density profile observed in experiments.

(8) Parameters of the 1D nonlocal model can be related to the set up of the gyratory compaction and the material properties, such as the tribological property of binder, angularity of aggregates, and aggregate gradation. The model yields predictions on the qualitative effect of material properties on the compaction behavior, and therefore can provide guidance for the design of more compactable asphalt mixtures.

(9) Using the 1D nonlocal model of gyratory compaction, the effect of randomness on

compaction of asphalt mixtures is studied. It is found that randomness in initial density leads to the average specimen density being normally distributed. The effect of the randomness in initial density profile on the distribution of the average specimen density can be summarized by this scaling relationship, $\sigma_{ave} \propto \sigma(l_c/L)^{0.5}$, which can be understood through central limit theorem. The randomness in compaction effort leads to a left-skewed and leptokurtic distribution of average specimen density, which explains the left-skewed and leptokurtic features of the field density distribution. These results can be used to develop a reliability-based specification for the compaction of asphalt pavements.

References

[1] K. Lee, Y. Hwang, S. Cheong, Y. Choi, L. Kwon, J. Lee, and S. H. Kim. Understanding the role of nanoparticles in nano-oil lubrication. *Tribology Letters*, 35(2):127–131, 2009.

[2] L. P. Ingrassia, X. Lu, M. Marasteanu, and F. Canestrari. Tribological characterization of graphene nano-platelet (gnp) bituminous binders. In *Airfield and Highway Pavements 2019: Innovation and Sustainability in Highway and Airfield Pavement Technology*, pages 96–105. American Society of Civil Engineers Reston, VA, 2019.

[3] E. Masad and J. Button. Implications of experimental measurements and analyses of the internal structure of hot-mix asphalt. *Trans. Res. Rec.*, 1891(1):212–220, 2004.

[4] F. N. Finn and J. A. Epps. *Compaction of hot mix asphalt concrete*. Texas Transportation Institute, the Texas A & M University System, 1980.

[5] C. S. Hughes. Compaction of asphalt pavement. Technical Report 152, National Cooperative Highway Research Program Synthesis of Highway Practice, 1989.

[6] R. N. Linden, J. P. Mahoney, and N. C. Jackson. Effect of compaction on asphalt concrete performance. *Trans. Res. Rec.*, 1217:20–28, 1989.

[7] E. D. P. Vivar and J. E. Haddock. HMA Pavement Performance and Durability. Technical Report FHWA/IN/JTRP-2005/14, Purdue University, 2006.

[8] K. Willoughby and J. P. Mahoney. An Assessment of WSDOT's Hot-Mix Asphalt Quality Control and Assurance Requirements. Technical Report WA-RD 517.2, Washington State Department of Transportation, 2007.

[9] D. E Watson, J. Moore, J. Heartsill, D. Jared, and P. Wu. Verification of superpave number of design gyration compaction levels for georgia. *Trans. Res. Rec.*, 2057(1):75–82, 2008.

[10] D. S. Harmelink and T. Aschenbrener. In-place voids monitoring of hot mix asphalt pavements. Technical report, Colorado Department of Transportation, Research Branch, 2002.

[11] B. D. Prowell and E. R. Brown. *Superpave mix design: verifying gyration levels in the Ndesign table*, volume 573. Transportation Research Board, 2007.

[12] Standard practice for Superpave volumetric design for asphalt mixtures. standard, American Association of State Highway and Transportation Officials, 2020.

[13] R. West, C. Rodezno, F. Leiva, and F. Yin. Development of a framework for balanced mix design. Technical report, National Cooperative Highway Research Project (NCHRP), 2018.

[14] F. Moutier. La presse à cisaillement giratoire, modèle de série. *Bulletin Liaison Ponts Chaussées*, (74):137–148, 1974.

[15] W. R. Vavrik and S. H. Carpenter. Calculating air voids at specified number of gyrations in superpave gyratory compactor. *Trans. Res. Rec.*, 1630(1):117–125, 1998.

[16] A. D. Stakston, H. U. Bahia, and J. J. Bushek. Effect of fine aggregate angularity on compaction and shearing resistance of asphalt mixtures. *Transp. Res. Rec.*, (02):14–24, 2002.

[17] A. F. Faheem. *Using the Gyratory Compactor to Measure the Mechanical Stability of Asphalt Mixtures*. PhD thesis, University of Wisconsin–Madison, 2004.

[18] S. Dessouky, E. Masad, and F. Bayomy. Prediction of hot mix asphalt stability using the superpave gyratory compactor. *J Mater. Civil Eng.*, 16(6):578–587, 2004.

[19] G. Huber, J. Haddock, J. Wielinski, A. Kriech, and A. Hekmatfar. Adjusting design air void levels in superpave mixtures to enhance durability. In *Proc., 6th Eurasphalt & Eurobitume Congress 2016*, 2016.

[20] W. R. Vavrik, W. J. Pine, and S. H. Carpenter. Aggregate blending for asphalt mix design bailey method. *Transp. Res. Rec.*, 1789(1):146–153, 2002.

[21] F. Leiva and R. C. West. Analysis of hot-mix asphalt lab compactability using lab compaction parameters and mix characteristics. *Transp. Res. Rec.*, 2057(-1):89–98, 2008.

[22] M. M. Karimi, M. K. Darabi, and N. Tabatabaee. A thermodynamic-based large deformation viscoplastic constitutive relationship for asphalt concrete compaction. *Int. J. Solids Struct.*, jan 2019.

[23] S. Koneru, E. Masad, and K. R. Rajagopal. A thermomechanical framework for modeling the compaction of asphalt mixes. *Mech. Mater.*, 40(10):846–864, 2008.

[24] E. Masad, A. Scarpas, A. Alipour, K. R. Rajagopal, and C. Kasbergen. Finite element modelling of field compaction of hot mix asphalt. part i: Theory. *Int. J. Pavement Eng.*, 17(1):13–23, 2014.

[25] E. Masad, A. Scarpas, K. R. Rajagopal, E. Kassem, S. Koneru, and C. Kasbergen. Finite element modelling of field compaction of hot mix asphalt. part ii: Applications. *Int. J. Pavement Eng.*, 17(1):24–38, 2014.

[26] J. Chen, B. Huang, F. Chen, and X. Shu. Application of discrete element method to superpave gyratory compaction. *Road Mater. Pavement Des.*, 13(3):480–500, 2012.

[27] J. Chen, B. Huang, and X. Shu. Air-void distribution analysis of asphalt mixture using discrete element method. *J. Mater. Civ. Eng.*, 25(10):1375–1385, 2013.

[28] F. Gong, X. Zhou, Z. You, Y. Liu, and S. Chen. Using discrete element models to track movement of coarse aggregates during compaction of asphalt mixture. *Constr Build Mater.*, 189:338–351, nov 2018.

[29] F. Gong, Y. Liu, X. Zhou, and Z. You. Lab assessment and discrete element modeling of asphalt mixture during compaction with elongated and flat coarse aggregates. *Constr Build Mater.*, 182:573–579, sep 2018.

[30] T. Man. *Rheology of Granular-Fluid Systems and Its Application in the Compaction of Asphalt Mixtures*. PhD thesis, University of Minnesota, 2019.

[31] J. Le, M. Marasteanu, and M. Turos. Graphene nanoplatelet (gnp) reinforced asphalt mixtures: A novel multifunctional pavement material. Technical report, NCHRP IDEA Project 173.

[32] J. Le, M. Marasteanu, and M. Turos. Mechanical and compaction properties of graphite nanoplatelet-modified asphalt binders and mixtures. *Road Materials and Pavement Design*, 21(7):1799–1814, 2020.

[33] L. Tashman, E. Masad, B. Peterson, and H. Saleh. Internal structure analysis of asphalt mixes to improve the simulation of superpave gyratory compaction to field conditions (with discussion). *J. Assoc. Asphalt Paving Technol.*, 70, 2001.

[34] S. Thyagarajan, L. Tashman, E. Masad, and F. Bayomy. The heterogeneity and mechanical response of hot mix asphalt laboratory specimens. *Int. J. Pavement Eng.*, 11(2):107–121, 2010.

[35] M. Guler, H. U. Bahia, P. J. Bosscher, and M. E. Plesha. Device for measuring shear resistance of hot-mix asphalt in gyratory compactor. *Transportation Research Record*, 1723(1):116–124, 2000.

[36] K. Shamsi and L. N. Mohammad. Estimating optimum compaction level for dense-graded hot-mix asphalt mixtures. *The Journal of Engineering Research [TJER]*, 7(1):11–21, 2010.

[37] T. Yan, M. Marasteanu, C. Bennett, and J. Garrity. Field density investigation of asphalt mixtures in Minnesota. *Transp. Res. Rec.*, Advance online publication, 2021.

[38] E R. Brown. *Relationship of air voids, lift thickness, and permeability in hot mix asphalt pavements*, volume 531. Transportation Research Board, 2004.

[39] R. West, C. Rodezno, F. Leiva, and A. J. Taylor. Regressing air voids for balanced hma mix design. Technical report, Wisconsin. Dept. of Transportation, 2018.

[40] A. Hekmatfar, R. S. McDaniel, A. Shah, and J. E. Haddock. Optimizing laboratory mixture design as it relates to field compaction to improve asphalt mixture durability. Technical report, Purdue University, 2015.

[41] M. Marasteanu, J.-L. Le, K. Hill, T. Yan, T. Man, M. Turos, M. Barman, U. M. Arepalli, and J. Munch. Experimental and computational investigations of high-density asphalt mixtures. Technical report, Minnesota Department of Transportation, 2019.

[42] Superpave mix design and gyratory compaction levels. Technical brief, Federal Highway Administration, 2010.

[43] Standard specification for construction. Standard, Minnesota Department of Transportation, 2018.

[44] Y. Yildirim, J. Ideker, and D. Hazlett. Evaluation of viscosity values for mixing and compaction temperatures. *J. Mater. Civil Eng.*, 18(4):545–553, 2006.

[45] AASHTO T304, Uncompacted void content of fine aggregate. standard, American Association of State Highway and Transportation Officials, 2017.

[46] ASTM D5821, Standard Test Method for Determining the Percentage of Fractured Particles in Coarse Aggregate. standard, American Society for Testing and Materials, 2017.

[47] AASHTO T166, Standard Method of Test for Bulk Specific Gravity (Gmb) of Compacted Asphalt Mixtures Using Saturated Surface-Dry Specimens. standard, American Association of State Highway and Transportation Officials, 2020.

[48] ASTM D1188, Standard Test Method for Bulk Specific Gravity and Density of Compacted Bituminous Mixtures Using Coated Samples. standard, American Society for Testing and Materials, 2015.

[49] J. W. Tukey. Comparing individual means in the analysis of variance. *Biometrics*, pages 99–114, 1949.

[50] Phillip B Blankenship, Kamyar C Mahboub, and Gerald A Huber. Rational method for laboratory compaction of hot-mix asphalt (with discussion and closure). *Trans. Res. Rec.*, (1454), 1994.

[51] T. Yan, L. P. Ingrassia, R. Kumar, M. Turos, F. Canestrari, X. Lu, and M. Marasteanu. Evaluation of graphite nanoplatelets influence on the lubrication properties of asphalt binders. *Materials*, 13(3):772, 2020.

[52] W. J. Steyn. Applications of nanotechnology in road pavement engineering. In *Nanotechnology in civil infrastructure*, pages 49–83. Springer, 2011.

[53] T. Shirakawa, A. Tada, and N. Okazaki. Development of functional carbon nanotubes-asphalt composites. *International Journal of GEOMATE*, 2(1):161–165, 2012.

[54] J. Yang and S. Tighe. A review of advances of nanotechnology in asphalt mixtures. *Procedia-Social and Behavioral Sciences*, 96:1269–1276, 2013.

[55] M. Arabani and M. Faramarzi. Characterization of cnts-modified hma's mechanical properties. *Construction and Building Materials*, 83:207–215, 2015.

[56] A. N. Amirkhanian, F. Xiao, and S. N. Amirkhanian. Characterization of unaged asphalt binder modified with carbon nano particles. *International Journal of Pavement Research and Technology*, 4(5):281, 2011.

[57] M. Gong, J. Yang, H. Yao, M. Wang, X. Niu, and J. E. Haddock. Investigating the performance, chemical, and microstructure properties of carbon nanotube-modified asphalt binder. *Road Materials and Pavement Design*, 19(7):1499–1522, 2018.

[58] A. J. Hanz, A. Faheem, E. Mahmoud, and H. U. Bahia. Measuring effects of warm-mix additives: Use of newly developed asphalt binder lubricity test for the dynamic shear rheometer. *Transportation research record*, 2180(1):85–92, 2010.

[59] A. J. Hanz and H. U. Bahia. Asphalt binder contribution to mixture workability and application of asphalt lubricity test to estimate compactability temperatures for warm-mix asphalt. *Transportation research record*, 2371(1):87–95, 2013.

[60] T. Bennert, G. Reinke, W. Mogawer, and K. Mooney. Assessment of workability and compactability of warm-mix asphalt. *Transportation research record*, 2180(1):36–47, 2010.

[61] A. Stimilli, F. Frigio, M. Bocci, and F. Canestrari. Influence of production temperature and additive dosage on warm mix asphalt performance. In *World Conference on Pavement and Asset Management (WCPAM), Milan, Italy*, pages 12–16, 2017.

[62] G. L. Baumgardner, G. R. Reinke, and J. Brown. Lubricity properties of asphalt binders used in hot-mix and warm-mix asphalt pavements. In *5th Eurasphalt & Eurobitume Congress, Istanbul, Turkey*, pages 13–15, 2012.

[63] F. Canestrari, L. P. Ingrassia, G. Ferrotti, and X. Lu. State of the art of tribological tests for bituminous binders. *Construction and Building Materials*, 157:718–728, 2017.

[64] L. P. Ingrassia, X. Lu, F. Canestrari, and G. Ferrotti. Tribological characterization of bituminous binders with warm mix asphalt additives. *Construction and Building Materials*, 172:309–318, 2018.

[65] U. A. Mannan and R. A. Tarefder. Tribological and rheological characterisation of asphalt binders at different temperatures. *Road Materials and Pavement Design*, 19(2):445–452, 2018.

[66] F. Chin as Castillo and H. A. Spikes. Mechanism of action of colloidal solid dispersions. *J. Trib.*, 125(3):552–557, 2003.

[67] Y. Y. Wu, W. C. Tsui, and T. C. Liu. Experimental analysis of tribological properties of lubricating oils with nanoparticle additives. *Wear*, 262(7-8):819–825, 2007.

[68] J. Zhou, J. Yang, Z. Zhang, W. Liu, and Q. Xue. Study on the structure and tribological properties of surface-modified cu nanoparticles. *Materials Research Bulletin*, 34(9):1361–1367, 1999.

[69] Z. S. Hu, R. Lai, F. Lou, L. G. Wang, Z. L. Chen, G. X. Chen, and J. X. Dong. Preparation and tribological properties of nanometer magnesium borate as lubricating oil additive. *Wear*, 252(5-6):370–374, 2002.

[70] R. B. Rastogi, M. Yadav, and A. Bhattacharya. Application of molybdenum complexes of 1-aryl-2, 5-dithiohydrazodicarbonamides as extreme pressure lubricant additives. *Wear*, 252(9-10):686–692, 2002.

[71] G. Liu, X. Li, B. Qin, D. Xing, Y. Guo, and R. Fan. Investigation of the mending effect and mechanism of copper nano-particles on a tribologically stressed surface. *Tribology Letters*, 17(4):961–966, 2004.

[72] X. Tao, Z. Jiazheng, and X. Kang. The ball-bearing effect of diamond nanoparticles as an oil additive. *Journal of Physics D: Applied Physics*, 29(11):2932, 1996.

[73] T. Yan, M. Marasteanu, and J.-L. Le. Mechanism-based evaluation of compactability of asphalt mixtures. *Road Mater. Pavement Des.*, 22(sup1):S482–S497, 2021.

[74] F. N. Finn and J. A. Epps. *Compaction of hot mix asphalt concrete*. Texas Transportation Institute, the Texas A & M University System, 1980.

[75] W. J. Pine. Superpave gyratory compaction and the ndesign table. *Relatório Illinois Department of Transportation. Illinois, EUA*, 1997.

[76] S. Doll and K. Schweizerhof. On the development of volumetric strain energy functions. *J. Appl. Mech.*, 67(1):17–21, 2000.

[77] B. D. Prowell, E. Brown, and M. Huner. Evaluation of the internal angle of gyration of superpave gyratory compactors in alabama. 2003.

[78] M. E. Cates, J. P. Wittmer, J. P. Bouchaud, and P. h. Claudin. Jamming, force chains, and fragile matter. *Physical review letters*, 81(9):1841, 1998.

[79] A. J. Liu and S. R. Nagel. Jamming is not just cool any more. *Nature*, 396(6706):21–22, 1998.

[80] R. P. Behringer and B. Chakraborty. The physics of jamming for granular materials: a review. *Reports on Progress in Physics*, 82(1):012601, 2018.

[81] P. Charbonneau, J. Kurchan, G. Parisi, P. Urbani, and F. Zamponi. Fractal free energy landscapes in structural glasses. *Nature communications*, 5(1):1–6, 2014.

[82] A. N. Schofield and P. Wroth. *Critical state soil mechanics*, volume 310. McGraw-hill London, 1968.

[83] A. Graziani, G. Ferrotti, E. Pasquini, and F. Canestrari. An application to the european practice of the bailey method for hma aggregate grading design. *Procedia-Social and Behavioral Sciences*, 53:990–999, 2012.

[84] W. B. Fuller and S. E. Thompson. The laws of proportioning concrete. *Transactions of the American Society of Civil Engineers*, 59(2):67–143, 1907.

[85] F. J. Sánchez-Leal. Gradation chart for asphalt mixes: Development. *J. Mater. Civ. Eng.*, 19(2):185–197, 2007.

[86] M. S. Mamlouk and J. P. Zaniewski. *Materials for civil and construction engineers*. Pearson Prentice Hall Upper Saddle River, NJ, USA:, 2006.

[87] J. Friedman, T. Hastie, R. Tibshirani, et al. *The elements of statistical learning*, volume 1. Springer series in statistics New York, 2001.

[88] S. Weisberg. *Applied linear regression*, volume 528. John Wiley & Sons, 2014.

[89] T. Yan, M. Marasteanu, and J.-L. Le. One-dimensional nonlocal model for gyratory compaction of hot asphalt mixtures. *J. Eng. Mech.*, under review.

[90] X.-J. Li and M. O. Marasteanu. Using semi circular bending test to evaluate low temperature fracture resistance for asphalt concrete. *Exp. Mech.*, 50(7):867–876, 2010.

[91] L. A. Cooley, E. R. Brown, and S. Maghsoodloo. Developing critical field permeability and pavement density values for coarse-graded superpave pavements. *Transp. Res. Rec.*, (1761):41–49, 2001.

[92] A. Archilla and S. Madanat. Statistical model of pavement rutting in asphalt concrete mixes. *Trans. Res. Rec.*, 1764(1):70–77, 2001.

[93] T. Harman, J. R. Bukowski, F. Moutier, G. A. Huber, and R. McGennis. History and future challenges of gyratory compaction: 1939 to 2001. *Trans. Res. Rec.*, 1789(1):200–207, 2002.

[94] A. Consuegra, D. N. Little, H. Von Quintus, and J. L. Burati Jr. Comparative evaluation of laboratory compaction devices based on their ability to produce mixtures with engineering properties similar to those produced in the field. *Transp. Res. Rec.*, (1228), 1989.

[95] AASHTO M323, Standard specification for superpave volumetric mix design. standard, American Association of State Highway and Transportation Officials, 2013.

[96] A. F. Faheem, H. U. Bahia, and H. Ajideh. Estimating results of a proposed simple performance test for hot-mix asphalt from superpave gyratory compactor results. *Transp. Res. Rec.*, (1929):104–113, 2005.

[97] H. L. Ter Huerne, M. F. A. M. Van Maarseveen, A. A. A. Molenaar, and M. F. C. Van De Ven. Simulation of HMA compaction by using FEM. *Int. J. Pavement Eng.*, 9(3):153–163, 2008.

[98] J. Chen, B. Huang, X. Shu, and C. Hu. DEM simulation of laboratory compaction of asphalt mixtures using an open source code. *J. Mater. Civil Eng.*, 27(3):04014130, 2014.

[99] Y. Liu, X. Zhou, Z. You, S. Yao, F. Gong, and H. Wang. Discrete element modeling of realistic particle shapes in stone-based mixtures through matlab-based imaging process. *Constr Build Mater.*, 143:169–178, 2017.

[100] Y. Liu, F. Gong, Z. You, and H. Wang. Aggregate morphological characterization with 3d optical scanner versus x-ray computed tomography. *J. Mater. Civ. Eng.*, 30(1):04017248, 2018.

[101] L. E. Malvern. *Introduction to the Mechanics of a Continuous Medium.* Pearson College Div., 1969.

[102] J. W. Rudnicki. *Fundamentals of Continuum Mechanics.* John Wiley & Sons, West Sussex, 2015.

[103] H. A. Kramers. Brownian motion in a field of force and the diffusion model of chemical reaction. *Physica*, 7:284–304, 1940.

[104] H. Risken. *The Fokker-Planck Equation.* Springer-Verlag, Berlin, 1989.

[105] E. Tadmor and R. E. Miller. *Modeling Materials: Continuum, Atomistic and Multiscale Techniques.* Cambridge University Press, New York, 2011.

[106] P. Salamon, D. N. James, J. R. Harland, J. Pedersen, G. Ruppeiner, and L. Liao. Simulated annealing with constant thermodynamic speed. *Comp. Phys. Comm.*, 49:423–428, 1988.

[107] R. H. J. Peerlings, M. G. D. Geers, R. De Borst, and W. A. M. Brekelmans. A critical comparison of nonlocal and gradient-enhanced softening continua. *Int. J. Solids Struct.*, 38(44-45):7723–7746, 2001.

[108] K. Kamrin and G. Koval. Nonlocal constitutive relation for steady granular flow. *Phys. Rev. Lett.*, 2012.

[109] Z. P. Bažant and J.-L. Le. *Probabilistic Mechanics of Quasibrittle Structures: Strength, Lifetime, and Size Effect.* Cambridge University Press, Cambridge, U.K., 2017.

[110] K. Kamrin. Non-locality in Granular Flow: Phenomenology and Modeling Approaches. *Front. Phys.*, 7(August):1–7, 2019.

[111] Z. P. Bažant and G. Pijaudier-Cabot. Nonlocal continuum damage, localization instability and convergence. *J. Appl. Mech. ASME*, 55:287–293, 1988.

[112] Z. P. Bažant and M. Jirásek. Nonlocal integral formulations of plasticity and damage: Survey of progress. *J. Engrg. Mech., ASCE*, 128(11):1119–1149, 2002.

[113] E. Masad, V. K. Jandhyala, N. Dasgupta, N. Somadevan, and N. Shashidhar. Characterization of air void distribution in asphalt mixes using x-ray computed tomography. *J. Mater. Civ. Eng.*, 14(2):122–129, 2002.

[114] L. Tashman, E. Masad, J. D'Angelo, J. Bukowski, and T. Harman. X-ray tomography to characterize air void distribution in superpave gyratory compacted specimens. *Int. J. Pavement Eng.*, 3(1):19–28, 2002.

[115] J. B. Knight, C. G. Fandrich, C. N. Lau, H. M. Jaeger, and S. R. Nagel. Density relaxation in a vibrated granular material. *Phys. Rev. E*, 51(5):3957, 1995.

[116] G. Peng and T. Ohta. Logarithmic density relaxation in compaction of granular materials. *Phys. Rev. E*, 57(1):829, 1998.

[117] E. Ben-Naim, J. B. Knight, E. R. Nowak, H. M. Jaeger, and S. R. Nagel. Slow relaxation in granular compaction. *Physica D*, 123(1-4):380–385, 1998.

[118] AASHTO M332, Standard Specification for Performance-Graded Asphalt Binder Using Multiple Stress Creep Recovery (MSCR) Test. standard, American Association of State Highway and Transportation Officials, 2020.

[119] AASHTO T209, Standard Method of Test for Theoretical Maximum Specific Gravity (Gmm) and Density of Asphalt Mixtures. standard, American Association of State Highway and Transportation Officials, 2020.

[120] AASHTO M312, Standard Method of Test for Preparing and Determining the Density of Asphalt Mixture Specimens by Means of the Superpave Gyratory Compactor. standard, American Association of State Highway and Transportation Officials, 2019.

[121] H.-C. Dan, D. Yang, L. Zhao, S. Wang, and Z. Zhang. Meso-scale study on compaction characteristics of asphalt mixtures in superpave gyratory compaction using smartrock sensors. *Constr. Build. Mater.*, 262:120874, 2020.

[122] Z. A. Khan, H. I. A. Wahab, I. Asi, and R. Ramadhan. Comparative study of asphalt concrete laboratory compaction methods to simulate field compaction. *Constr. Build. Mater.*, 12(6-7):373–384, 1998.

[123] R. Delgadillo and H. U. Bahia. Effects of temperature and pressure on hot mixed asphalt compaction: field and laboratory study. *J. Mater. Civ. Eng.*, 20(6):440–448, 2008.

[124] M. Shinozuka and G. Deodatis. Simulation of stochastic processes by spectral representation. *Appl. Mech. Rev.*, 44(4):191–204, 1991.